NTNU

Norwegian University of
Science and Technology

A radar simulator for generating micro-Doppler datasets to be used for Automatic Target Recognition

Anders Liland

Master of Science in Electronics
Submission date: June 2018
Supervisor: Lars Magne Lundheim, IES

Norwegian University of Science and Technology
Department of Electronic Systems

Abstract

To train a classifier used for automatic target recognition, a large dataset of annotated target signatures is needed. Obtaining such datasets from real recordings can be very time-consuming. Therefore a system for generating annotated feature sets, based on radar signatures is developed. Micro-Doppler signatures are obtained from the radar recordings and reduced to a compact feature set intended for classification.

The dataset is extracted with the intention to train a classifier to automatically identify a human and a dog target. The system consists of three modules: the target simulator, the radar simulator, and the feature extractor. The target simulator uses motion capture recordings to create a point scatterer model of each target. The radar simulator is configured as an ultra-wideband pulse-Doppler radar. The feature extraction module performs a time-frequency analysis to obtain the targets periodic micro-Doppler signature. From this, a feature extraction is performed to compactly describe each target with six parameters.

The extracted feature parameters showed some clustering for similar target types. This is desirable and will help the classifier estimate the correct target class. Since only one motion capture data of a dog was obtained, a comparison with the human data could not be made.

Sammendrag

For å trene et klassifikasjons system som skal brukes til automatisk målgjenkjenning, er et stort datasett med annoterte målsignaturer nødvendig. Å skaffe slike datasett fra ekte opptak kan være svært tidkrevende. Derfor er det utviklet et system for å generere annoterte datasett, basert på Micro-Doppler-signaturer. Disse skaffes fra radaropptakene og reduseres til et kompakt sett parameter som er egnet for klassifisering.

Datasettet er hentet med intensjon om å trene en klassifikasjons systemet for automatisk å identifisere et menneske og et hundemål. Systemet består av tre moduler: målsimulatoren, radarsimulatoren og parameterutvinningsmodul. Målsimulatoren bruker «motion capture» for å lage en punktspredermodell for hvert mål. Radarsimulatoren er konfigurert som en ultra-bredbånds puls-Doppler radar. Parameterutvinningsmodulen utfører en tid og frekvens-analyse for å hente ut den periodiske mikro-Doppler-signaturen. Fra denne hentes det ut seks parametere, som mer kompakt beskriver målets karakteristikk.

De seks parameterne viste en del gruppering for like måltyper. Dette er ønskelig og vil hjelpe et klassifiserings system å korrekt anslå riktig målklasse. Siden kun ett «motion capture» fra en hund var tilgjengelig, kunne det imidlertid ikke foretas en sammenligning med menneskelige data.

Preface

I want to thank Jan Road Pleym and Novelda for providing this project opportunity, necessary tools and guidance in understanding the complexity of ultra-wideband (UWB) pulse-Doppler radar technology.

I also want to extensively thank professor Lars Magne Lundheim from the NTNU department of electronic systems, who was my supervisor in this work. He thoroughly explained the answers to my questions, and provided excellent inspiration when no questions could be formulated.

Anders Liland
Trondheim, June 2018

Contents

Nomenclature

β_1, β_2	Step harmonic frequency ratios	
$\boldsymbol{\mu}$	Micro-Doppler signature matrix	
$\boldsymbol{\Upsilon}$	Radar simulator data matrix	
$\boldsymbol{D}$	Step-Doppler matrix	
$\boldsymbol{G}$	Range-Doppler matrix	
$\boldsymbol{Y}$	Framebuffer matrix	
χ	Target index	
Λ	Target movement data file	
λ	Wavelength	m
ψ	Radar LOS aspect angle	
σ	Radar cross section	m^2
σ_w	Gaussian window steepness	
τ	Pulse width/duration	s
θ	Transmit signal phase	rad
θ'	Received signal phase	V
$\vec{R}$	Range vector	m
$\vec{v_r}$	Point scatterer radial velocity vector	
$\vec{v_t}$	Point scatterer tangential velocity vector	
$\vec{v}$	Point scatterer velocity vector	
A	Transmit signal amplitude	V
A'	Received signal amplitude	V
A_2	Amplitude at the 2^{nd} harmonic step frequency f_2	

A_3	Amplitude at the 3^{rd} harmonic step frequency f_3	
A_m	Amplitude at the fundamental step frequency f_m	
A_{f_d}	Amplitude of the Doppler frequency f_d	
B	Half power bandwidth	Hz
B_μ	Micro-Doppler bandwidth	Hz
B_H	Tracking limit micro-Doppler bandwidth high	Hz
B_L	Tracking limit micro-Doppler bandwidth low	Hz
B_r	Spatial Doppler bandwidth	Hz
c	Speed of light in a vacuum	$299,792,458\,\mathrm{m/s}$
F	Feature-Set	
f_2, f_3	2^{nd} and 3^{rd} harmonic step frequency	Hz
f_c	Carrier frequency	Hz
f_d	Doppler frequency	Hz
f_m	Stride frequency	Hz
f_p	Pulse repetition frequenc	Hz
f_r	Motion capture recording frame rate	
f_s	Fast-time samplings frequency	Hz
G_{rx}	Receiver amplifier gain	dB
G_r	Receiver antenna gain	dB
G_t	Transmitter antenna gain	dB
H	Target Height	
I	Number of radar frames in each scenario	
K	Number of discrete Fourier transform (DFT) frequency bins	
k	discrete Fourier transform (DFT) frequency bin index	
l	Point scatterer index	
$L(t_f)$	Free space path loss amplitude ratio	
L_χ	Number of point scatterer in target χ	
L_m	Step length	m
L_{stride}	Stride length	m

M	Number of frames in framebuffer	
m	Frame buffer frame index	
N	Number of range bins (fast-time samples) in each radar frame	
n	Range bin/fast-time index	
P	Radar parameters	
$p(t)$	Gaussian pulse shape function	
P_t	Peak transmit power	W
p_x, p_y, p_z	Radar position	
R	Range from radar position to target point scatterer	m
$r(t)$	Received echo signal	
R_H	Tracking limit range high	m
R_L	Tracking limit range low	m
R_t	Target range span	m
r_{max}	Frame maximum distance	
r_{min}	Frame minimum distance	
r_{span}	Distance within a frame	
$s(t)$	Transmitted radar signal	
T	pulse repetition interval (PRI)	s
t	Global Time	s
t_0	Received signal propagation delay	s
t_1	ADC start sampling time	s
t_2	ADC stop sampling time	s
t_μ	Micro-Doppler bandwidth threshold	
t_c	Carrier wave period	s
T_d	Coherent Processing Interval (CPI)	s
t_d	Frame time variable	s
T_o	Observation time	s
t_{step}	Step period	s
t_{stride}	Stride/gait cycle period	s

v	Point scatter velocity	$\mathrm{m/s}$
v_m	Target radial velocity	$\mathrm{m/s}$
$w[m]$	Gaussian window coefficients	
X	Number of targets in each scenario	
x, y, z	Point scatterer position	

Chapter 1

Introduction

1.1 Problem Description

Automatic target recognition (ATR) in radar is the ability of an algorithm to recognize targets based on their radar signature. It was initially performed by listening to an audible representation of the received radar signal, where a trained operator could distinguish sound from different targets. With the advancement in radar and computing technology this process is automated, which drastically reduce the time and improves the accuracy of target recognition.

Home alarm systems is a typical scenario where an ATR capability is desired. With the capability to differentiate between human and non-human targets, such as pet-animals, the alarm can be active inside the house, even when pet-animals are present. For example, many of today's alarm systems use a perimeter protection where all entry points into a house are monitored by open/closed sensors. These detect if a window or door is open or closed. Inside the house, there are movement detectors, typically infrared (IR) sensors which trigger on all motion. With such a system it is not possible for anything to move inside the house while the alarm is active. By replacing the movement detectors with radars, humans and pet animals can be discerned, and the alarm only is triggered when a human is detected. This way pet animals can move freely inside the house, even while the alarm is active.

There exists a wide variety of automatic target recognition techniques used in radar. In [1] Fossum identified nine different ATR possibilities, and identified that the *micro-Doppler effect* (previously called *jet engine modulation* [2, p. 382]) was most broadly applicable for moving humans and most kinds of four legged animals. The micro-Doppler effect in explained in Section 2.4.1.

The process of determining target class based on a dataset is called *classification*. A classifier is an algorithm which processed datasets and produces labels as output, corresponding to what type of target is recognized. In [3] and [4] a neural network classifier is used to classify the targets, based on their micro-Doppler signature. These require large, *annotated datasets*. An annotated dataset provides, for each target, the true target class to the classifier. This enables the use of a supervised classifier.

The goal of this project is to create a system which generates multiple human and dog micro-Doppler signatures and perform a feature extraction on these to prepare the dataset for classification.

1.2 Previous Work

Previous work [1, 5, 3] have been conducted with the aim of extracting *micro-Doppler signatures* from an UWB pulse-Doppler radar recording. The hypothesis was that the micro-Doppler signature contains enough information about a target, to successfully classify it. In [3] a simple human and dog movement simulator was used to synthetically generate micro-Doppler signatures. A set of features was extracted from these, and classified with an artificial neural network (ANN), yielding an accuracy of 89%.

In [6] a very accurate human movement simulation is created, based on empirical mathematical parameterizations derived from biomechanical experimental data from [7]. This type of simulation requires a lot of time and effort to develop and limits the number of targets and movement patterns available. Hence a method for easily obtaining accurate target movement data should be created.

These results have two main limitations: first the human and dog simulation model used in [3] was very simple, and it is assumed that it will not produce movement patterns accurate enough to train a classifier to successfully classify targets from real radar recordings. Second, the simulation is limited to only a few different target models, and movement patterns. The motion data should be as varied as in real life, to better train the classier for real radar recordings. In addition, this prevents over-fitting of the classifier. This is a situation where the classifier becomes very good at classifying the training data but is too specific such that it performs very poor on the real data it is trained for.

1.3 Proposed Solution

The presented solution is building on the work of [5] and [4], where [5] presented a radar simulator and [4] proposed multiple feature extraction methods. A system to generate micro-Doppler signatures and a feature set extractor is developed. The system is divided into three modules: a target simulator, a radar simulator, and a feature extractor as shown in Figure 1.1. The classification module is not part of this project, but it is presented here to illustrate how the system is intended to be used.

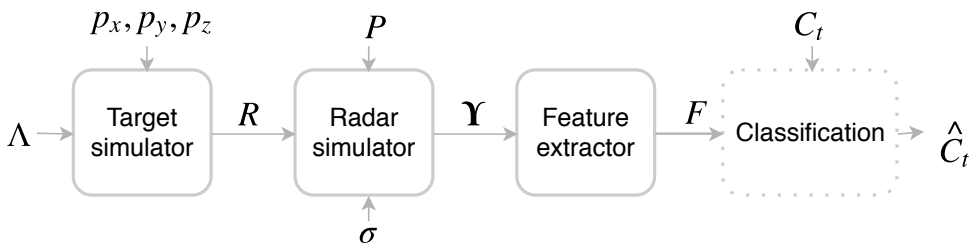

Figure 1.1: System overview

- The *target simulator* reads a *target movement data file* Λ and performs necessary control and clean-up of the data. Λ provides position coordinates (x, y, z) for the target, as will be explained in Section 2.2.1. Based on these it calculates the range R from the radar in position (p_x, p_y, p_z) to the target in position (x, y, z), which will be explained in Section

2.3. For each target a label, C_t is added in order to annotate the dataset created by the feature extractor.

- The *radar simulator* module simulates the signal processing of a stationary *monostatic* pulse-Doppler radar. Monostatic means that the transmit and receive antenna are the same antenna, or two antennas located close enough to be considered the same antenna. The *radar parameters* P contains the settings used to specifying the radars operation, and is given in Section 5.1. The module computes the returned echo from the target, given its range R and radar cross-section (RCS) σ. σ determines how much electromagnetic (EM) energy is reflected off the target to the radar. RCS modeling is explained in Section 3.1.

  The module outputs a two-dimensional data matrix $\boldsymbol{\Upsilon}$ containing the raw radar data. This module supports the same output formats as [8], which makes it easy to change between the simulator and a real radar when testing new algorithms. The radar module is explained in detail in Chapter 3.

- The *feature extractor* does a time-frequency analysis of $\boldsymbol{\Upsilon}$ extracting frequency and time information, which makes up the *micro-Doppler signature*. Based on the movement characteristics captured in the micro-Doppler signature, a *feature-Set* F is obtained. The feature extractor is explained in Chapter 4.

Using F and C_t as inputs, a classifier could be trained to automatically recognize humans and dogs, from their micro-Doppler signature. The estimated target class from the classification module is denoted $\hat{C}_t$, and it follows that if $\hat{C}_t = C_t$ the target is classified correctly. The proposed solution can, in theory extract and classify any kind of target that creates a micro-Doppler signature, but to narrow down the task it is determined to only classify humans and pet-animals such as dogs and cats. When referring to pet animals through this report, it is given that this is limited to four-legged dogs.

The radar simulator will be developed independent of a specific radar, such that it can easily be used to simulate radar recordings of a large variety of pulse-Doppler radars. However, when presenting the results the simulator settings will be specified to match a radar setup using the XeThru X4 system on chip (SoC) UWB pulse-Doppler radar [9] from Novelda AS, explained in Section 5.1.

Chapter 2

Target Simulator

The target simulator module provides the radar simulator with range values R. The range values are extracted from a target movement file Λ, as shown in Figure 2.1.

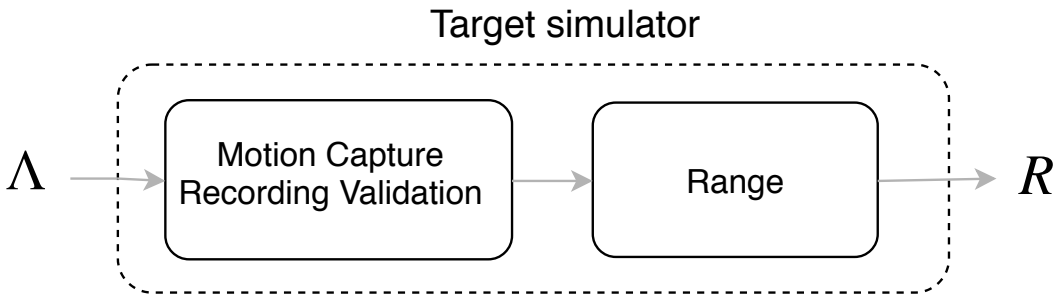

Figure 2.1: Target simulator module overview

The target movement file Λ is obtained from external sources, as explained in Section 2.2. Since Λ is an external file loaded into the system, it needs to be validated, eventual errors corrected and adapted to the current radar parameters P, which is explained in Section 2.2.2. If the file is successfully validated the range between the target and the radar is computed as explained in Section 2.3.

2.1 Point Scatterer Modeling of Radar Targets

Accurately simulating the motion of humans and pet-animals is very complex, time-consuming, and strictly not necessary to achieve a unique and distinguishable target signature [6, p. 50]. A simpler, yet accurate model can be obtained by decomposing each target into a composition of *point scatterers*, where the position of a scatterer is described in a Cartesian coordinate system by x, y, z. Figure 2.2 shows a collection of point scatterers representing a human (a) and a dog (b).

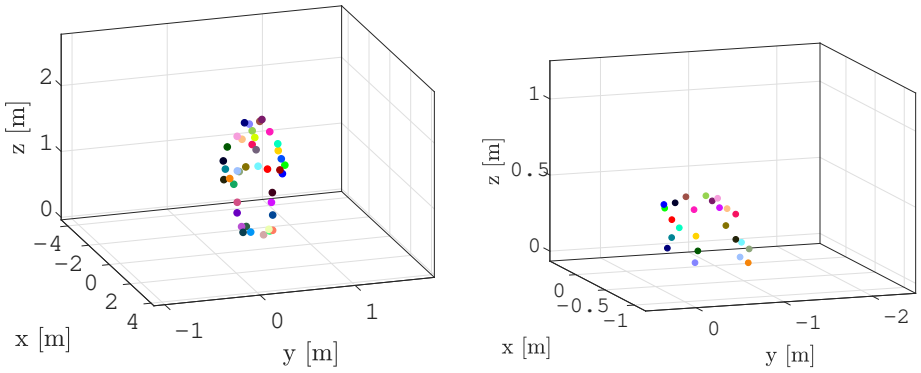

(a) Human target from 41 point scatters. (b) Dog target from 24 point scatters.

Figure 2.2: Point scatterer models of a Human and Dog target.

In (a) the human target is mowing in the positive x direction, with a *target height* $H = 1.8$ m. The center top scatterer makes up the torso, with two arms protruding form the upper and two legs from the bottom part of the torso. In (b) a dog is moving in the negative y direction, with a height $H = 0.5$ m. The top line of scatterer represents the torso, with four legs protruding down.

2.2 Target Movement Data

Point scatter coordinates which accurately model human and animal movement can be obtained from multiple sources. In [6] a complex human gait simulation is created. This is a very accurate model, but limited to only one target class. In [5] a much simpler target movement simulator was developed for a human, dog and cat. This has however limited accuracy compared to real motion patterns. Both [6] and [5] require considerable time and effort in analyzing a targets gait patterns and building a mathematical description for its movements. This limits the number of target classes to be modeled. *Motion capture (mo-cap)* is the process of recording movement of objects or people. It has been identified as a good system for obtaining scatter coordinates from human and animal targets, providing both accurate and diverse target movement models.

2.2.1 Motion Capture

A common system for motion capture consist of multiple cameras, arranged around a recording area as shown in Figure 2.3.

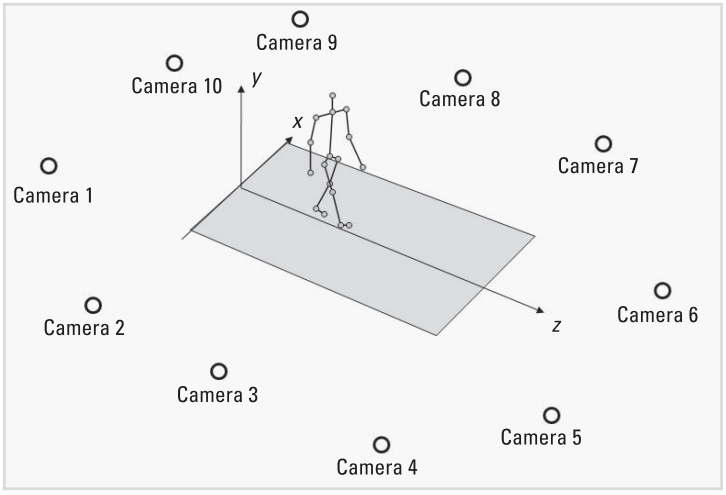

Figure 2.3: Optical motion-capture system equipped with multiple cameras [6, p. 181].

The target have special markers placed on their body, often with some reflective surface or tracking light. The system tracks the movement of the target and calculates a position for each maker. This way each marker from the recording can be used to represent a point scatterer in the simulation.

Creating motion capture recordings require expensive equipment and is out of scope of this project. However multiple motion capture databases of human and animal motion are available for free [10], and is used in this project. [11] is very good for human targets and contains hundreds for recordings.

2.2.2 Motion Capture Recording Validation

Figure 2.4 shows an overview of the validation steps performed when loading a mo-cap target motion file Λ.

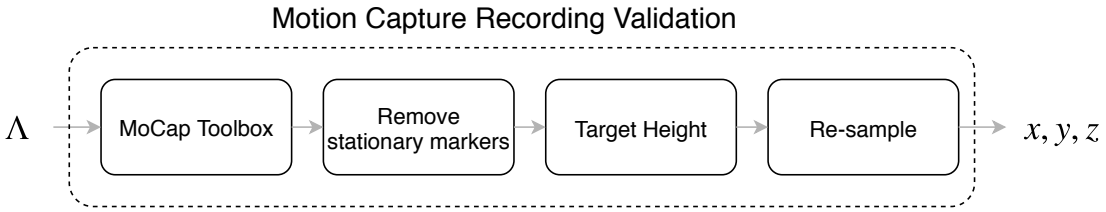

Figure 2.4: Motion capture validation

- The mo-cap target movement data file Λ is loaded by using the MoCap MATLAB Toolbox [12]. This module only accepts $.c3d$ files, which is a binary file format used in biomechanics, animation and gait analysis to record motion capture since the mid-1980 [13]. It is supported by all major 3D Motion Capture System Manufactures. The MoCap MATLAB Toolbox outputs x, y, z coordinates for each marker, for each frame.
- Stationary markers are removed. These are often placed on the floor as a reference when recording motion capture. It is not desired to include these markers in the target motion signature.
- All markers are scaled in the z dimension such that the marker with the highest z value is equal to the target height H. This correctly scales the target velocity and allows for different target heights.

- The mo-cap file is recorded with a frame rate f_r. This is most likely not equal to the radars frame rate f_p, called the pulse repetition frequency (PRF), which is explained in Chapter 3. The mo-cap frames rate needs to match the radars frame rate. Hence the mo-cap recording is re-sampled such that $f_r = f_p$.

2.3 Scatter Range and Velocity

Figure 2.5 illustrates the coordinate systems used to locate the radar and point scatterer. The radar position, as mentioned earlier, is given by (p_x, p_y, p_z) and illustrated by the antenna icon. The point scatter is the black dot in the middle at (x, y, z). The coordinate system is drawn in two dimensions for simplicity, but the derivation will be given for three-dimensional space.

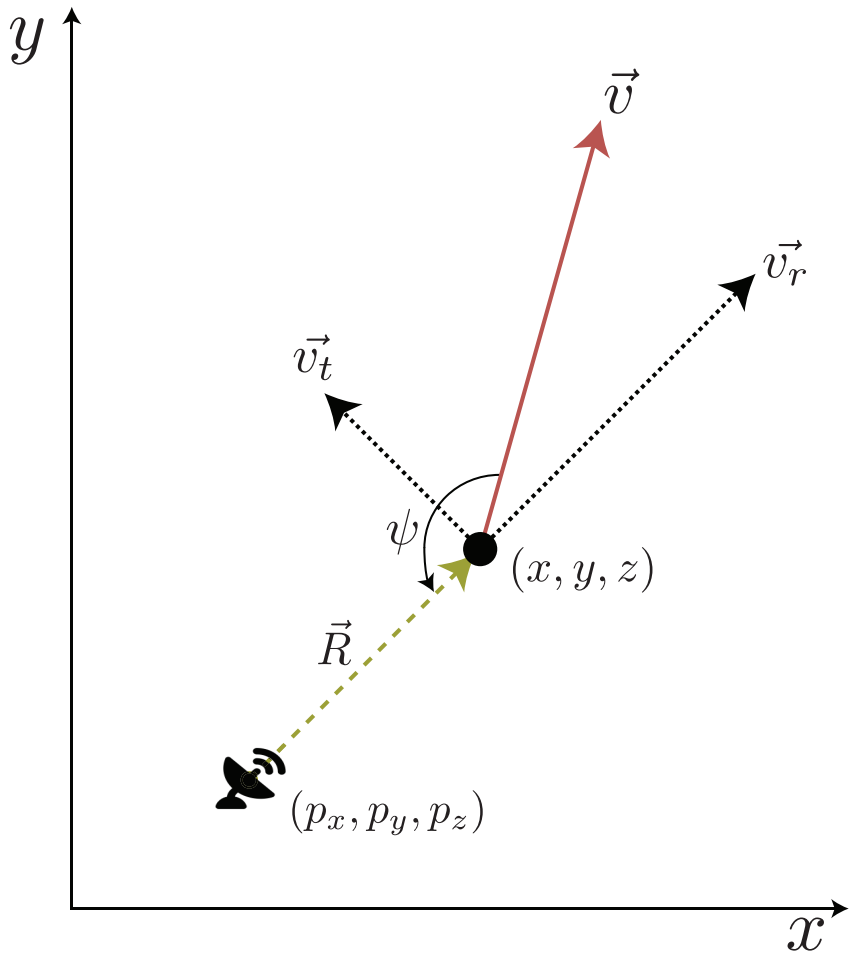

Figure 2.5: Radar coordinate reference

The range R from the radar to the point scatter is given by

$$R = |\vec{R}| = \sqrt{(x - p_x)^2 + (y - p_y)^2 + (z - p_z)^2} \tag{2.1}$$

where $\vec{R}$ is the line-of-sight (LOS) range vector, which points from the radar to the point scatter. It is illustrated in Figure 2.5 as the dotted yellow line.

The *velocity vector* $\vec{v}$ is a vector from the scatter position, pointing in the direction the scatter is moving. $\vec{v}$ can be decomposed into a radial and a tangential vector as $\vec{v} = \vec{v_r} + \vec{v_t}$, respectively. The scatterer velocity is given as $v = |\vec{v}|$, and the radial velocity v_r is given as

$$v_r = |\vec{v_r}| = |\vec{v}| \cdot \cos\psi \tag{2.2}$$

where ψ is the angle from $\vec{v}$ to $\vec{R}$. v_r is defined to be positive for an approaching scatter ($\psi = 0°$) and negative for a receding scatter ($\psi = 180°$).

2.4 The Doppler Frequency Shift

Due to the Doppler Effect the frequency of an echo from a moving point scatter will differ from the transmitted frequency f_c. For a monostatic radar system the transmitted EM wave travels twice the distance between the transmitter/receiver and the point scatter. With the assumption that $v \ll c$ the Doppler frequency shift for a point scatter is given as [6, p. 7]

$$f_d = f_c \frac{2v}{c} = \frac{2v}{\lambda} \quad \text{[Hz]} \tag{2.3}$$

where $\lambda = c/f_c$ is the wavelength of the transmitted signal in meters, and c is the propagation speed of EM waves. With respect to v_r, f_d is given as

$$f_d = \frac{2v}{\lambda}\cos\psi = \frac{2v_r}{\lambda} \quad \text{[Hz]} \tag{2.4}$$

where f_d is maximum if a scatter is moving directly inbound ($\psi = 0°$) or outbound ($\psi = 180°$). If $\psi = 90°$, then $v_r = 0$ m/s, and hence $f_d = 0$ Hz. Figure 2.6 shows how the Doppler frequency shift f_d, corresponds to the radial velocity, v_r.

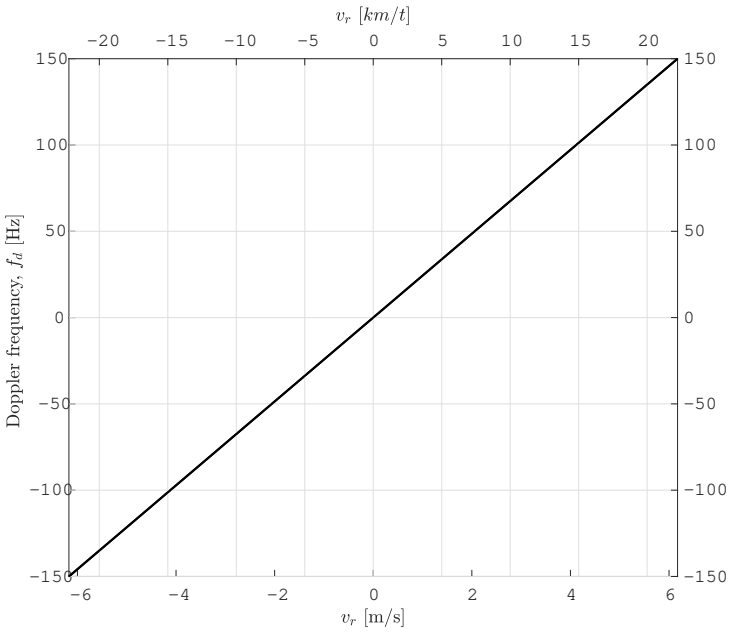

Figure 2.6: Doppler frequency shift f_d versus radial velocity v_r.

The black center line shows the linear relationship between f_d and v_r. In this example if $f_d > 150$ Hz, or $f_d < -150$ Hz the Doppler frequency will alias and not be unique to only one v_r.

Equation 2.4 shows only the physical relationship between the Doppler frequency shift and the radial velocity. It cannot be used to extract f_d, since v_r is unknown. Section 3.4 explains how a pulse-Doppler radar extract the Doppler frequency shift from multiple returned echoes.

2.4.1 The Micro-Doppler Effect in Radar

A moving object introduces a Doppler frequency shift in a returned radar signal. If the object moves at a constant velocity the Doppler frequency shift will be constant. If the object itself, or parts of it has oscillations or vibrations these will induce minor modulation to the objects Doppler frequency shift. This minor modulation is called the *micro-Doppler effect*. With recent technology advancement in radar and signal processing, it is possible to capture these minor modulations, as explained in Section 4.3.

2.5 Scenario creation

To better describe the setup for each simulation a *scenario* framework is introduced. One scenario encapsulates one simulation, starting when Λ is loaded, until F is exported. Each scenario have one stationary radar position (p_x, p_y, p_z), and use the same radar hardware settings P. All targets can move independently, with respect to each other in the xy plane.

Each scenario has X targets, each consisting of L point scatters. The subscript l and χ are used to identify which scatter from which target a value is representing. For instance the range to scatter l for target χ would be given by $R_{\chi,l}$. From a scenario with X targets, X micro-Dopplers signatures are computed, and X feature-Sets obtained, indexed as F_χ, as illustrated in Figure 2.7.

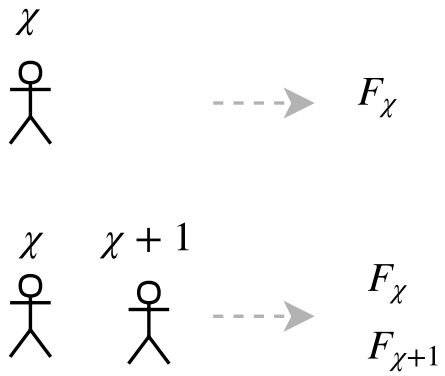

Figure 2.7: One feature-set F is extracted for each target.

2.6 Gait motion

To better explain the micro-Doppler signature from a moving human and dog, it is necessary to present a structured framework for describing their movement patterns. A human or animals manner of walking is defined as its *gait* [14]. In the context of this report it is used to describe the pattern of movement of the limbs of animals, including humans, during

locomotion over a solid substrate. One *stride* (also called *gait cycle*) is defined as the motion performed from heel-strike to heel-strike of the same foot, and a *heel-strike* is when the heel of the foot lands on the ground. One stride takes t_{stride} seconds, and the frequency of which the stride repeats itself is the *stride frequency* $f_{stride} = 1/t_{stride}$ [15, Ch. 91]. Each stride consists of two *steps*, where one step is defined as the movement from heel-strike of on foot, until a successive heel-strike of the opposite foot. One step takes t_{step} seconds and repeats repeats itself at the *step frequency* f_m. The stride length L_{stride} is given by

$$L_{stride} = \frac{v}{f_{stride}} \tag{2.5}$$

where v is the velocity of the moving human or animal. In similar fashion the step length L_m is

$$L_m = \frac{v}{f_m} \tag{2.6}$$

Figure 2.8 illustrates the difference between a stride and step length.

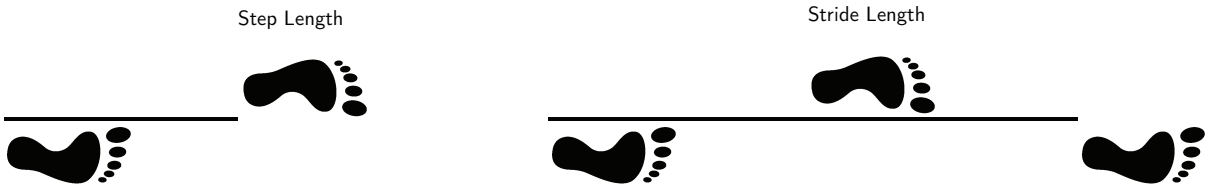

Figure 2.8: Stride length versus step length for a human

In previous work [6, 3, 1, 16] the term stride length is often wrongly used to denote the step length. The periodic frequency from the micro-Doppler signature is the step frequency, which will be used consistently through this report, and explained in relation to the micro-Doppler signature in Section 4.3.2.

Bipedal motion

Human motion is classified as *bipedal motion*. Some typical properties of the gait pattern is that each arm and leg will swing back and forth once during each gait cycle. The arms will swing in opposite phase to each other, and each leg will swing in phase with the opposite arm, and the torso and head will have a minor oscillation at twice the gait frequency. Figure 2.9 shows the two phases during a gait cycle: the stance and swing phase.

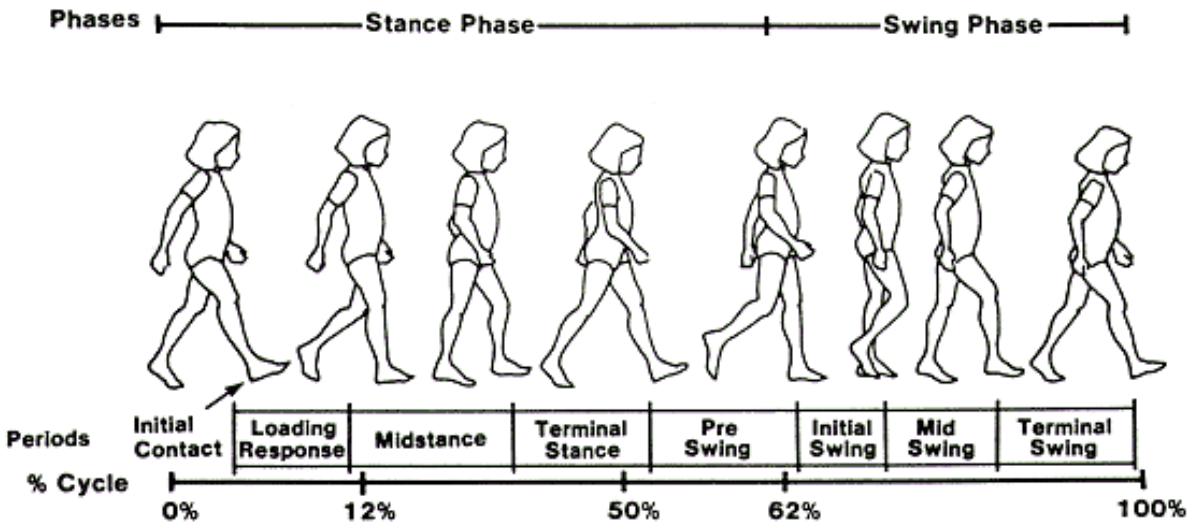

Figure 2.9: Human gait cycle [17]

A gait cycle starts when one foot gets initial contact with the ground, and last until the same foot, receives initial contact again [18]. During a gait cycle the arms and legs accelerate and decelerate relative to the torso. The arm and legs complete one period t_{gait}, each gait cycle.

Human gait cycle from point scatterer

The human gait cycle can be visualized by plotting the point scatter positions obtained from a mo-cap recording. The target movement file Λ in Figure 2.12 and 2.13 are from the Carnegie Mellon University Graphics Lab Motion Capture Database [11]. It contains a recording of a person walking at a steady pace, in a straight line. The placement of each maker on the human target is given by [19] and shown in Figures 2.10 and 2.11.

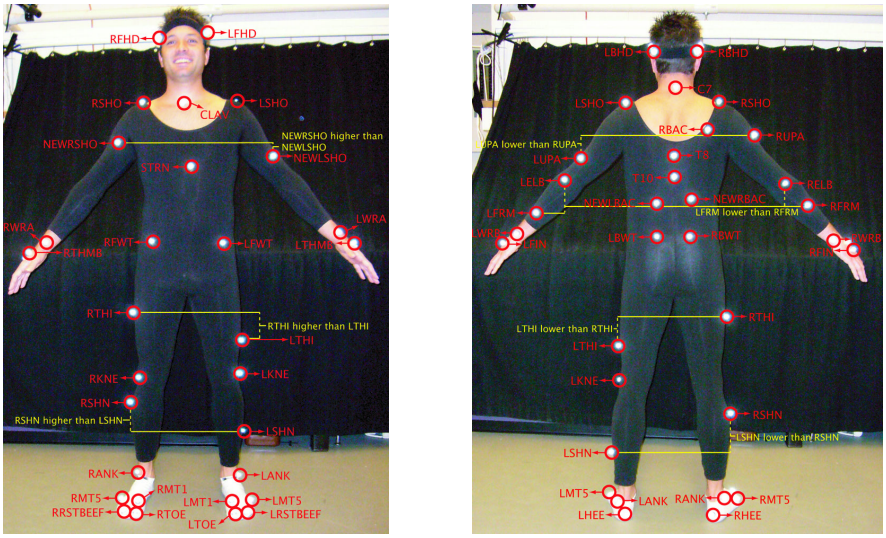

(a) Frontmarkers (b) Backmarkers

Figure 2.10: CMU Marker Placements for Front and Back [19]

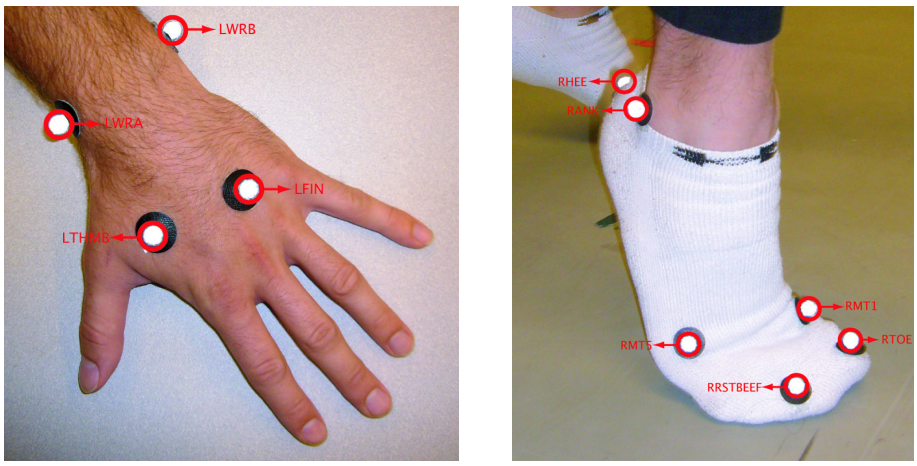

(a) Handmarkers (b) Footmarkers

Figure 2.11: CMU Marker Placements for Hands And Feets [19]

Figure 2.12 (a)-(i) shows the scatterer positions of a human performing one gait cycle of walking, viewed from the side. By plotting consecutive time steps, a human body can be identified.

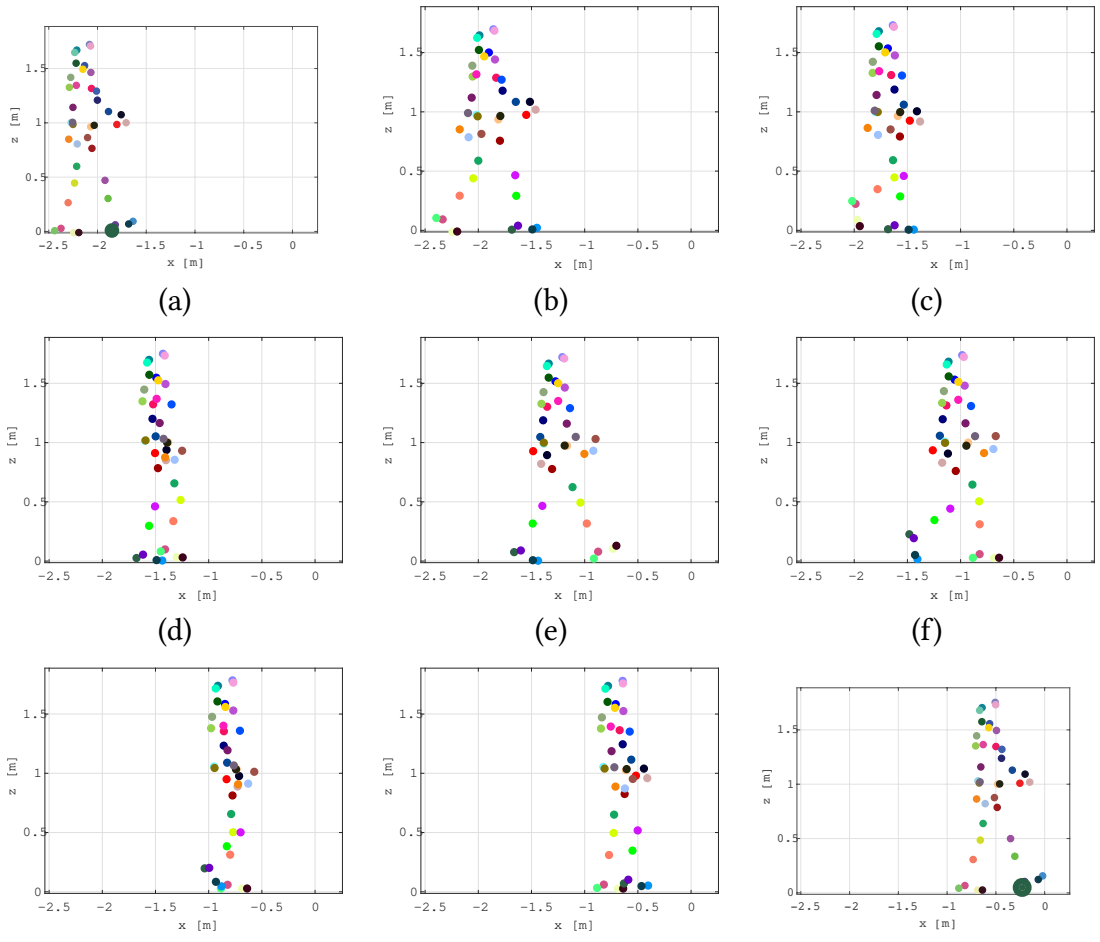

Figure 2.12: Point scatters of Human walking viewed from the side.

One complete gait cycle is performed in (a) through (i). The human target starts with the right foot in front of the left in (a). The right heel marker RHEE (dark green) is made bigger in (a) and (i) to illustrate that the heel starts and ends in the same position, relative to the human body, thus completing a gait cycle. Note that one gait cycle contains two steps. Figure 2.13 shows the range versus time for the recording in Figure 2.12.

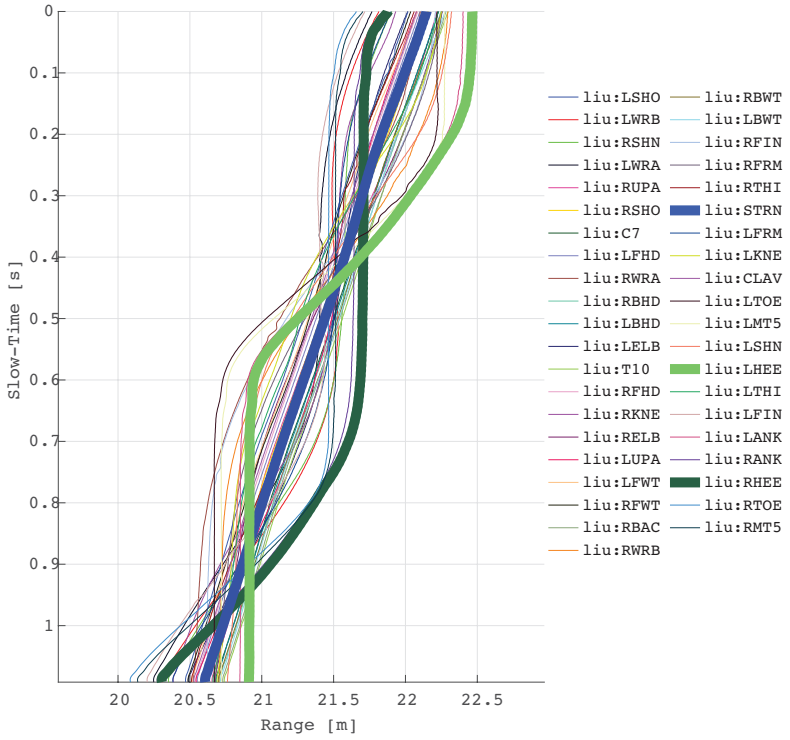

Figure 2.13: Range versus time for each scatter form a motion capture recording of a human walking.

The right heel marker RHEE (dark green), the left heel marker LHEE (light green) and the torso marker STRN (blue) are highlighted with a thicker line. It can be observed that RHEE and LHEE have a sinusoidal pattern, oscillating around a STRN, located in the middle. The sinusoidal curves are from the arm and legs of the human. The RHEE and LHEE markers are from the very edge of the right and left foot respectively, and therefore have the largest displacement during a stride. When a gait cycle is performed the feet move both in front and behind the torso, which explains the oscillations around the straight center lines. The LHEE and RHEE are in opposite phase, which corresponds to the gait pattern explained in Section 2.6. The STRN marker placed on the front torso has very little oscillations since the torso does not swing back and forth like the legs. The straight line equals a constant velocity. If the target velocity is changing, the the STRN line wound bend towards the left for acceleration and right when deceleration.

Figure 2.14 shows the Doppler frequency shift f_d for the same target. f_d is obtained by using Equation 2.4, and $\lambda = 0.0411$m. The same markers as in Figure 2.13 are highlighted in bold.

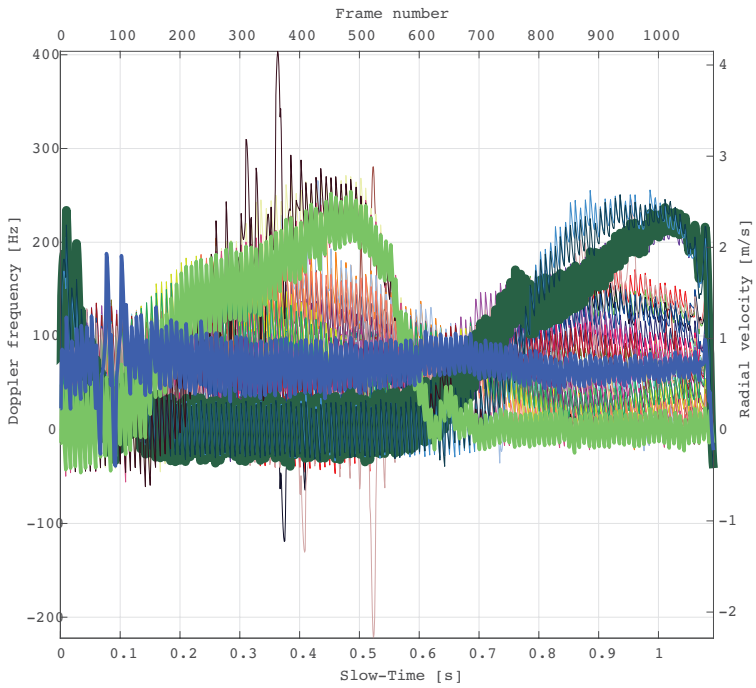

Figure 2.14: The Doppler frequency shift for each marked from a mo-cap of a Human waking toward the radar with $\psi = 0°$ performing 1 gait cycle.

It can be seen that the STRN marker has little Doppler frequency shift, which corresponds to the lack of oscillation, while the RHEE and LHEE markers have the largest Doppler shift which corresponds to the their large oscillations in Figure 2.13. Since the target movement file Λ for this, and all other obtained mo-cap recordings, contains very many markers, the plots become very cluttered.

Chen target movement model

To better illustrate the different phases of the gait cycle, from the Doppler frequency shift, the human target model created by Chen [6] is used below. It is based on empirical mathematical parameterizations derived from biomechanical experimental data from [7]. Similar to the mo-cap files this model provides the target simulator with x, y, z coordinates. The benefit of using this model is fewer scatterer, with clearly labeled names. This makes it easier to illustrate and explain key concepts through this report. The human model from Chen will also be used to verify and test the radar and feature extractor, as this is considered a very accurate target model. It will be explicitly stated when this model is used and when a mo-cap recording is used. Figure 2.15 shows the layout of the 17 point scatter used in the Chen human model.

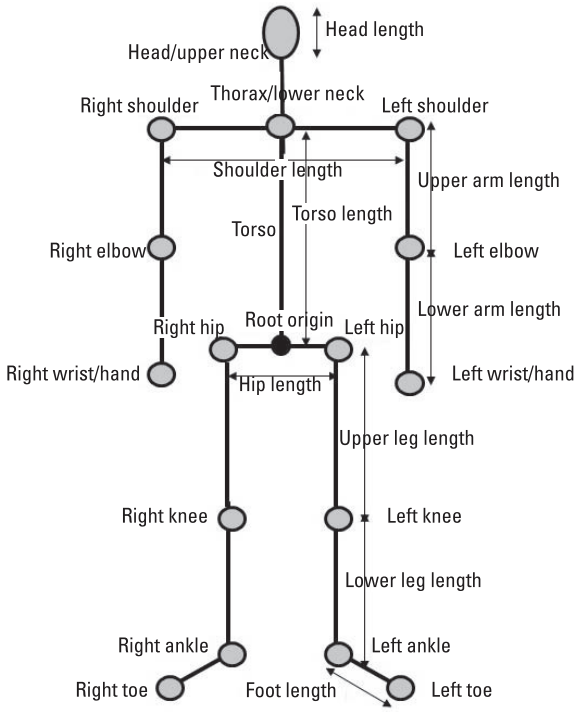

Figure 2.15: Chen point scatter model [6, p. 175]

It has a very similar marker layout to a mo-cap recording, where the human consist of multiple point scatterer. Figure 2.16 shows the Doppler frequency shift of the 17 point scatters from the Chen target movement model. This Figure shows a similar scenario as in Figure 2.14.

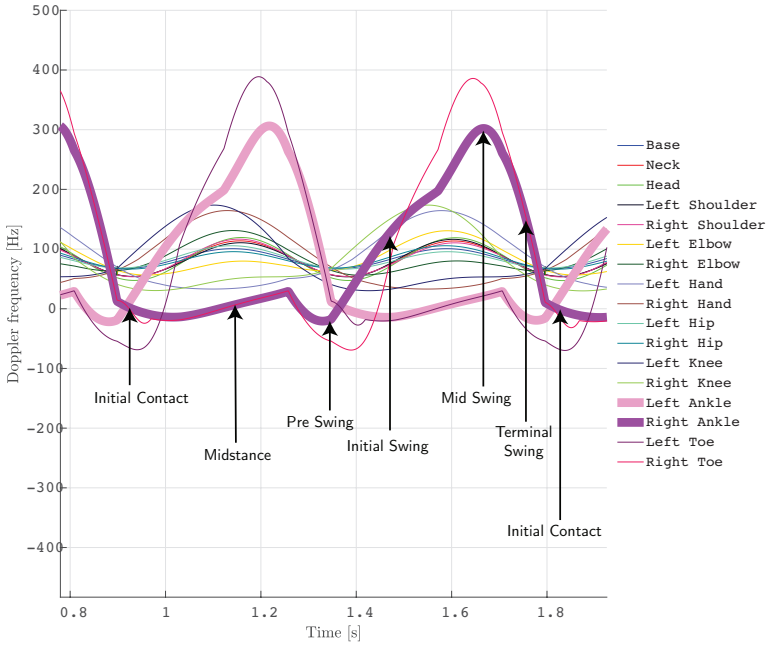

Figure 2.16: Doppler frequency shift of Human waking toward the radar with $\psi = 0°$ performing 1 gait cycle, based on the Chen target movement model.

A humans gait pattern can be determined from Figure 2.16. The Doppler frequency shift of the Right Ankle is highlighted in bold, and annotated with the different periods of the gait cycle from Figure 2.9. The Right Ankle will be used to describe the right foot, as it is located in center of the leg at the end of the foot. The Left Ankle is also highlighted in bold to be used as a reference to the Right Ankle. The gait cycle starts in the stance phase, at initial contact. Here the right foot just completed is previous gait cycle and touched the ground. At this point the right ankle is stationary, with $f_d = 0$ and hence $v_r = 0$. In the midstance period the left ankle performs its swing phase, while the right foot carries the weight of the human. At the end of the stance phase, in the pre-swing period, the right foot is located behind the target. The slight negative f_d happens since the feet are simulated to move slightly backwards at the end of each gait cycle. The swing phase starts with the initial swing period. Here the foot moves towards the radar, increasing its radial velocity. Mid-swing the right foot are centered under the torso, having its maximum radial velocity, with $f_d \approx 300$ Hz, making $v_r = 6.17$ m/s, by using Equation 2.4. Here $\lambda = 0.0411$ m. In the terminal swing phase the right foot is decelerated before touching the ground, and beginning a new gait cycle all over again.

2.6.1 Quadrupedal motion

Animals with four legs are quadrupeds. Their motion is classified as *quadrupedal motion*. Their gait pattern can be divided into two main groups: symmetric and asymmetric, with their subgroups given as

- Symmetric gait
  - Walk
  - Trot

  - Pace
- Asymmetric gait
  - Gallop

Gaits such as the walk, trot and pace are symmetric with the limbs on one side of the body repeating, repeating the motion of the limbs on the opposite side. The intervals between the footfalls is evenly spaced [15, Ch. 91]. Figure 2.17 illustrates one gait cycle of a walking dog, showing the opposite phase its front and rear legs.

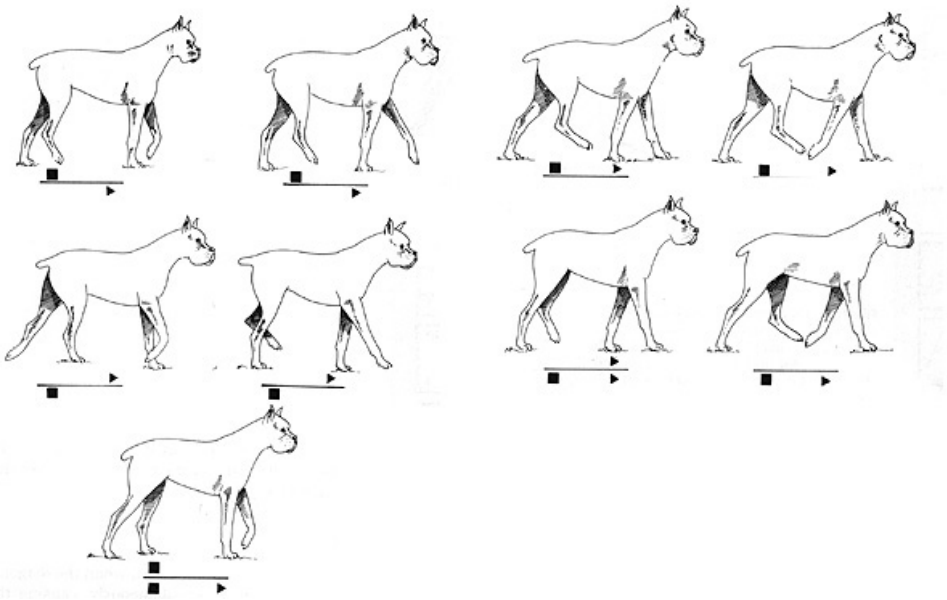

Figure 2.17: A dog performing one gait cycle of walking [15, Ch. 91]

The footprint pattern shown below demonstrates which foot is on the ground during a gait cycle. Symmetric quadrupedal motion have many of the same features as bipedal motion. Each leg will swing back and forth once each gait cycle, legs on the left side in opposite phase with the right ones, and the rear legs in phase with the opposite front leg. The head and torso will have the same minor oscillation at twice the gait frequency.

Gallop is an asymmetric gait used for high-speed locomotion. During a gallop the limb movements of one side does not follow the other side.

Dog gait cycle from point scatterer

A dogs gait cycle can be visualized in a similar way as the human gait cycle. The target movement file Λ used for the dog target in this Section is obtained from [20]. Figure 2.18 (a)-(i) shows the scatterers of a dog performing on gait cycle of gallop, view from the side.

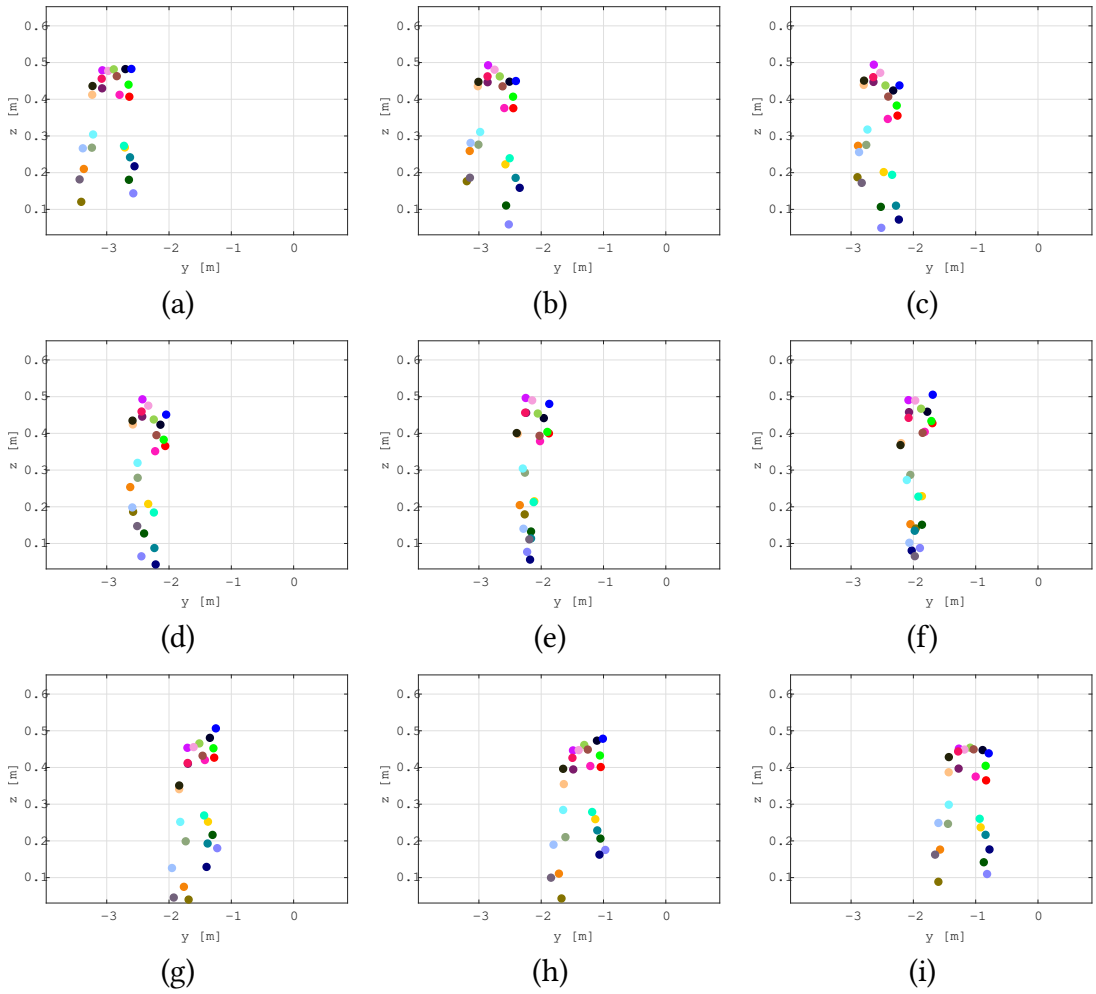

Figure 2.18: Point scatters of a Dog galloping viewed from the side.

In (a) the torso is located in the cluster at the top, with the head on the right side, pointing in the positive y direction. The the front and rear legs can be seen underneath. The left and right legs move with the same phase, and touch the ground at the same time in (b) through (c). In (d) through (g) the front and rear legs are centered under the torso, preparing for a new jump. In (g) through (i) the dog kicks off with the rear legs and completes the gallop gait cycle. Figure 2.19 shows the range vs time for the scatterer in Figure 2.18.

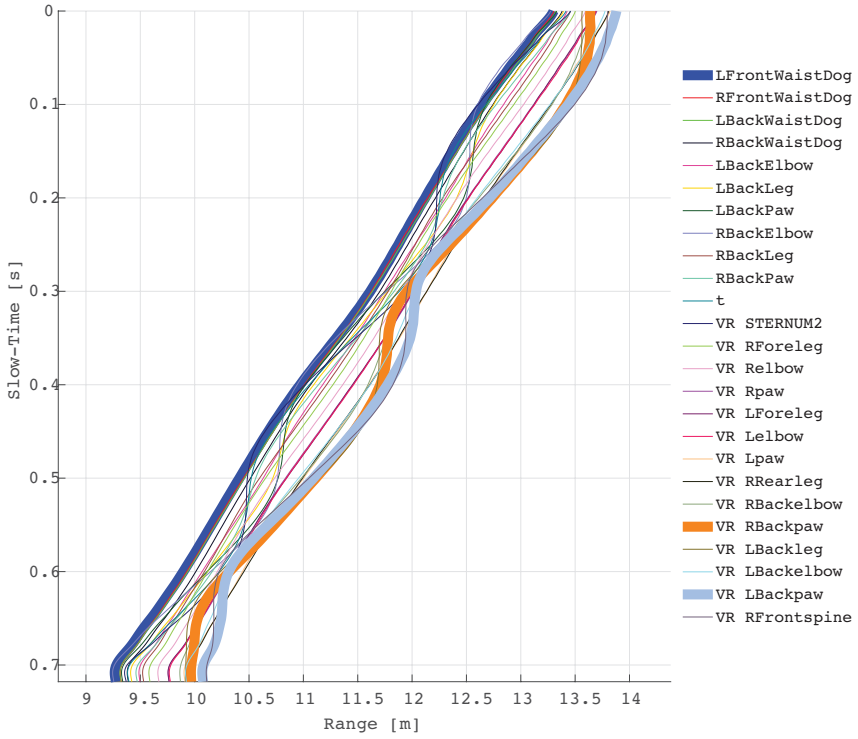

Figure 2.19: Range vs time for a mo-cap recording of a dog galloping towards the radar with $\psi = 0$.

The Left Front Waist marker (dark blue), the Right Back Paw (orange) and the Left Back Paw (gray) are highlighted with a bold line. It can be seen that the waist marker is located in front of the rear paw scatterer, since the dog has a larger range span from the head to tail, that the thickness of a human. The left and rear paws oscillate at the step frequency f_m, but since the dog is galloping, the left and right side are in phase. Figure 2.20 shows the Doppler frequency shift of the scatterer in Figure 2.18, with the same markers highlighted as in Figure 2.19.

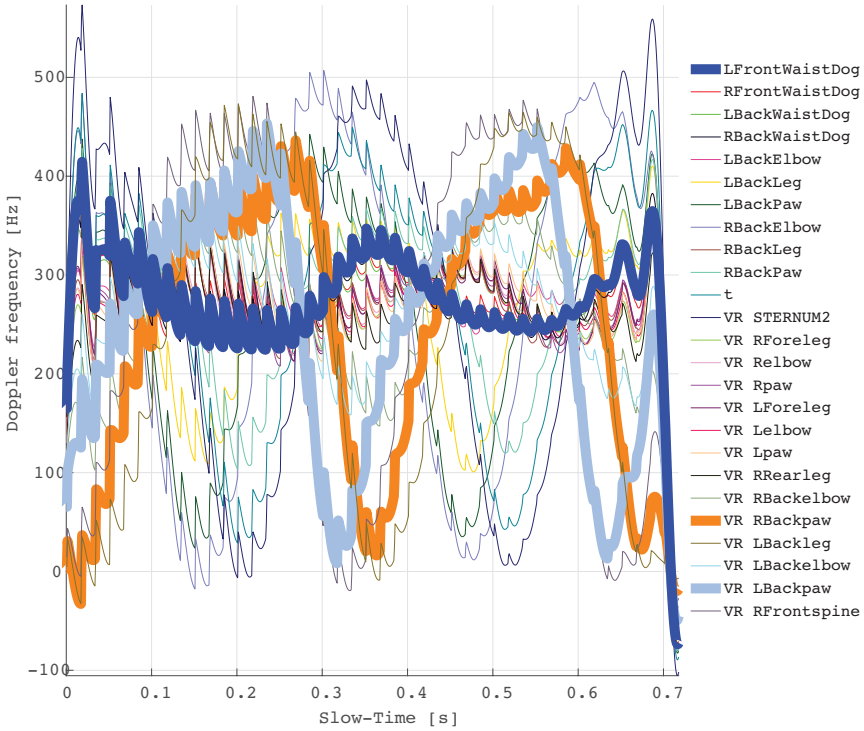

Figure 2.20: Doppler frequency shift for a mo-cap recording of a dog galloping towards the radar with $\psi = 0$.

The Left Front Waist marker has some more oscillations that the torso for a human. When looking at the same Left Front Waist marker (dark blue) in Figure 2.18, it can be seen to oscillate up and down, following the dogs head then galloping. The dog has a radial velocity $v_r \approx 3$ m/s, as can be seen on the right vertical axis. The Right Back Paw (orange) and the Left Back Paw (gray) vary in velocity, and at about 0.4 seconds into the recording both have a Doppler frequency $f_d \approx 0$, indicating that the feet are stationary. This corresponds to the phase right before the back legs kick off the ground.

Chapter 3

Radar Simulator

A pulsed radar transmits EM energy to its surroundings. This reflects off objects and a portion of the transmitted energy is returned to the radar, called *backscattering*. The radar measures the time delay and energy of the backscatter. The time delay determines the objects range R and the RCS σ determines the returned energy. Both these parameters are given to the radar simulator module, as is illustrated in Figure 3.1.

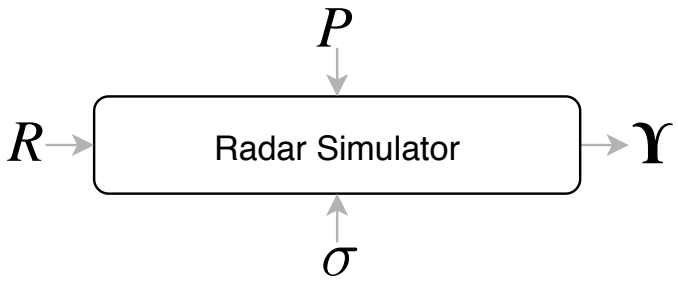

Figure 3.1: Radar simulator module

The radar parameters P, which determine how the radar operates are given in Table 5.1, and will be explained throughout this chapter.

Table 3.1: Radar parameters P

Symbol	Parameter	Unit
f_c	Carrier frequency	Hz
f_s	Receiver sampling frequency	Hz
f_p	Pulse repetition frequency (PRF)	Hz
G_{rx}	Receiver amplifier gain	dB
G_t	Transmit antenna gain	dBi
G_r	Receive antenna gain	dBi
τ	Pulse duration	seconds
P_t	Peak transmit power	W
θ	Transmit pulse phase	rad

Since the radar parameters are given as inputs to the radar simulator module, it can be used to simulate a wide variety of pulsed radars, by simply changing P.

Pulsed radars emit short and powerful EM pulses, and waits for an echo signal reflecting of objects, in the receive time. A new pulse is transmitted every *pulse repetition interval (PRI)* T. This makes the transmission rate of new pulses, called the *pulse repetition frequency (PRF)* f_p, as

$$f_p = \frac{1}{T}. \qquad \text{[Hz]} \quad (3.1)$$

In Figure 3.2 three pulses are illustrated as the gray rectangles.

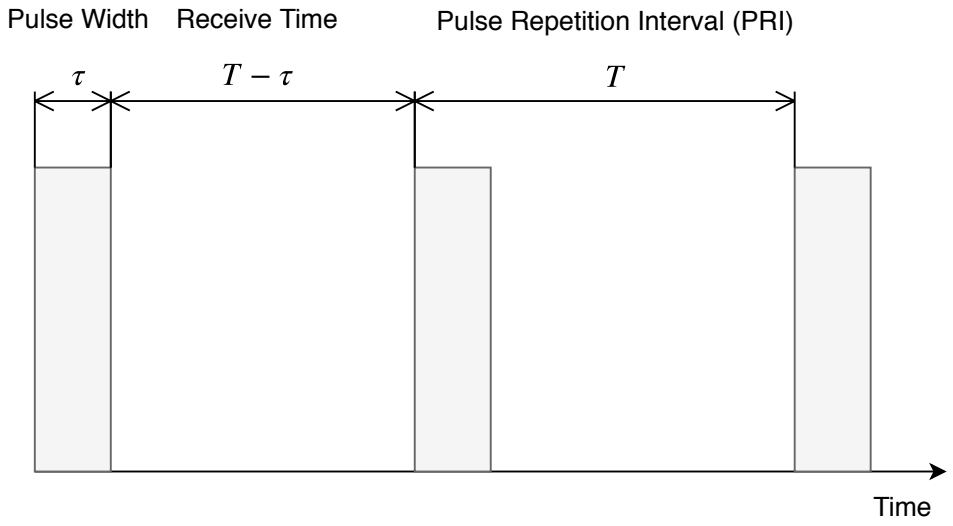

Figure 3.2: Pulsed radar transmit and receive intervals

The *pulse duration* or *pulse width* is the time the radar transmits, and is denoted τ. The receive time is defined as $(T - \tau)$. Pulsed radars are characterized by $\tau \ll (T - \tau)$, meaning that the pulse width is very short compared to the receive time.

The output of the radar simulator module is the *radar data matrix* $\boldsymbol{\Upsilon}$, representing data captured along two time dimensions: the *fast-time* and the *slow-time*, as illustrated in Figure 3.3.

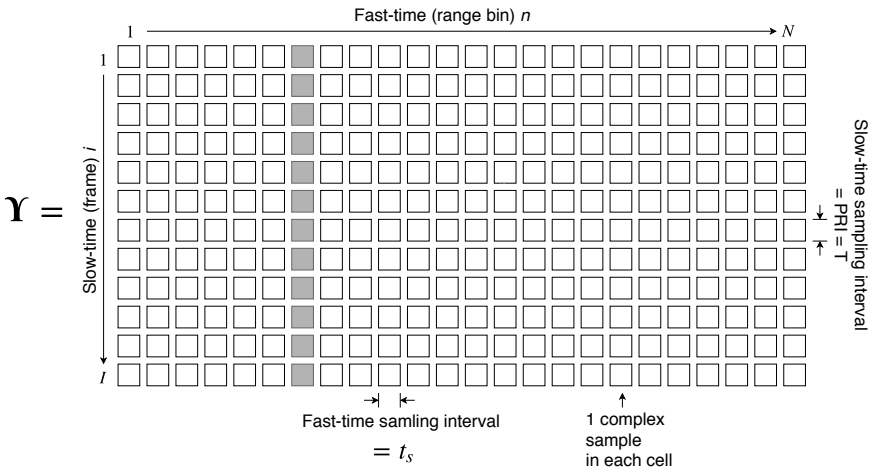

Figure 3.3: Two-dimensional radar data matrix $\boldsymbol{\Upsilon}$. The shaded samples are the slow-time signal for the seventh range bin, $\Upsilon_i[7]$ for $i = 1, 2, 3, \cdots, I$ where I is the number of frames in the simulation.

- In the fast-time dimension the received backscattering is digitized by the radar receivers analog-to-digital converter (ADC) at a sampling rate $f_s = 1/t_s$. t_s is the time between each captured sample, and typically $t_s \ll T$, hence the fast-time name. One *fast time vector* is created for every pulse transmitted. It is indexed with the subscript $n = 1, 2, 3 \cdots, N$, where N is the number of samples, called *range bins*. One fast-time vector, illustrated as a row in Figure 3.3 is called a *frame*, which will be explained in Section 3.3.1.
- The slow-time dimensions is made up of multiple sequential frames arranged in a matrix as illustrated in Figure 3.3. A column makes up one *slow-time vector*, where each sample is from the same range bin, n. Each frame is indexed with the subscript i where $i = 1, 2, 3, \cdots, I$, and I is the number of frames in a recording. A new frame is captured during every PRI, making the sampling rate in the slow-time dimension the pulse repetition frequency (PRF), as will be explained in Section 3.4.

The collection of I frames, each with N range bins make up the radar data matrix $\boldsymbol{\Upsilon}$. Each square is a sample, containing a complex number representing the backscattering from that range bin and frame. The total amount of time represented by $\boldsymbol{\Upsilon}$, in the slow time dimension, is the duration of the entire recording in seconds, defined as the *observation time* $T_o = I \cdot T$.

3.1 Radar Cross Section Modeling

RCS σ is a measure of how detectable an object is by radar, where a large RCS indicates that an object is more easily detectable. The RCS is dependent of the size, geometry and material of the target, the carrier frequency and the aspect angle of the target, relative to the radar [6, p. 52].

Using point scatterer to describe the target, allows for a very simple EM scattering model. The EM scattering occurs when a target is illuminated by a EM wave. This induces electric and magnetic currents on the surface and/or within the volume of the target, which generates a backscattering EM wave. Both the radar antennas and the point scatterer are modeled as *isotropic* radiators and reflectors, respectively. This means that they emit and reflect the same intensity in all directions. This allows the targets RCS σ to be given by a constant value, where the RCS of each scatterer is given as

$$\sigma_l = \frac{\sigma}{L} \qquad [\mathrm{m}^2] \quad (3.2)$$

where σ_l is the RCS for the l point scatterer. The major disadvantage with this is that every point scatterer gets the same RCS. This is obviously not accurate since, for instance, a torso is much larger than a single foot, but they are each represented by a single point scatterer. This could be solved by a system for partitioning the RCS based on which body part the scatterer represents. Then the torso and head would receive a large fraction of σ compared to a scatterer representing a foot or a hand. Such a system is not implemented in this project, since different mo-cap recordings organize the markers differently. Hence it is very difficult to automatically determine which body part each marker represents. For each target a constant σ is heuristically determined based on RCS values from [2, p. 64]:

Table 3.2: Target RCS

Target	σ
Human	$1\ m^2$
Dog	$0.2\ m^2$

This simplification is done to limit the scope of this project, since a RCS study would use considerable time. In additional the actual σ values are not important in this project, since only the difference in RCS between the human and dogs is used.

3.2 Description of a pulsed radar signal

To understand how a pulsed radar works, it is necessary to understand the fundamental property of Fourier analysis. Most important is that the time and frequency scales have an inverse relationship to each other. The longer a signal is in time, the shorter is the corresponding frequency spectrum and vice versa. To accurately describe the transmitted and received signal, four increasingly long time and wide frequency scales are introduced, given in Table 3.3.

Table 3.3: Pulse radar signal time and frequency scales

	Time scale [s]	Frequency scale [Hz]
1	Carrier wave period, t_c	Carrier frequency, $f_c = 1/t_c$
2	Pulse duration, τ	Pulse bandwidth, $B = 1/\tau$
3	Pulse Repetition Interval, T	Pulse Repetition Frequency, $f_p = 1/T$
4	Coherent Processing Interval, T_d	Spectral line bandwidth, $\propto 1/T_d$

The first time and frequency scale is used to describe the period of the sinusoidal carrier wave, with a frequency f_c and a period of $t_c = 1/f_c$. To generate a pulsed signal the second time scale defines the pulse durations τ which limits the signal in time, illustrated in Figure 3.4. Here a rectangular pulse is centered around $t = 0$ with a pulse duration τ. The amplitude of the signal is A.

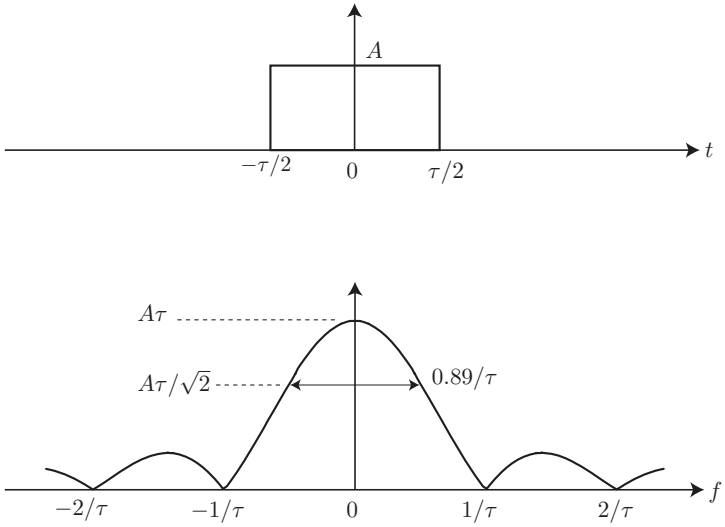

Figure 3.4: Single rectangular pulse and its spectrum [21, p. 278]

In the frequency domain a time limited pulse gets a bandwidth B which is inversely proportional to the pulse duration, as $B = 1/\tau$. The *main lobe* of the spectrum in Figure 3.4 is defined to be between $-1/\tau$ and $1/\tau$. The other lobes outside is the *sidelobes*. The bandwidth B of the main lobe can be described using several different metrics. A common convention in radar is to use the *half-power bandwidth*. This is the two sided bandwidth measured at an amplitude corresponding to half the peak power, given by a 3 dB reduction from peak power. In this report B will be used to denote the half-power bandwidth, given as $B = A\tau/\sqrt{2}$. The third time scale is introduced by transmitting a new pulse every T seconds. Multiple pulses is needed to be able to detect the Doppler frequency shift of a target, which will be explained in Section 3.4. The fourth time scale is introduced to limit the number of pulses transmitted, since it is impossible to transmit infinitely many pulses. The transmitted pulses are truncated to a finite pulse train of total duration T_d, called the *coherent processing interval (CPI)*. The coherent processing interval (CPI) determines the Doppler resolution, which is explained in Section 3.4.3. By putting all this together we are able to fully describe the transmitted pulse generated by the radar in general terms as

$$x(t) = A \cdot p(t) \cdot \cos(2\pi f_c t). \tag{3.3}$$

where A is the amplitude, $p(t)$ is a pulse shape function and $\cos(2\pi f_c t)$ is the carrier wave modulating the pulses, as shown in Figure 3.5.

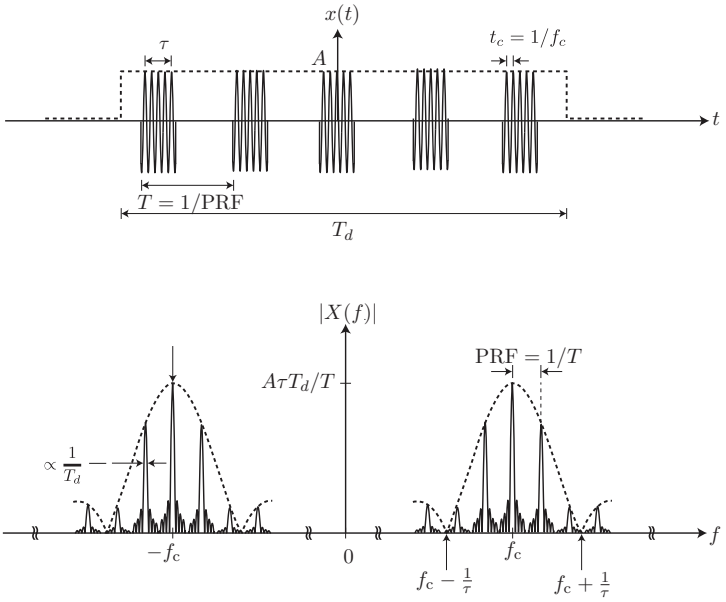

Figure 3.5: Finite modulated pulse train with a rectangular pulse shape function [21, p. 278].

3.3 Fast-Time Dimension

Each PRI, one pulse is transmitted and one frame is captured. The frame capture process makes up the fast-time dimension, which is explained in the following section.

3.3.1 Frame Capture

To describe the transmitted $s(t)$ and received signal $r(t)$ it is helpful to introduce the concept of frames. One frame is the digitized part of the echoes from one transmitted pulse. Each frame spans a limited distance in space. This spatial limitations is illustrated in Figure 3.6. Each letter Ⓐ-Ⓒ is used to connect the space and time dimensions together, in Figure 3.6 and 3.7. The events marked with the same letter happens at the same time/ range.

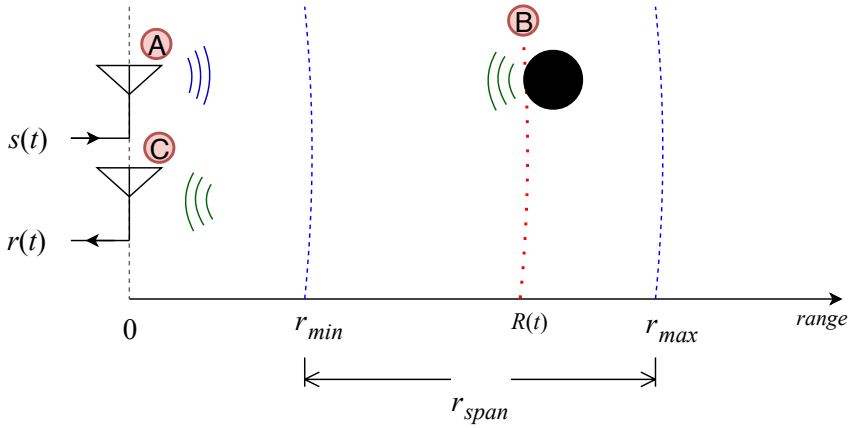

Figure 3.6: Radar frame in the spatial domain

Each frame spans r_{span} meters, where $r_{span} = r_{max} - r_{min}$. r_{min} is the minimum range, and r_{max} is the maximum range. Hence only scatterer with range $r_{min} < R(t) < r_{max}$ will be part

of the frame. The added t in $R(t)$ is used to denote the time dependence of the range. Figure 3.7 illustrates the timeline for one frame.

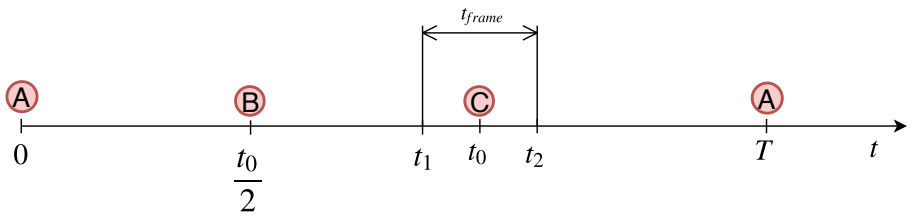

Figure 3.7: Radar frame in the time domain

At (A) when $t = 0$ the radar begins transmitting $s(t)$. At (B) when $t = \frac{t_0}{2}$ the signal reflects of a scatterer. t_0 propagation delay of the signal given by

$$t_0 = \frac{2}{c}R(t). \quad \text{[s]} \quad (3.4)$$

At $t = t_1$ the ADC in the receiver starts sampling the returned echo signal, where t_1 is given as

$$t_1 = 2\frac{r_{min}}{c}. \quad \text{[s]} \quad (3.5)$$

The ADC captures a sample every t_s seconds until N samples are captured. This happens at $t_2 = t_1 + Nt_s$, where t_2 is given by

$$t_2 = 2\frac{r_{min} + r_{span}}{c}. \quad \text{[s]} \quad (3.6)$$

The duration of one frame t_{frame} is given as

$$t_{frame} = t_2 - t_1 = \frac{r_{span}}{c}. \quad \text{[s]} \quad (3.7)$$

At (C) when $t = t_0$ the echo from the scatterer returns to the receiver. $t_1 < t_0 < t_2$ must be true if the scatterer echo is going to be sampled by the ADC and be part of the frame. When $t = T$ the next signal starts transmitting, and the frame capture cycle starts over again.

3.3.2 The Transmitted Pulse

The ith pulse transmitted can be written as

$$s_i(t) = A \cdot p(t - iT) \cdot Re\{e^{j\theta}e^{j2\pi f_c(t-iT)}\} \quad \text{[V]} \quad (3.8)$$

where A is the transmit amplitude, $p(t)$ is the *pulse shape function* limiting the effective bandwidth of the transmitted pulse, f_c is the carrier frequency and θ is the phase of the signal. $p(t)$ is a Gaussian pulse shape function given as

$$p(t) = \exp\left(-\frac{t^2}{2\tau^2}\right) \quad (3.9)$$

where τ is the *pulse width*. It has the characteristic that the time and frequency domain of the pulse have equal shapes, as illustrated in Figure 3.8

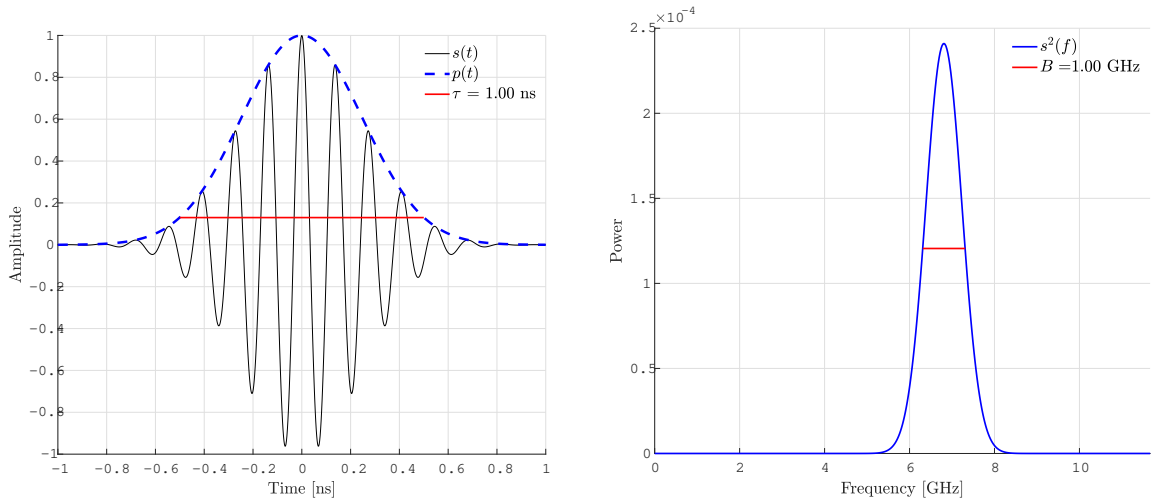

(a) (b)

Figure 3.8: (a) $s(t)$ modulated with Gaussian pulse shape with $\tau = 1$ ns. (b) The frequency power spectrum of $s(t)$, with a half-power bandwidth $B = 1$ GHz. $f_c = 7.2$ GHz.

In (a) the blue dotted line is the pulse shape function $p(t)$ creating the envelope of the transmitted signal $s(t)$. In (b) is the corresponding frequency power spectrum, with a *half-power bandwidth* $B = 1$GHz. The pulse width is given as $\tau = 1/B = 1$ns.

To simplify the notation in Equation 3.8 the local time frame variable t_f is defined as

$$t_f = t - iT \quad t_f \in [0, T]. \qquad [\text{s}] \quad (3.10)$$

By inserting Equation 3.10 into 3.8, the ith pulse can be written as

$$s_i(t_f) = A \cdot p(t_f) \cdot Re\{e^{j\theta} e^{j2\pi f_c t_f}\}. \qquad [\text{V}] \quad (3.11)$$

3.3.3 The Received Pulse

The received signal $r(t)$ equals the transmitted signal $s(t)$ with some distortion, noise, amplitude attenuation, phase shift and a propagation delay based on the target range. The following derivations are given for one point scatterer for each frame. The returned echo from a single target for the ith frame is a delayed version of $s_i(t_f)$ given in Equation 3.11. When disregarding the distortion and noise the received signal $r_i(t_f)$ is given as

$$r_i(t_f) = s_i(t_f - t_0) \qquad [\text{V}] \quad (3.12a)$$

$$= A' \cdot p\left(t_f - t_0\right) \cdot Re\left\{e^{j\theta'} e^{j2\pi f_c t_f}\right\} \qquad [\text{V}] \quad (3.12b)$$

where t_0 is the two-way propagation delay for the current frame. Comparing equation 3.12 with 3.11, it can be seen that the received signal $r_i(tf)$ has a new amplitude A', a time delay t_0 and a phase shift θ'. These are parameters a pulse-Doppler radar measures.

The propagation delay for the ith frame is given by

$$t_0 = \frac{2R(t_f + iT)}{c}. \qquad [\text{s}] \quad (3.13)$$

The received phase θ' can be found by multiplying the terms of the cosine in Equation 3.12b, and removing the $2\pi f_c t_s$ term , which gives

$$\theta' = \theta - \frac{4\pi}{\lambda} R(t_f + iT). \qquad \text{[rad]} \quad (3.14)$$

This phase shift is extremely important in *coherent* radar signal processing. A radar with a coherent receiver is able to measure the phase difference between the transmitted and received signal. It gives the radar the ability to measure sub-wavelength changes in range, from the Doppler frequency shift [6, p. 19]. If a target travels with a constant velocity, the rate of change of its phase will be constant. If the target accelerates or decelerate, the rate of change of the phase will vary accordingly. These two factors are the key to Doppler and micro-Doppler estimation in pulse-Doppler radars and is explained in Section 3.4.

Propagation Loss

The received amplitude A' is less than A, mainly due to propagation loss, and is given by

$$A' = \frac{A}{L(t_f)} \qquad \text{[V]} \quad (3.15)$$

where $L(t_f)$ is the free-space path loss (FSPL) amplitude ratio. The FSPL is the loss in signal strength of an EM wave that would result from a line-of-sight path through *free space*, with no obstacles nearby to cause reflection or diffraction. Free space is defined as a perfect vacuum, that is, a space free of all matter. The FSPL amplitude ratio is given by

$$L(t_f) = \sqrt{\frac{|P_t|}{|P_r|}} \quad (3.16)$$

where P_t and P_r is the transmitted and received signal power, respectively. P_r is given by the radar range equation [21, p. 64] as

$$P_r = \frac{P_t G_t G_r \lambda^2 \sigma}{(4\pi)^3 R_t^2 R_r^2} \qquad \text{[W]} \quad (3.17)$$

where G_t and G_r is the gain of the transmitter (Tx) and receiver (Rx) antenna respectively, λ is the wavelength of f_c, σ is the radar cross-section of the target and R_r,R_t is the range from the Tx and Rx antenna respectively. The Tx and Rx antenna is assumed to be *isotropic radiators*, meaning they transmit and received equal power in all directions.

Since the radar is monostatic the range to and from the target is equal, and R_t^2 and R_r^2 can be combined to $R(t_f)^4$. Equation 3.17 then becomes

$$P_r(t) = \frac{P_t G_t G_r \lambda^2 \sigma}{(4\pi)^3 R(t_f)^4}. \qquad \text{[W]} \quad (3.18)$$

By inserting Equation 3.18 into 3.15 the FSPL ratio can be given as

$$L(t_f) = \sqrt{\frac{(4\pi)^3 R(t_f)^4}{G_t G_r \lambda^2 \sigma}} \quad (3.19)$$

3.3.4 Digitizing the signal

The signal is digitized by sampling at $t_1 + nt_s$ where t_1 is the frame offset time, and t_s is the sampling period of the ADC, with a corresponding sampling frequency $f_s = 1/t_s$. According to the sampling theorem $f_s \geq 2f_{max}$, where $f_{max} \approx f_c + B/2$ is the maximum frequency of $r_i(t)$.

Every PRI, N samples are digitized, making up one frame. N is given by

$$N = \left\lceil \frac{2 \cdot r_{span}}{c \cdot t_s} \right\rceil \tag{3.20}$$

and the distance between each sample is

$$\Delta R = \frac{c}{2} t_s. \quad \text{[m]} \tag{3.21}$$

Figure 3.9 shows a frame, where each gray box represents a sample in that frame.

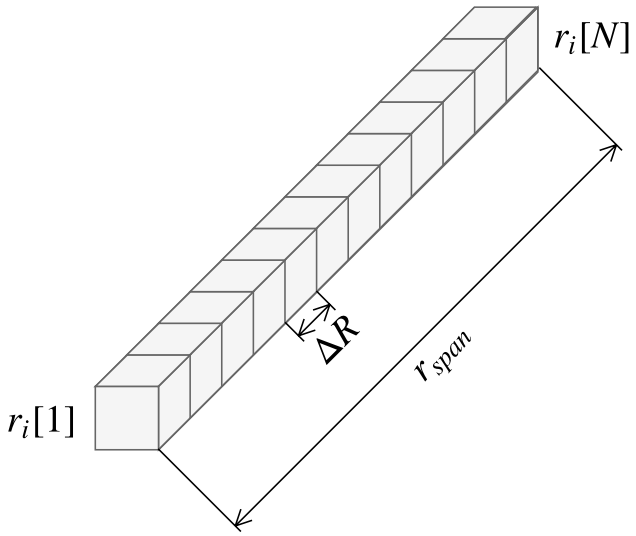

Figure 3.9: N range bins in a frame, with ΔR meters between each range bin.

Its range interval is equal to r_{span}, from $r_{min} = ct_1/2$ to $r_{max} = ct_2/2$. Each sample in the frame is refereed to as a by several names, including *range bin*, *range cell*, and *fast-time sample*. The term *range bin* will be used through this report. The digitized signal is given by

$$\begin{aligned} r_i[n] &= s_i(t_1 + nt_s) \\ &= \frac{A}{L(t_1 + nt_s)} \cdot p\left(t_1 + nt_s - \frac{R(t_1 + nt_s + iT)}{c}\right) \\ &\cdot Re\{e^{j\theta'} e^{j2\pi f_c(t_1 + nt_s)}\}. \end{aligned} \tag{3.22}$$

The expression above can be simplified by the *"stop and hop"* assumption [21, p. 288] [22], whereby it is assumed that $v_r \ll c$, meaning the target movement while the pulse is in flight is negligible. This simplifies the range expression as

$$R(t_1 + nt_s + iT) \approx R(iT), \quad \text{[m]} \tag{3.23}$$

which is the same as assuming that the range to the target will be constant throughout the frame.

This simplification is also the reason why the Doppler frequency shift cannot be measured from only one frame, which will be explained in Section 3.4. We use this simplification to write Equation 3.13 as

$$t_0 = \frac{2R(iT)}{c}. \qquad [\text{s}] \quad (3.24)$$

Similarly the phase change is simplified to

$$\theta' = \theta - \frac{4\pi}{\lambda} R(iT). \qquad [\text{rad}] \quad (3.25)$$

Substituting Equation 3.24 and 3.25 into 3.22 the digitized received signal becomes

$$r_i[n] \approx \frac{A}{L(t_1 + nt_s)} \cdot p\left(t_1 + nt_s - t_0\right) \cdot Re\{e^{j\theta'} e^{j2\pi f_c(t_1+nt_s)}\} \quad (3.26)$$

3.3.5 Digital Down-Conversion

Down-Conversion of $r_i[n]$ removes the carrier frequency f_c of the signal. The resulting signal is centered around 0 Hz, called the *baseband* or *video signal*. This significantly lowers the maximum frequency of the signal, which makes processing in hardware a lot simpler. Digital down-conversion (DDC) can easily be performed by multiplying $r_i[n]$ with a complex conjugated phasor with the same frequency as $r_i[n]$. The down-converted signal $r_{i,bbu}[n]$ is given as

$$r_{i,bbu}[n] = r_i[n] \cdot Re\{e^{-j2\pi f_c(t_1+nt_s)}\} \quad (3.27a)$$

Figure 3.10 shows the power frequency spectrum of the received signal $r_i[n]$ before and after down-conversion.

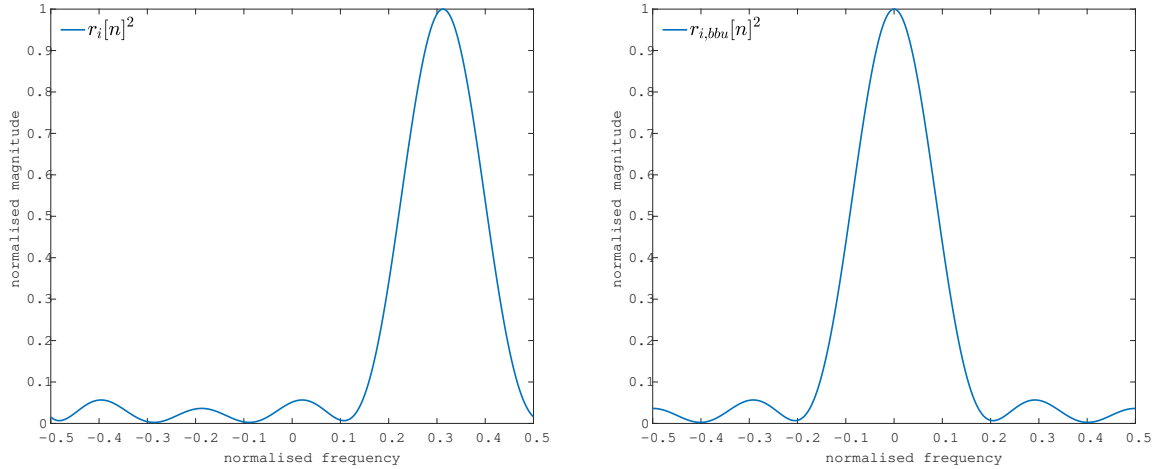

(a) (b)

Figure 3.10: Signal before (a) and after (b) DDC

In (a) the $r_i[n]$ signal is centered around the carrier frequency f_c, whereas in (b) the carrier frequency is removed, and the signal is centered around 0 Hz.

3.3.6 Radar Simulator Output

The equation for the received signal has only been valid for one scatterer this far. The received signal can be expressed as the superposition of each scatterer from each target. As mentioned earlier, a scenario contains X targets, each with L_χ scatterer, where the subscript χ is used to separate the number of scatterer for each target. The nth range bin in the ith frame denoted as $\Upsilon_i[n]$ is expressed as

$$\Upsilon_i[n] = \sum_{\chi=1}^{X} \sum_{l=1}^{L_\chi} r_{i,bbu}[n] \tag{3.28a}$$

$$= \sum_{\chi=1}^{X} \sum_{l=1}^{L_\chi} \frac{A}{L(t_1 + nt_s)} \cdot p\left(t_1 + nt_s - \frac{2R_{\chi,l}(iT)}{c}\right) \cdot \exp\left(\frac{-j4\pi}{\lambda} R_{\chi,l}(iT)\right) \tag{3.28b}$$

where $R_{\chi,l}(iT)$ is the range to the lth point scatterer for the χth target.

3.4 Slow-Time Dimension

The received signal $r_{i,bbu}[n]$ is as mentioned in Section 3.3.4, derived with the assumption that the target range is constant for each frame, and hence does not create a Doppler frequency shift in the returned echo. To measure the Doppler frequency shift from a single pulse of width τ generally requires that there be at least one cycle of the Doppler frequency f_d within the pulse; or that $f_d > 1/\tau$ [2, p. 109]. This means the Doppler frequency shift of the target must be greater the bandwidth of the transmitted signal.

The Doppler frequency shift is captured along the slow-time dimension, consisting of multiple consecutive frames. The number of frames used in the Doppler processing is determined by the CPI, T_d. The length of the CPI determines the *Doppler resolution*, which is the smallest Doppler frequency shift the radar can reliably discern. This will be explained in Section 3.4.3. First, a Doppler signal model is introduced, which shows how the Doppler frequency shift is extracted across the slow-time dimension.

3.4.1 The Doppler Signal

Suppose a target is illuminated by the radar at a certain range bin over a CPI of M frames, where $M \leq I$. The target has a radial velocity, v_r, making the range to the target, when the mth pulse ($1 \leq m \leq M$) is transmitted, as $R - mv_rT$ meters. Similar to Equation 3.14, the phase shift of the mth pulse will be $(-4\pi/\lambda)(R - v_rmT)$ radians. When the received signal is sampled at $t = 2R + mT$, the measured output for the mth pulse will be

$$\begin{aligned} \Upsilon_m &= A' \exp\{j[\theta - (4\pi/\lambda)(R - v_rmT)]\} \\ &= A' \exp\left\{j\left[2\pi(\frac{2v_r}{\lambda})(iT) + \theta - (\frac{4\pi R}{\lambda})\right]\right\} \quad 1 \leq m \leq M \\ &= A' \exp[j(2\pi f_d mT + \theta')]. \end{aligned} \tag{3.29}$$

From Equation 3.29 it is clear that measuring the phase of successive pulse echoes, forms a discrete-time complex sinusoid at the expected Doppler frequency f_d. Doppler frequency measured in this way, from a series of phase measurements is called *spatial Doppler* [21,

p. 292]. Figure 3.11 (a) shows the spatial Doppler for a CPI of 10 frames, while (b) shows the same signal with a CPI of 31 frames, with a PRF $f_p = 300$ Hz.

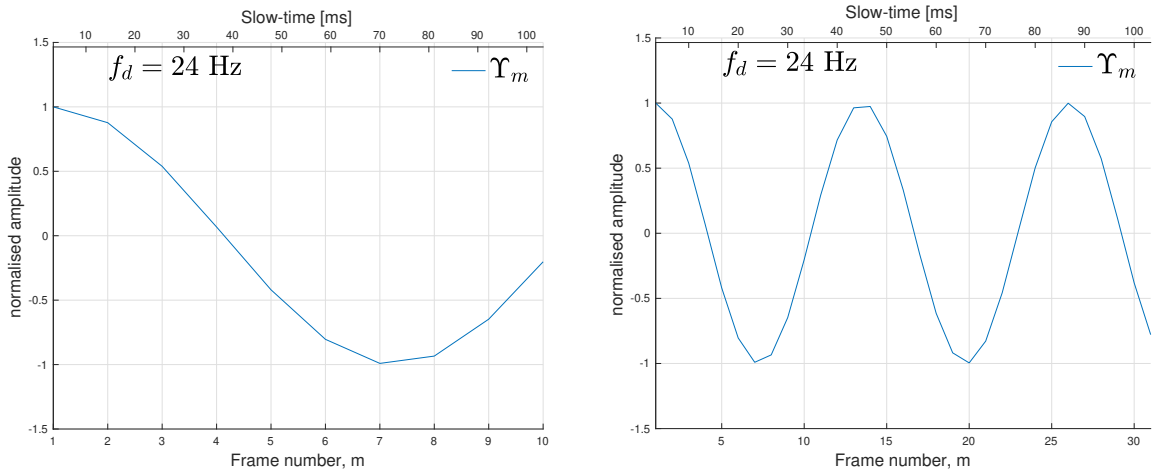

(a) (b)

Figure 3.11: Spatial Doppler with a $f_p = 300$ Hz. In (a) the CPI consist of 10 frames and in (b) 31 frames.

Both figures are from the same target, which has a Doppler frequency shift $f_d = 24$ Hz. In (a) the CPI is to short to capture one period of the spatial Doppler signal, while in (b) a longer CPI captures about two periods of the spatial Doppler. The more periods in the Doppler signal, the better resolution is obtained in the Doppler frequency spectrum, which will be explained in Section 3.4.3.

3.4.2 The Doppler Spectrum

The Doppler spectrum of a range bin is the discrete-time Fourier transform (DTFT) of the slow-time dimension data, at that range bin. Figure 3.12 shows an illustration of the components in a Doppler spectrum.

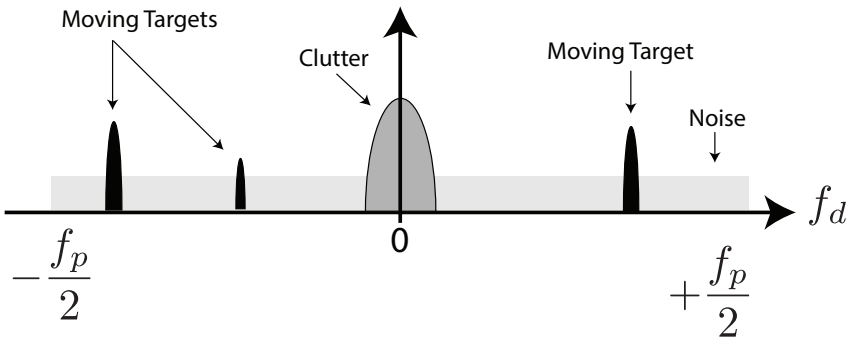

Figure 3.12: Range-Doppler frequency spectrum

The spectrum is periodic with half the Doppler sampling sample rate $f_p/2$. This determines the maximum Doppler frequency which can be detected. The Doppler frequency shifts of targets outside this range will alias to an apparent Doppler of $f_d + qf_p$, where the integer q is chosen such that the results fall in the range $\pm f_p/2$. From the Doppler spectrum the following signals are observed:

- White receiver noise spread uniformly across the entire spectrum.
- Stationary objects are located at $f_d = 0$ Hz. Unwanted echoes are called *clutter*.
- Moving targets get a Doppler frequency shift according to Equation 2.4. The two targets on the left side have a negative Doppler frequency shift, and hence are moving away from the radar, while the target on the right side is approaching the radar. Their individual amplitudes relative to the noise are determined by their individual signal to noise ratio (SNR).

3.4.3 Doppler Resolution

When multiple targets are present within the same range bins, with about the same velocities their spectrum peaks will overlap. The minimum velocity/Doppler frequency difference between the two targets, which allows their individual Doppler peaks to be distinguished is determined by the *Doppler resolution*. It is determined by *spatial Doppler bandwidth* B_r [21, p. 283], given as

$$B_r = \frac{1}{T_d} = \frac{f_p}{M}. \qquad \text{[Hz]} \quad (3.30)$$

where M is the number of frames in the CPI. B_r is estimated from the *Rayleigh criterion*, when applied to the Doppler domain it states that two point targets are resolvable when the peak of the DTFT of one target falls on the first null of the second target [21, p. 783]. Figure 3.13 illustrates the Doppler resolution for a scenario with two targets separated by different Doppler frequency shift.

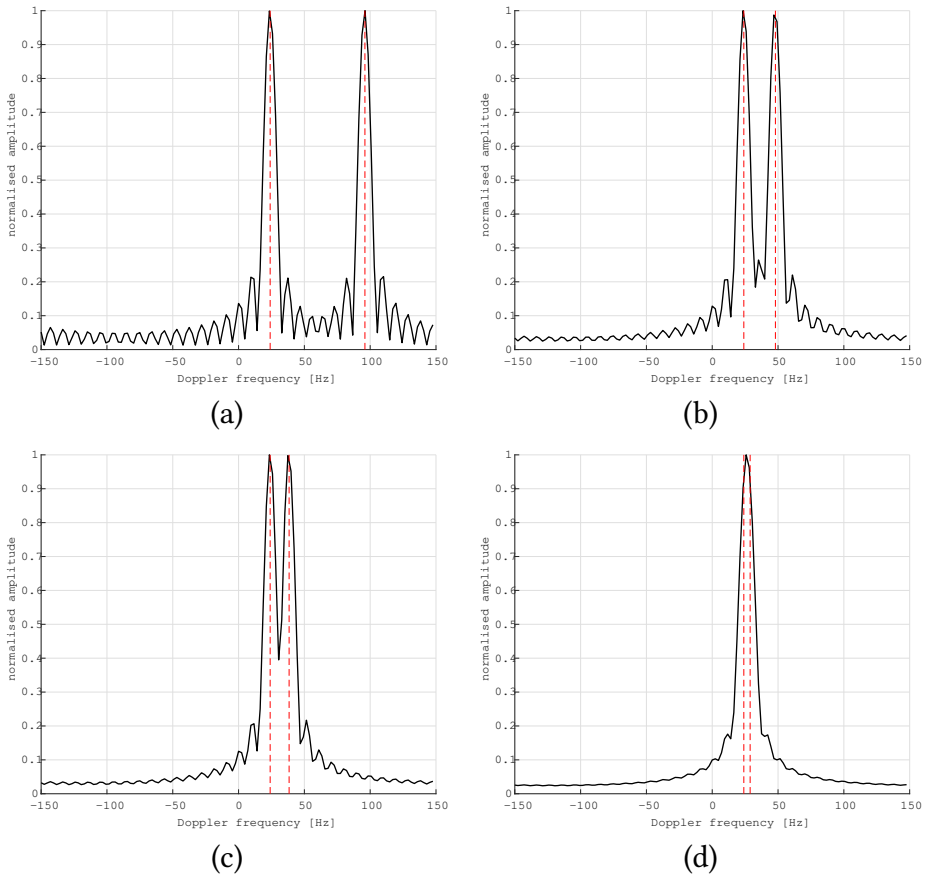

Figure 3.13: Two targets at different Doppler frequency shift. Individual spectral lines have $B_r = 10$ Hz, and zero relative phase. The Doppler spacing is (a) 72 Hz (b) 24 Hz (c) 14 Hz (d) 5 Hz

The plots are created with $f_c = 7.2$ GHz, PRF $f_p = 300$ Hz, $\tau = 1$ ns and a CPI $T_d = 0.1$s and $M = 31$ frames. This makes $B_r = 10$ Hz, which is the smallest difference in Doppler frequency that can be determined. In (a) and (b) the sidelobes of one spectrum affects the sidelobes and main lobe of the other. Still the two frequencies components are obvious, as illustrated by the vertical red dotted line. In (c) the two targets peaks begin to blend together. In (d) the Doppler spacing is 5 Hz which is less than $B_r = 10$Hz, hence the frequency components cannot be individually distinguished.

These, two different targets can be reliably separable when their Doppler frequency spectrum peaks are spaced at least the single-pulse bandwidth. From Equation 3.30 it shows that the Doppler resolution is determined by the CPI, T_d, and that the Doppler resolution increase with increasing CPI.

3.5 Radar Data Matrix

The output of the radar simulator is the *radar data matrix* $\boldsymbol{\Upsilon}$, which contains I frames, each with N samples. Figure 3.14b shows $\boldsymbol{\Upsilon}$ from obtained from the range values in Figure 3.14a.

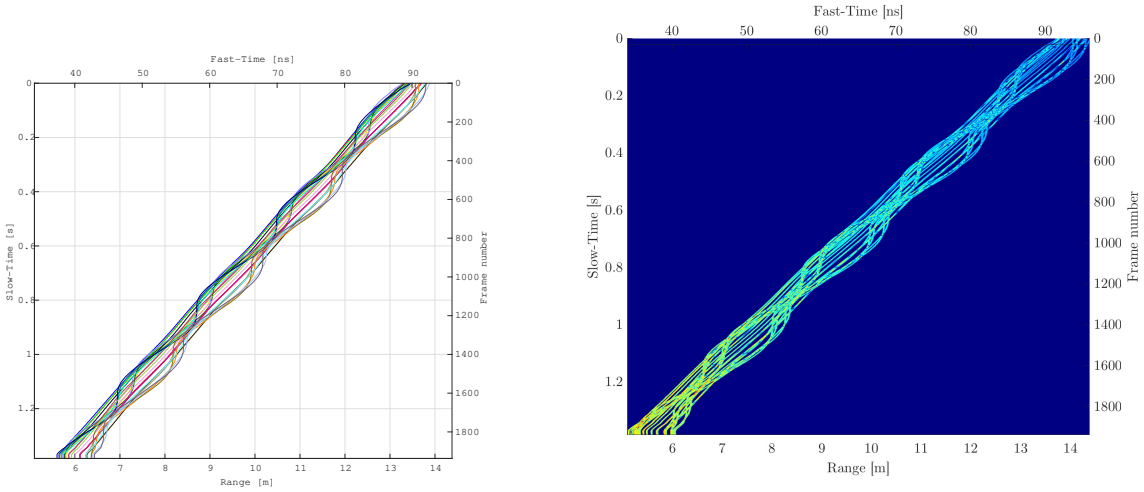

(a) (b)

Figure 3.14: Mo-cap recording of a dog galloping towards the radar, $\psi = 0°$.

It can be seen that the target starts at about 14 m, and walks with a constant velocity towards the radar, where each line represents one scatterer. The simulation is about 1.3 seconds, with $I = 1938$ frames, and $N = 162$ range bins. The propagations loss is shown be the color, where a brighter color represents a stronger echo. The closer the target is to the radar, the stronger the echo becomes.

Figure 3.15 shows $\boldsymbol{\Upsilon}$ for a scenario of two Human targets crossing each other path. Λ is two mo-cap recordings form [11].

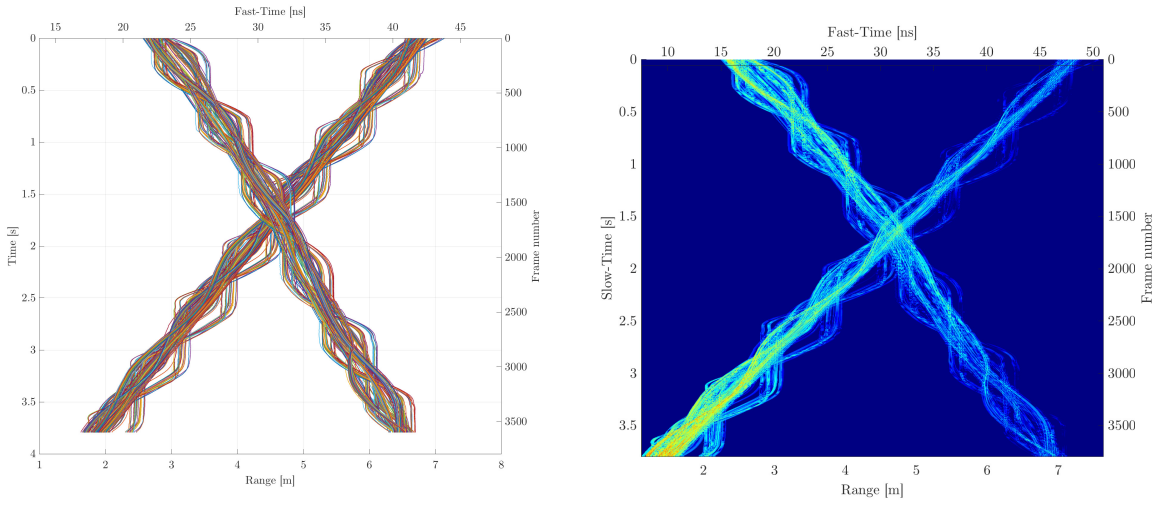

(a) (b)

Figure 3.15: Two humans walking towards the radar, crossing paths.

The range R for both targets is shown in (a), and the corresponding $\boldsymbol{\Upsilon}$ in (b). The target received power increase with shorter range.

Chapter 4

Feature Extraction

The purpose of the feature extraction module is to perform the time-frequency analysis of Υ to obtain the micro-Doppler signature matrix $\boldsymbol{\mu}$ and performed a feature extraction. A time-frequency analysis separates stationary and moving objects in the Doppler dimension. This allows a moving target to be detected even in high stationary clutter environments such as in forests, or inside houses.

Using $\boldsymbol{\mu}$ and/or $\boldsymbol{D}$ directly in a classifier would require a very large input, and hence make the classifier very complex. A much smaller data set can be obtained by performing feature extraction on the $\boldsymbol{D}$ matrix, resulting in a few parameters, which more compactly describes each target class.

4.1 Feature Extraction Overview

Figure 4.1 shows an overview of the Feature Extractor module. It takes the radar data matrix Υ as input, and outputs a Feature-Set vector F for all targets in Υ.

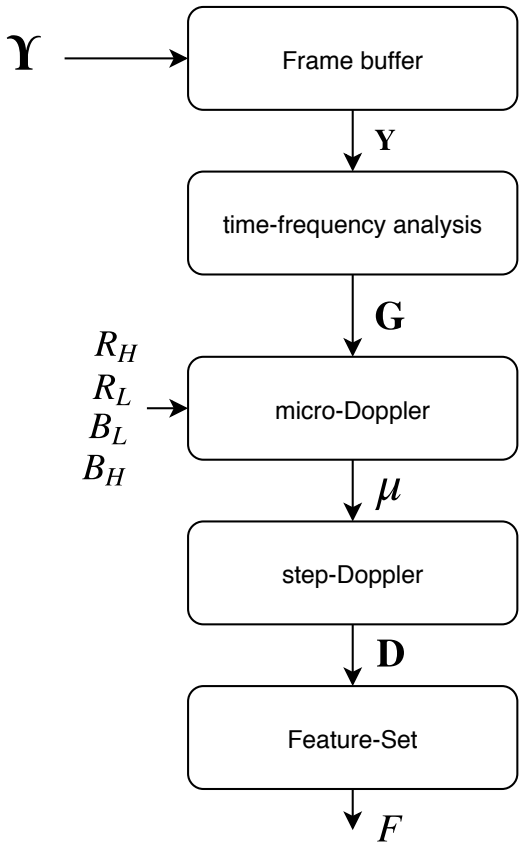

Figure 4.1: Feature Extractor Overview

A brief explanation of the feature extractor module is given as follows:

- In *framebuffer*, the radar data matrix $\boldsymbol{\Upsilon}$ is resolved into multiple smaller segments of M consecutive frames, called the Framebuffer $\boldsymbol{Y}$. The length of each frame buffer equals the CPI, spanning $M \cdot T$ seconds. The Framebuffer operates as a sliding window, used for the time-frequency analysis.
- A *time-frequency analysis* is performed by taking the discrete Fourier transform (DFT) of each slow-time column in each framebuffer $\boldsymbol{Y}$. Taking the Fourier transform over sliding windows this way is called the short-time Fourier transform (STFT). It extracts the time-varying Doppler frequency from each framebuffer and creates one range-Doppler matrix $\boldsymbol{G}$ for each framebuffer.
- The *micro-Doppler signature matrix* $\boldsymbol{\mu}$, is obtained by summing the cells in $\boldsymbol{G}$ containing a target. Each target is located inside a *range and bandwidth gate* given by R_H, R_L, B_H, B_L. Where R_H and R_L is the maximum and minimum target range in $\boldsymbol{G}$, and B_H and B_L is the max/min Doppler frequency shift, respectively. The range gating is explained in Section 4.3.1.
- The *Step-Doppler matrix* $\boldsymbol{D}$ is obtained by taking the DFT of each row in $\boldsymbol{\mu}$. This extracts the frequency of the periodic targets movements.
- The *Feature-Set* F, contains six values extracted from $\boldsymbol{D}$, which describes features such as a targets radial velocity v_m, micro-Doppler bandwidth B_μ, step length L_m, step-harmonic frequency ratios β_1, β_2 and gait amplitude ratio ρ. These will be explained in Section 4.5.

To best illustrate the feature extraction process, the figures showing simulation results in this chapter will use the human motion model developed by Chen [6], as mentioned in Section 2.2, and not mo-cap data. The mo-cap data contains very many scatterers and hence the plots become very cluttered. The model by Chen uses only 17 point scatterer, each named with the body part they represent. This makes it easier to explain and verify the correctness of the feature extractor. Similar to mo-cap data the model by Chen provides x, y, z coordinates to the target simulator.

The feature extraction plots in this chapter belong to the same scenario of a human walking towards the radar. It was generated with $f_p = 1000$ Hz, $M = 100$ frames, $N = 1189$ range bins, $f_s = 23$ GS/s, and $f_c = 7.2$ GHz. Figure 4.9a is an exception from this, as it is a dog scenario, used to show the effect of normalization in $\boldsymbol{\mu}$.

4.2 Time-Frequency Analysis

4.2.1 Framebuffer

A framebuffer $\boldsymbol{Y}$ is created to provide the sliding window for the time-frequency analysis. For each frame, a framebuffer containing M frames is defined, with the ith frame being the center row. The framebuffer is symmetric, with $\lfloor M/2 \rfloor$ frames on either side of the ith frame. The total amount of time MT, in the slow-time dimension in each framebuffer equals the CPI. The framebuffer matrix $\mathbf{Y}_i$ for the ith frame is given by

$$\mathbf{Y}_i = \begin{bmatrix} y_{1,1} & y_{1,2} & \cdots & y_{1,N} \\ y_{1,1} & y_{1,2} & \cdots & y_{1,N} \\ \vdots & \vdots & \ddots & \vdots \\ y_{\lfloor \frac{M+1}{2} \rfloor,1} & y_{\lfloor \frac{M+1}{2} \rfloor,2} & \cdots & y_{\lfloor \frac{M+1}{2} \rfloor,N} \\ \vdots & \vdots & \ddots & \vdots \\ y_{M,1} & y_{M,2} & \cdots & y_{M,N} \end{bmatrix} \tag{4.1}$$

where M is the number of frames in the framebuffer and

$$y_{m,n} = \boldsymbol{\Upsilon}[i + m - \left\lfloor \frac{M+1}{2} \right\rfloor, n] \tag{4.2}$$

Each row contains one frame with the center row, $\lfloor (M+1)/2 \rfloor$ containing frame $\Upsilon_i[n]$, for $n = 1, 2, 3, \cdots, N$. M must be a odd number, such that the number of frames on each side of Υ_i is equal. The frame buffer in Figure 4.2, is marked with gray samples, where the current frame $\Upsilon_i[n]$ (always center frame) is red.

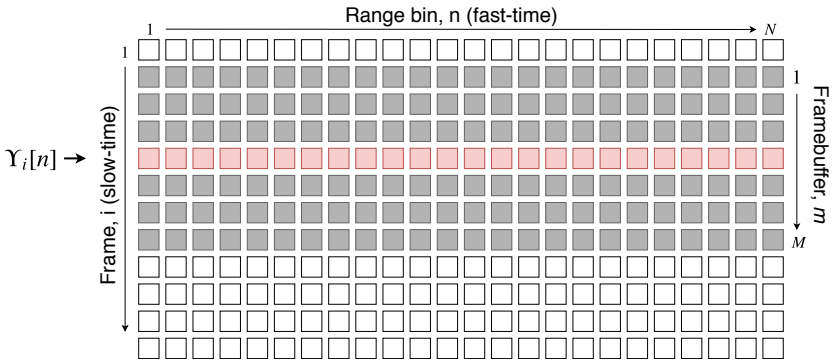

Figure 4.2: The gray and red squares make up the framebuffer $\boldsymbol{Y}_4$ with $M = 7$ frames and $N = 24$ range bins. The center row in the framebuffer $\boldsymbol{Y}_i$ is $\Upsilon_i[n]$.

The framebuffer $\boldsymbol{Y}_i$ obtained from frame i where $\left\lfloor \frac{M+1}{2} \right\rfloor > i > I - \left\lfloor \frac{M+1}{2} \right\rfloor$ does not have enough surrounding frames to fill the framebuffer, and hence is filled with frames of value zero, called *zero padding*.

Framebuffer length

The number of frames M in each framebuffer will determine the time-frequency resolution of the STFT. A larger M will give a better frequency resolution but decrease time resolution, and vice versa. The number of frames in the framebuffer $\boldsymbol{Y}$ is given by

$$M = \lceil T_d \cdot f_p \rceil \tag{4.3}$$

Appendix A show how the size of M affects the micro-Doppler signature matrix $\boldsymbol{\mu}$ (a), the step-Doppler matrix $\boldsymbol{D}$ (b) and the step-Doppler spectrum D_g (c). The best T_d is obtained when the peaks of f_m, f_2 and f_3 are most prominent. It can be observed in Figure A.1 that $T_d = 1$ s gives a too poor frequency resolution, such that f_m, f_2 and f_3 cannot be detected in D_g. The same argument applies to $T_d = 0.5$ s in Figure A.2. A $T_d = 0.3$ s or 0.1 s is found to give the most prominent peaks in D_g as shown in Figure A.3 and A.4. Reducing T_d beyond 0.1 s does not provide more prominent peaks in D_g, observed in Figure A.5 and A.6.

Spectral leakage

Each column in the framebuffer $\boldsymbol{Y}_i$ is multiplied with a Gaussian window, as given in Equation 4.6, to reduce *spectral leakage*, hence reducing *sidelobe* levels in the Doppler frequency spectrum. The window weights are given by

$$w[m] = \exp\left(-\frac{1}{2}\left(\frac{m - (M/2)}{\sigma_w(M/2)}\right)^2\right) \quad m = 1, 2, 3, \cdots, M \tag{4.4}$$

where σ_w decides the steepness of the Gaussian window. The steepness should be chosen to attenuated the signal as little as possible, while still decaying sufficiently towards the end, to reduce the sidelobes by as much as possible. Figure 4.3 shows $w[m]$ and its frequency magnitude spectrum.

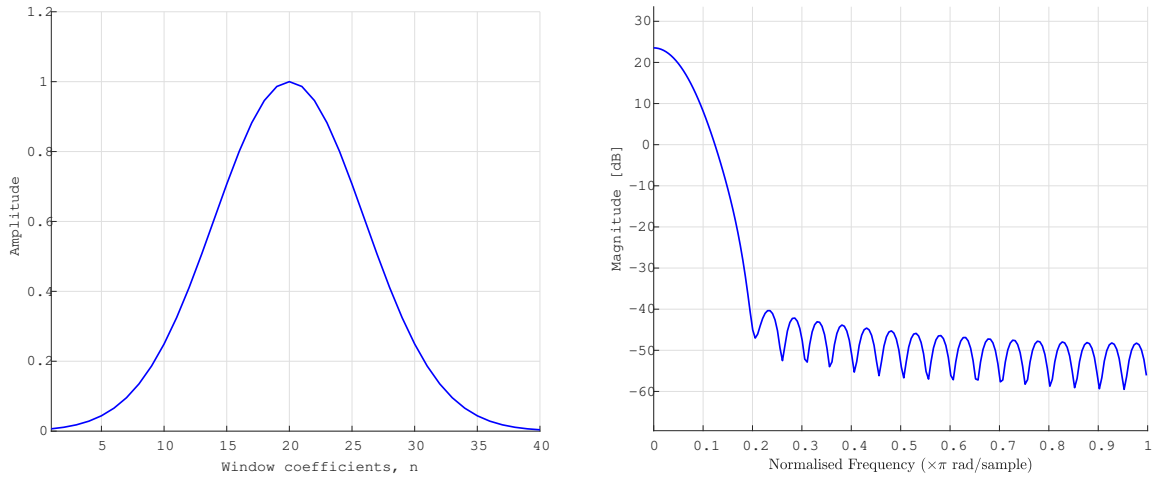

(a) (b)

Figure 4.3: In (a) Gaussian window time domain and in (b) the corresponding frequency magnitude spectrum.

Here $M = 40$ and $\sigma_w = 0.3$, which gives a relative sidelobe attenuation of -65.4 dB.

4.2.2 Range-Doppler spectrum

The range-Doppler spectrum $\boldsymbol{G}_i$ is the magnitude squared DFT of all the frames in a range bin in a framebuffer matrix $\boldsymbol{Y}_i$. $\boldsymbol{G}_i$ is computed using the fast Fourier transform (FFT) algorithm on each column, as illustrated in Figure 4.4.

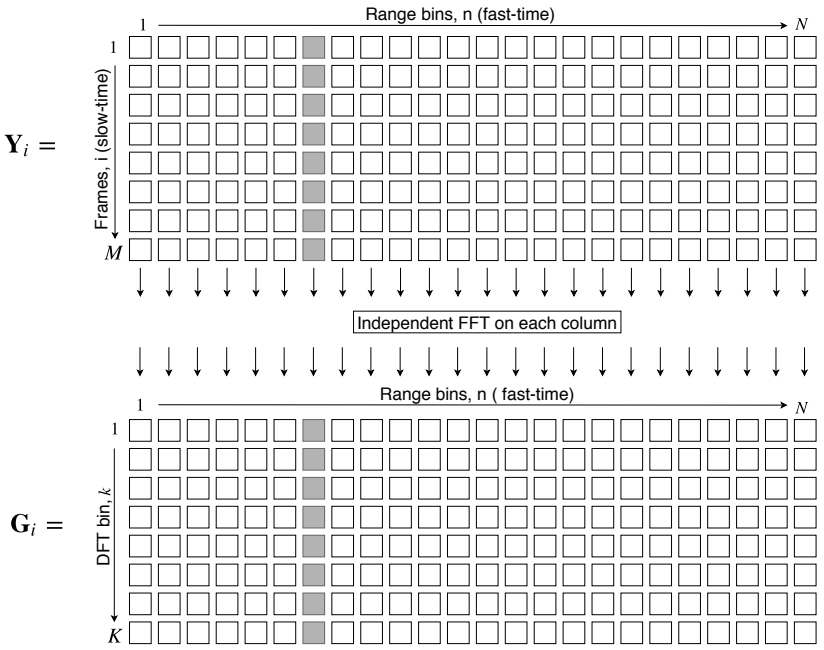

Figure 4.4: Conversion of the fast-time/slow-time framebuffer matrix $\boldsymbol{Y}_i$ to a range-Doppler matrix by applying a FFT on each slow-time row.

Each slow-time row is an independent FFT computation, where $K \geq M$. The DFT bins 1 through K corresponds to frequencies $-f_p/2$ to $+f_p/2$. The range-Doppler matrix $\boldsymbol{G}_i$ for the

ith frame is given by

$$\mathbf{G}_i = \begin{bmatrix} g_{1,1} & g_{1,2} & \cdots & g_{1,N} \\ g_{2,1} & g_{2,2} & \cdots & g_{2,N} \\ \vdots & \vdots & \ddots & \vdots \\ g_{K,1} & g_{K,2} & \cdots & g_{K,N} \end{bmatrix} \tag{4.5}$$

where

$$g_{k,n} = \left| \sum_{m=1}^{M} w[m] \cdot y_{m,n} \cdot \exp\left(-\frac{j2\pi km}{M} \right) \right|^2 \quad k = 1, 2, 3, \cdots, K \tag{4.6}$$

Figure 4.5 shows a range-Doppler matrix for a Human target walking toward the radar. The DFT is computed with $K = M$ frequency bins, and the radar parameters are explained in the end of Section 4.1.

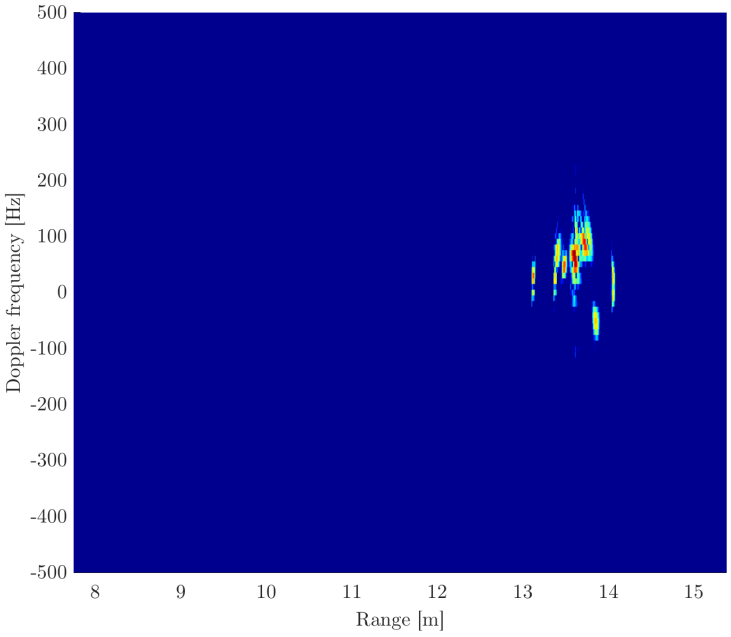

Figure 4.5: Range-Doppler matrix.

The Doppler frequency shift is plotted along the vertical axis, where the Doppler frequency of each bin is

$$f_d[k] = f_p \frac{k-1}{K} - \frac{1}{2} \quad k = 1, 2, 3, \cdots, K. \qquad \text{[Hz]} \tag{4.7}$$

and the range along the vertical axis has a scale corresponding to the fast-time sampling frequency f_s is

$$R[n] = r_{min} + \frac{c}{2}\left(t_s + \frac{n-1}{f_s} \right) \quad n = 1, 2, 3, \cdots, N. \qquad \text{[m]} \tag{4.8}$$

It can be seen that the target is decomposed into multiple point scatterer, and spread out along the vertical Doppler frequency axis. The two largest red clusters are from the torso and head of the target, while the smaller clusters are from the targets extremities, such as arms and legs. The target is moving towards the radar since the torso part of the scatterer have a positive Doppler frequency of around 100 Hz. A single scatter is observed underneath with a

negative Doppler frequency. This is from either a foot or an arm moving backward during the gait cycle, giving it a temporary negative radial velocity. The color represents the power at a certain range and Doppler frequency, where a more red color corresponds to more power.

4.3 Micro-Doppler Signature

The micro-Doppler signature $\boldsymbol{\mu}$ gives an integrated Doppler history of individual body segments during a given observation time. It is a spectral image that directly relate to the movement dynamics of the target [6, p. 191]. It is extracted from the range-Doppler matrix $\boldsymbol{G}$ by summing together only the samples that contains target point scatterer.

4.3.1 Range and Doppler frequency gating

Based on the target range and micro-Doppler bandwidth B_μ the range-Doppler matrix $\boldsymbol{G}$ is limited in range and Doppler frequencies to those cells containing a target, as illustrated in Figure 4.6.

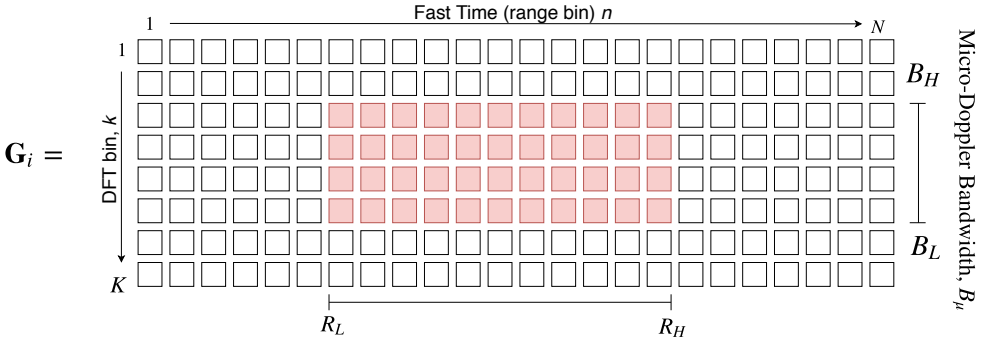

Figure 4.6: Range and Doppler frequency gating for the range-Doppler matrix $\boldsymbol{G}_i$.

R_H and R_L are a targets maximum and minimum range, and B_H and B_L are a targets maximum and minimum Doppler frequency shift in $\boldsymbol{G}_i$. The limits will vary for each $\boldsymbol{G}_i$ depending on the targets velocity and movement direction. The red samples are inside the range/Doppler gate and will contribute to the micro-Doppler signature. The white samples outside is ignored. The red cells show a range/Doppler gate for one target, but similarly, there would be a tracking gate for each target in the scenario.

The R_H, R_L,B_H and B_L needs to be obtained before computing $\boldsymbol{\mu}$. For simulated data, these values are obtained from the target simulator and provides a range/Doppler gate with very high accuracy. In a real system obtaining these values is the job of a tracker, often combined with a threshold detection algorithm to decompose a target into its scattering elements. This will not be a focus in this project.

Figure 4.7 shows a range-Doppler spectrum $\boldsymbol{G}_i$ with a tracking gate.

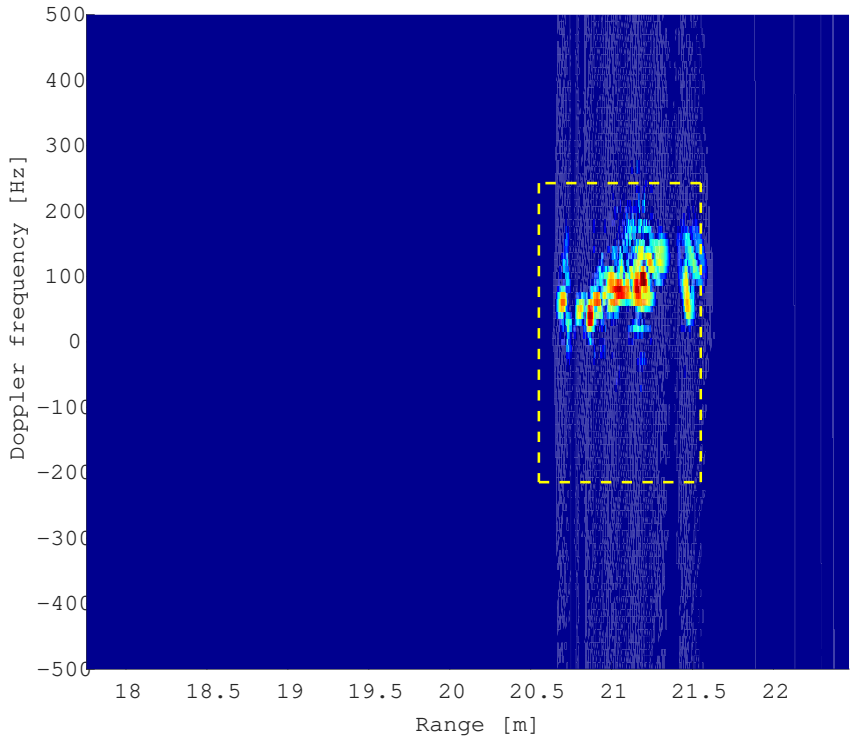

Figure 4.7: Range and Doppler frequency gate drawn on a range-Doppler spectrum $\boldsymbol{G}_i$.

The range limits R_H and R_L for scatter l in target χ from frame i is given as

$$R_H = R_{\chi,l,i} + \frac{R_t}{2} \tag{4.9}$$

and

$$R_L = R_{\chi,l,i} - \frac{R_t}{2} \tag{4.10}$$

where R_t is the target range span. For simplicity this is given as a constant based on the target type given in Table 4.1

Table 4.1: Target range span

Target	R_t
Human	$1\ m$
Dog	$1.5\ m$

B_H and B_L is the the maximum and minimum values from the Doppler frequency shift of each individual point scatter, shown in Figure 4.8.5

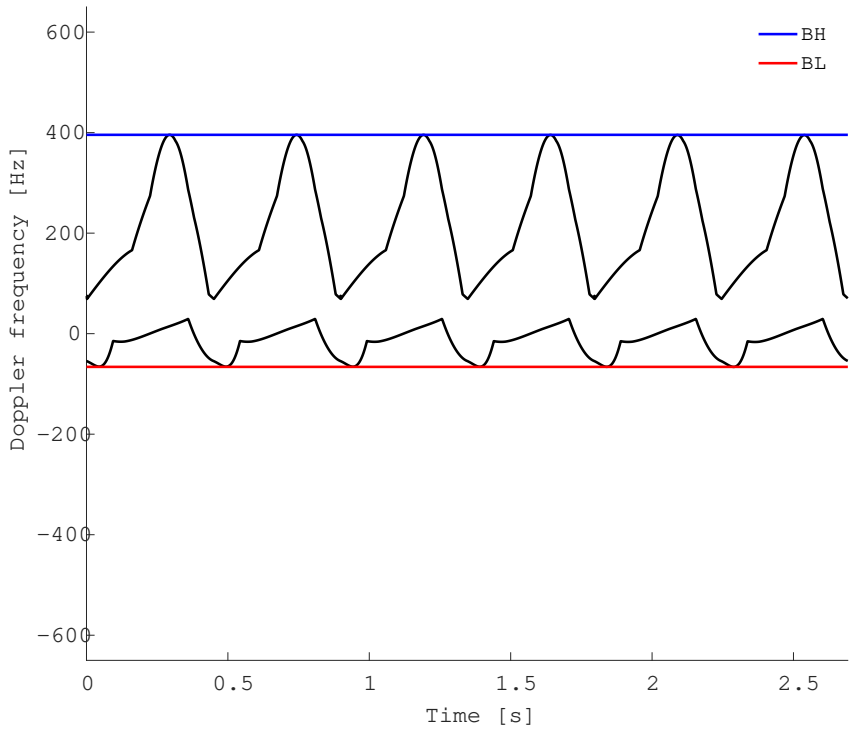

Figure 4.8: B_H and B_L is the max/min Doppler frequency shift of the targets point scatterer.

B_H and B_L are constant inside the same observation time T_o.

4.3.2 Micro-Doppler spectrum

$\boldsymbol{\mu}$ is obtained by row-wise summing the range bins within the range/frequency gate for each successive range-Doppler $\boldsymbol{G}_i$ matrix for $i = 1, 2, 3, \cdots, I$. The micro-Doppler signature matrix $\boldsymbol{\mu}$ is given by

$$\boldsymbol{\mu} = \begin{bmatrix} u_{1,1} & u_{1,2} & \dots & u_{1,I} \\ u_{2,1} & u_{2,2} & \dots & u_{2,I} \\ \vdots & \vdots & \ddots & \vdots \\ u_{K,1} & u_{K,2} & \dots & u_{K,I} \end{bmatrix} \tag{4.11}$$

where

$$u_{k,i} = \left\{ \begin{array}{ll} \sum_{n=R_L}^{n=R_H} g_{k,n,i} & \text{for } B_L < k < B_H \\ 0 & \text{elsewhere} \end{array} \right\} \tag{4.12}$$

for $i = 1, 2, 3, \cdots, I$. The added subscript i in $g_{k,n,i}$ indicates that this is the $g_{k,n}$ value associated with $\boldsymbol{G}_i$.

Each column in $\boldsymbol{\mu}$ is normalized to remove the propagation loss magnitude difference. Figure 4.9 shows the same $\boldsymbol{\mu}$ with and without normalization.

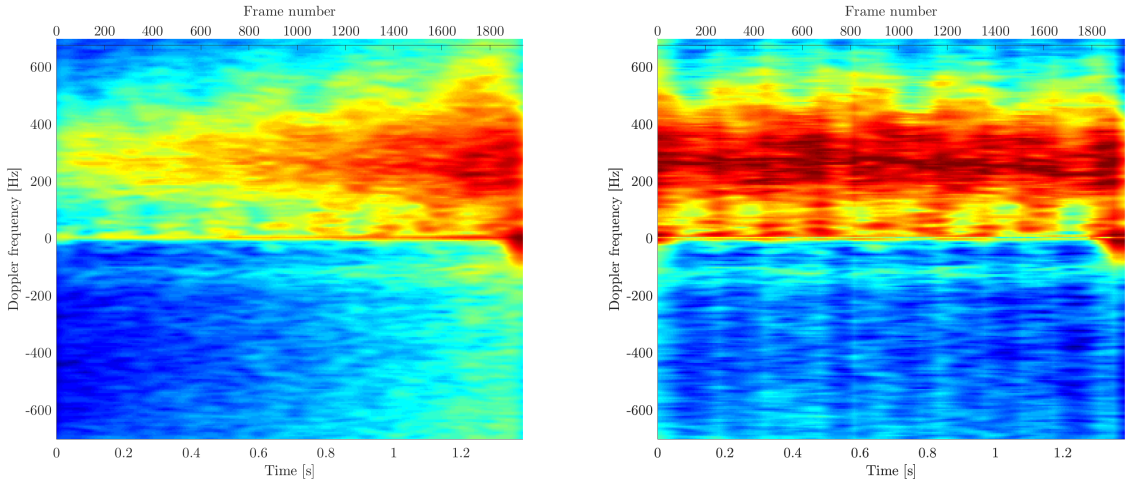

(a) Micro-Doppler signature

(b) Normalized Micro-Doppler signature

Figure 4.9: Normalization of each column in $\boldsymbol{\mu}$ to compensate for propagation loss.

It (a) the signal is much stronger on the right side than left. In (b) this difference is removed by normalization.

Figure 4.10 shows the micro-Doppler signature based on Figure 2.16. This scenario is created with the target movement model Λ from Chen, as explained in Section 2.6. In (a) the Doppler frequency shift directly from the point scatterer is illustrated and (b) shows the micro-Doppler signature matrix $\boldsymbol{\mu}$. The Figure in (a) is the true Doppler shifts of the target, and (b) should be as equal to (a) as possible.

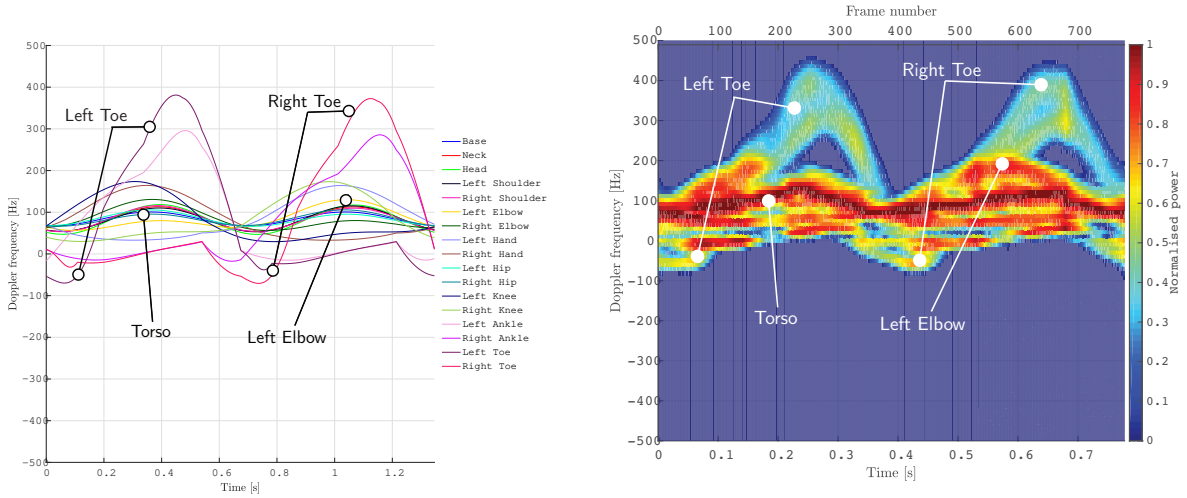

(a)

(b)

Figure 4.10: (a) The Doppler frequency shift for each point scatter. (b) The Micro-Doppler signature matrix $\boldsymbol{\mu}$ from the feature extractor. Simulation of a Human walking towards the radar with $\psi = 0°$.

From the true values in (a) the different part of the target is annotated in (b). The torso has the highest magnitude, and the least Doppler frequency shift. The top and bottom sawtooth shaped signals are from the legs. They have the highest velocity during a gait cycle, and hence the highest Doppler frequency shift f_d. Figure 4.11 shows the same signature as in Figure 4.10,

for a longer simulation, containing five gait cycles, or 10 steps. One step equals on peak in the micro-Doppler signature.

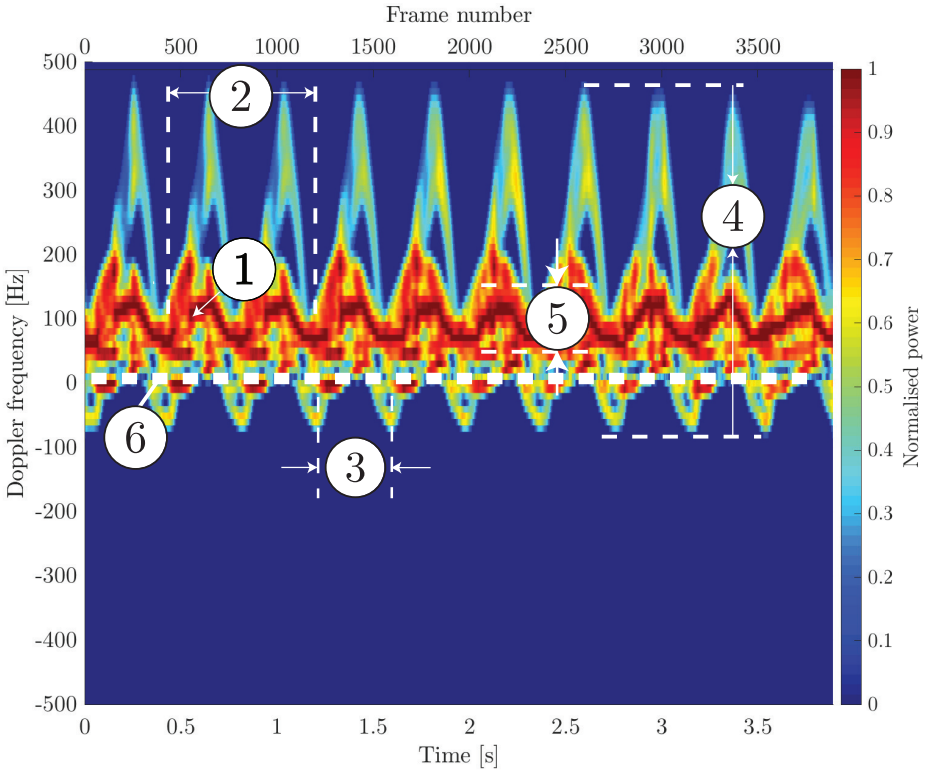

Figure 4.11: Micro-Doppler signature of a human waking toward the radar with $\psi = 0°$ performing 5 gait cycles.

The different target characteristics found in the micro-Doppler signature are labeled ① – ⑥ in Figure 4.11, and are defined as follows:

1. **Main Doppler Line**: This line, which contains the highest energy from the target, and is made up of the scatters with largest RCS. In most cases, this line is made up from the torso of the target. From the Human signature in Figure 4.11 it can be seen that the Main Doppler Line oscillates at twice the gait frequency.

2. **Gait Cycle** t_{stride}: The time between to alternating steps, making up a gait cycle. Each spike corresponds to one step, where sequential spikes are alternating feet.

3. **Step Period** t_{step}: The time between two peaks in the upper or lower envelopes. Each period in the signal corresponds to one step, making the period of the micro-Doppler signature t_{step}.

4. **Micro-Doppler bandwidth** B_μ: The micro-Doppler bandwidth for the target, here from the top peaks to the bottom peak, representing the entire Doppler variations of the target. This value represents the maximum velocity variations of each scatterer in the target.

5. **Main Doppler bandwidth**: The bandwidth of the Doppler signal without micro-Doppler modulation.

6. **Zero-Doppler Line**: A line of all the zero Doppler frequency bins. This is where the energy from stationary targets and clutter resides.

4.4 Step-Doppler

A method to measure the periodicity of the target's gait is to take Fourier transform of each column in the micro-Doppler signature matrix $\boldsymbol{\mu}$. Similar to any periodic signal, the more periods in the signal, the better frequency resolution is obtained from a Fourier analysis. At least one step period is needed to resolve the periodicity. However, a longer micro-Doppler signature will reduce the step frequency spectrum sidelobes, and make the step-frequency peaks more prominent. The step-Doppler matrix $\boldsymbol{D}$ is obtained by taking the DFT magnitude of each row in $\boldsymbol{\mu}$, and is given by

$$\mathbf{D} = \begin{bmatrix} d_{1,1} & d_{1,2} & \dots & d_{1,I} \\ d_{2,1} & d_{2,2} & \dots & d_{2,I} \\ \vdots & \vdots & \ddots & \vdots \\ d_{K,1} & d_{K,2} & \dots & d_{K,I} \end{bmatrix} \tag{4.13}$$

where d_{k,k_g} is given as

$$d_{k,k_g} = \left| \sum_{i=1}^{I} u_{k,i} \cdot \exp\left(-\frac{j2\pi k_g i}{I} \right) \right| \quad k_g = 1, 2, 3, \cdots, I \tag{4.14}$$

Figure 4.12 is extracted from the micro-Doppler signature in Figure 4.11.

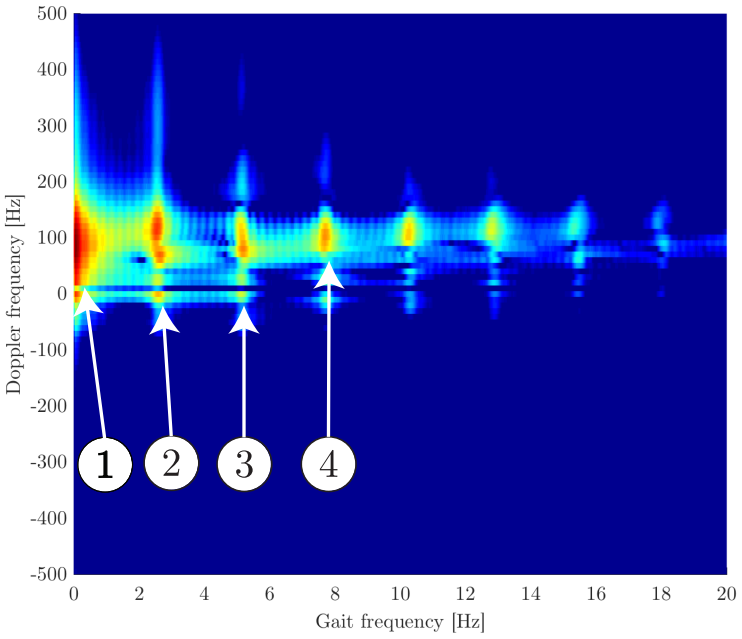

Figure 4.12: Step-Doppler matrix $\boldsymbol{D}$ showing step-frequency up to 20 Hz.

It can be seen that the target is moving towards the radar, given the average Doppler frequency around $+100$ Hz. This equals $v_m \approx 2$ m/s, by using Equation 2.4. The frequency range in $\boldsymbol{D}$

far exceeds what is necessary to record both the fundamental step frequency and the first couple of harmonics. Therefor the step frequency is limited to 20 Hz. The annotated numbers ①-④ are given as follows:

1. **Low step frequency component** f_0: This frequency bin(s) are mainly from the main Doppler line, which consists of scatterer with little oscillations, like the torso.
2. **Fundamental step frequency** f_m: This is the step frequency of the target. The frequencies are made up from the oscillating appendages of the target.
3. **Second step frequency harmonic** f_2
4. **Third step frequency harmonic** f_3

The low step frequency component f_0 has a much higher magnitude than f_m, f_2 and f_3. To reliably detect their peaks a second step-Doppler matrix is given as $\boldsymbol{D_0}$, which is obtained by using Equation 4.14 on $\boldsymbol{\mu_0}$. Each element in $\boldsymbol{D_0}$ is similarly denoted as $d0_{k,k_g}$. $\boldsymbol{\mu_0}$ is the micro-Doppler signature matrix with the low step-frequency components f_0 removed, and is given as

$$\boldsymbol{\mu_0} = \begin{bmatrix} u0_{1,1} & u0_{1,2} & \dots & u0_{1,I} \\ u0_{2,1} & u0_{2,2} & \dots & u0_{2,I} \\ \vdots & \vdots & \ddots & \vdots \\ u0_{K,1} & u0_{K,2} & \dots & u0_{K,I} \end{bmatrix} \tag{4.15}$$

where

$$u0_{i,k} = \frac{1}{I}\sum_{i=1}^{I} u_{i,k} \quad k = 1, 2, 3 \cdots, K \tag{4.16}$$

To extract f_m, f_2 and f_3, each column in $\boldsymbol{D_0}$ are summed together to form the *step-Doppler spectrogram* D_g, given as

$$D_g[k_g] = \sum_{k=1}^{K} d0_{k,k_g} \quad k_g = 1, 2, 3, \cdots, I \tag{4.17}$$

and is plotted in Figure 4.13.

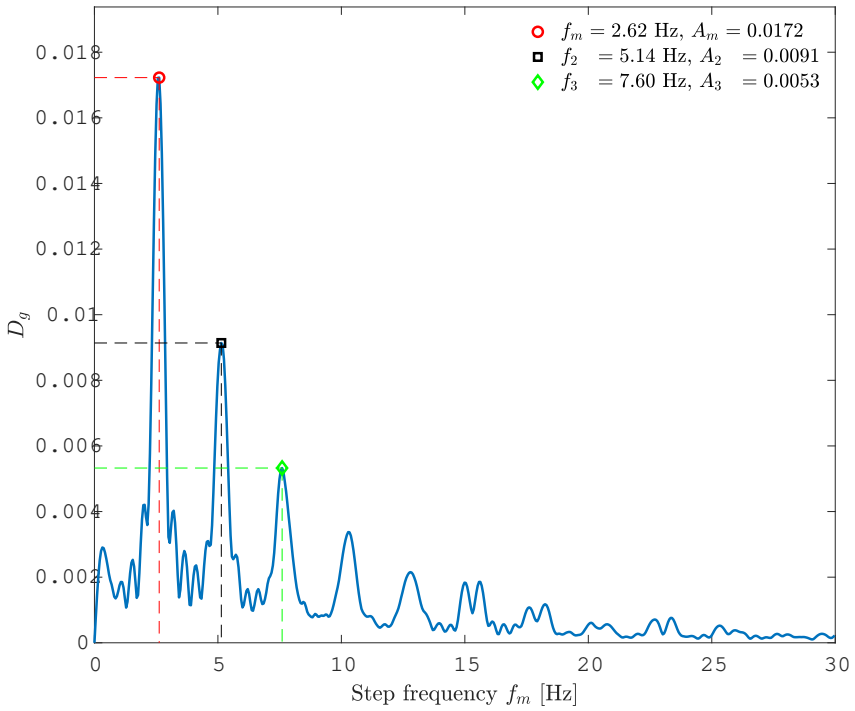

Figure 4.13: step-Doppler spectrogram D_g with f_m, f_2 and f_3 annotated.

The step frequency peaks in D_g are detected and their amplitude and frequency extracted. f_m is obtained by detecting the highest peak in D_g. The highest peak will be the low step frequency component, f_0 visible on the left side in Figure 4.13. The f_2 and f_3 peaks are estimated as the highest peaks close to where 2nd and 3rd harmonic frequency is expected.

4.5 Feature Set

A feature-Set F containing six parameters which compactly describes the target, is extracted from $\boldsymbol{D}$ and $\boldsymbol{D_0}$. The feature-Set parameter extraction are based on work from [23], [16] and [4]. In [23] f_m are detected, from the peaks in the step-Doppler spectrogram D_g. In [16] a solution to discriminate between human and animals using their step frequency f_m and the RCS differences between the main body (torso) and the oscillating parts (appendages) of each target is proposed. In [4] a system combining these feature parameters is demonstrated, and provided a classification accuracy of 96%. The Feature-Set parameters are given as follows:

- **Target radial velocity** v_m: This value can be obtained from the estimated Doppler frequency, f_d given as

$$v_m = \frac{f_d \lambda}{2} \tag{4.18}$$

by using Equation 2.4. f_d is obtained from the Doppler frequencies at which the peak energy from the torso occurs, which can be found in the first column in $\boldsymbol{D}$, given as

$$D_1 = \begin{bmatrix} d_{1,1} \\ d_{2,1} \\ \vdots \\ d_{K,1} \end{bmatrix} \tag{4.19}$$

D_1 is shown in Figure 4.14, based on $\boldsymbol{D}$ from Figure 4.12

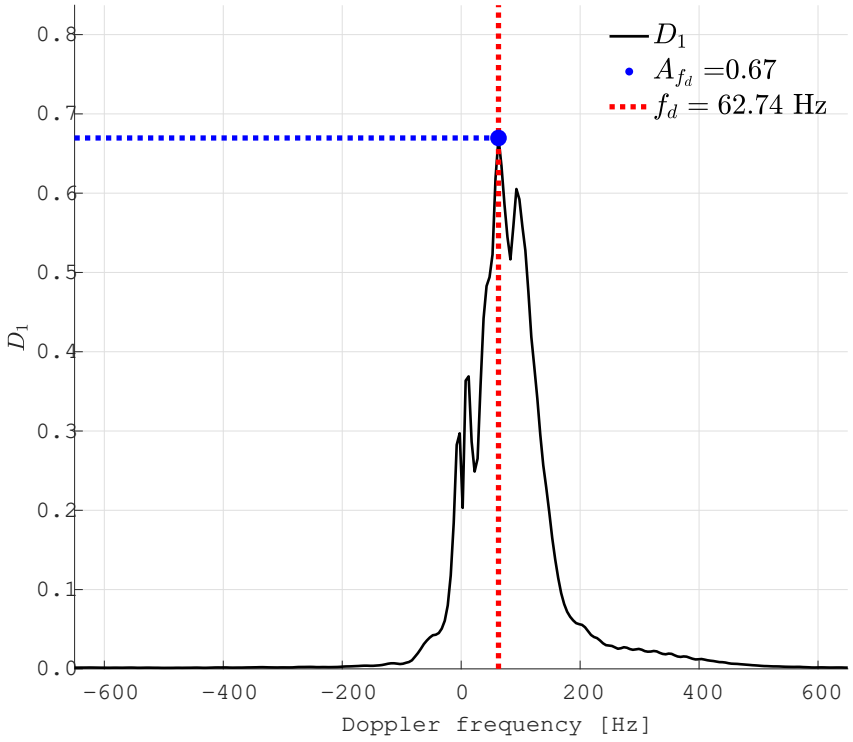

Figure 4.14: Doppler frequency of the first column in $\boldsymbol{D}$

The Doppler frequency f_d is the frequency of the highest peak A_{f_d} which is given as

$$A_{f_d} = max(D_1). \tag{4.20}$$

f_d is the Doppler frequency at which A_{f_d} is located.

- **Micro-Doppler bandwidth** B_μ: The micro-Doppler bandwidth B_μ is extracted from D_1 as shown in Figure 4.15.

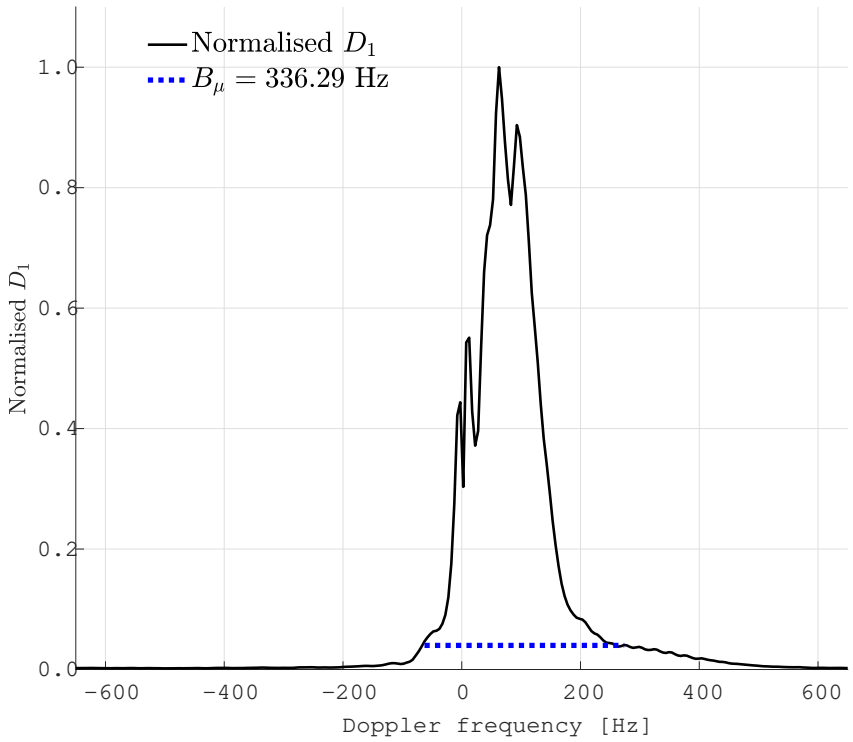

Figure 4.15: $\boldsymbol{D}$

It is determined by locating when the rising and falling edges of the signal is above a certain threshold B_μ. The values in D_1 are normalized to make the threshold equal for all targets. A threshold of $t_\mu = 0.04$ was found to give the most accurate micro-Doppler bandwidth.

- **Step Length** L_m: The step length, repeated here from Equation 2.6 can be found as

$$L_m = \frac{v_m}{f_m} \quad [\text{m}] \tag{4.21}$$

- **Step-harmonic frequency ratios** β_1 and β_2: This is an indication of the span in which the step frequencies lie and is given by

$$\beta_1 = \frac{f_2}{f_m} \quad \beta_2 = \frac{f_3}{f_m} \tag{4.22}$$

They have no physical interpretable meaning, but can be used to ensure the correct peaks are detected. If the correct peaks are detected, then $\beta_1 = 2$ and $\beta_2 = 3$, since harmonic frequencies is always a integer multiple of the fundamental frequency.

- **Step amplitude ratio** ρ: This value represents the ratio between the total micro-Doppler energy to the constant Doppler energy that is located with the low step frequency components in $\boldsymbol{D}$, as annotated in 4.12. The micro-Doppler energy is spread between the A_m, A_{f_2} and A_{f_3} peaks, representing the energy from the moving appendages, such as arm and feet. The gait amplitude ratio p is given as

$$\rho = \frac{A_m + A_2 + A_3}{A_{f_d}} \tag{4.23}$$

where the constant Doppler energy A_{f_d} is the amplitude of D_1, when it is not normalized, as shown in Figure 4.14. ρ is expected to assist in discriminating humans against pet-animal targets, as humans is expected to have a higher RCS-ratio compared to dogs.

From these six parameters the feature-Set F is defined as

$$F = \begin{bmatrix} v_m \\ B_\mu \\ L_m \\ \beta_1 \\ \beta_2 \\ \rho \end{bmatrix} \tag{4.24}$$

Chapter 5

Results and Discussion

An evaluation and demonstration of the simulator and feature extractor are given in this chapter. Highlighting the benefits and challenges with motion capture recordings, the time-frequency trade-off in $\boldsymbol{G}$ and and evaluation of the Feature-Set parameters.

An evaluation of multiple human and the single dog dataset is presented. A total of 170 scenarios are simulated, consisting of:

- 148 human mo-cap recordings
- 1 dog mo-cap recording
- 21 Chen target model simulations

All scenarios are limited to constant velocity motion, directly towards $\psi = 0°$ or away $\psi = 180°$ from the radar LOS. These are the best conditions for detecting a targets Doppler frequency shift. The human targets have a target height $H = 1.8$ m and $\sigma = 1\ m^2$ and the dog $H = 0.2$ m and $\sigma = 0.2\ m^2$. To highlight the benefits and disadvantages of using mo-cap target movement files, they will be compared to the Chen target moment files based on the human simulation explained in Section 2.6.

5.1 Radar Simulator Parameters

In 2017 Novelda AS released a new ultra-wideband (UWB) pulse-Doppler radar, called the $X4$ [9]. It is hypothesized that this has good enough range and Doppler resolution to be used for ATR. It is a low power radar with up to 25 m range, intended for indoor use. Its low power makes it safe to use on humans and animals. The results presented are obtained with the radar simulator configured to operate like the $X4$, which has the following parameters.

Table 5.1: Radar parameters P

Symbol	Parameter	Value
f_c	Carrier frequency	7.29 GHz
f_s	Receiver sampling frequency	23.328 GS/s
f_p	Pulse repetition frequency (PRF)	$300 - 1300$ Hz
G_{rx}	Receiver amplifier gain	10 dB
G_t	Transmit antenna gain	4 dBi
G_r	Receive antenna gain	4 dBi
τ	Pulse duration	1ns
P_t	Peak transmit power	0 dBm
θ	Transmit pulse phase	0

The $X4$ has a maximum $f_p = 300$ Hz, which limits $v_r = 6$ m/s, due to aliasing. This is found to be to low for most of the mo-cap recordings used in this project. Hence f_p is adjusted individually for each scenario, and set to the lowest value that still prevents aliasing.

5.2 Target models from motion capture recordings

Using motion capture recordings of humans provided accurate movement patterns, when comparing with the human walking model from Chen [6] introduced in Section 2.6. Figure 5.1 shows the range R of each scatterer for a walking Human target from a mo-cap recording in (a) and from the Chen target model in (b).

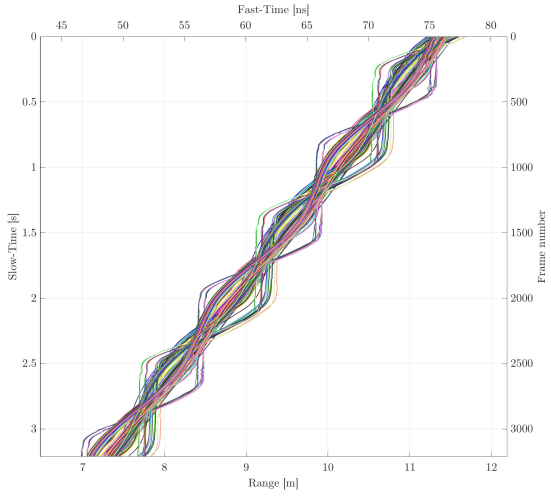

(a) Scatterer range from a walking Human from a mo-cap recording.

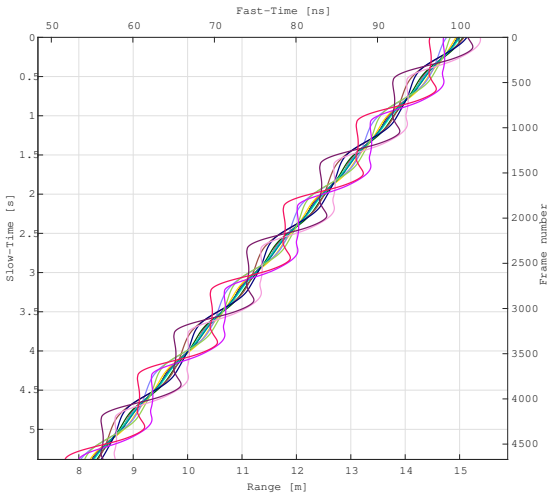

(b) Range for each scatterer from a walking Human from Chen target model.

Figure 5.1: Comparison between a mo-cap recording and the Chen target model.

Both (a) and (b) looks very similar, with the same oscillating pattern of the arms and feet found in both. Most mo-cap recordings provided between $30 - 70$ markers on each target compared to 17 in (b). This creates a more dense target path, which again resulted in a diffused micro-

Doppler signature as can be seen by comparing Figure 4.11 (Chen) and 5.3. In (a) it is more difficult to separate the movement of each arm, foot and torso, compared to Chen model.

It proved easy to find free and available motion capture recording databases for human targets. In [11] there are 144 different subjects performing a large number of different movement pattern, with around 100 unique recordings of walking and running. However for a dog, and pet-animal targets it proved difficult to obtain mo-cap recordings. A few dog recordings where found in [20], but of those only one recording of a galloping dog was usable. In it the a dog is galloping 2 gait cycles in a straight line as shown in Figure 5.2.

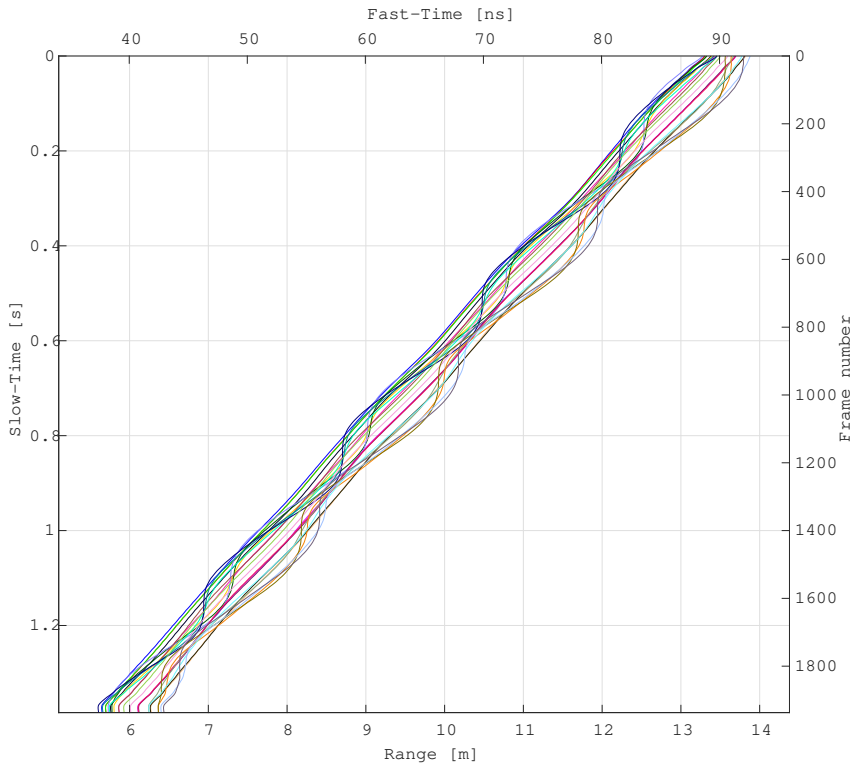

Figure 5.2: Range line for a mo-cap recording of a galloping Dog, $\psi = 0$.

As discussed in Section 2.6.1 the recording shows a movement pattern which has the expected features of a dog, based on the quadrupedal gait analysis. Without sufficient dog recordings it was not possible to generate a large and varied dataset for human/dog classification. Either more dog recordings needs to be obtained, or a specific dog simulator can be created.

5.3 Evaluation of the Feature Extractor

Feature extraction results for humans and dog is presented. Four human scenarios are compared, two from mo-cap recording and two from the Chen target model, each with one slow and one running fast target. The feature-Sets are extracted with the feature extractor parameters given in Table 5.2.

Table 5.2: Feature Extraction parameters

Symbol	Parameter	Value
T_d	Coherent Processing Interval	0.1s
σ_w	Gaussian window steepness	0.4
t_μ	micro-Doppler bandwidth threshold	0.04

5.3.1 Human targets

Figure 5.3 shows the the micro-Doppler signature of a human walking towards the radar at different radial velocities with $\psi = 0°$.

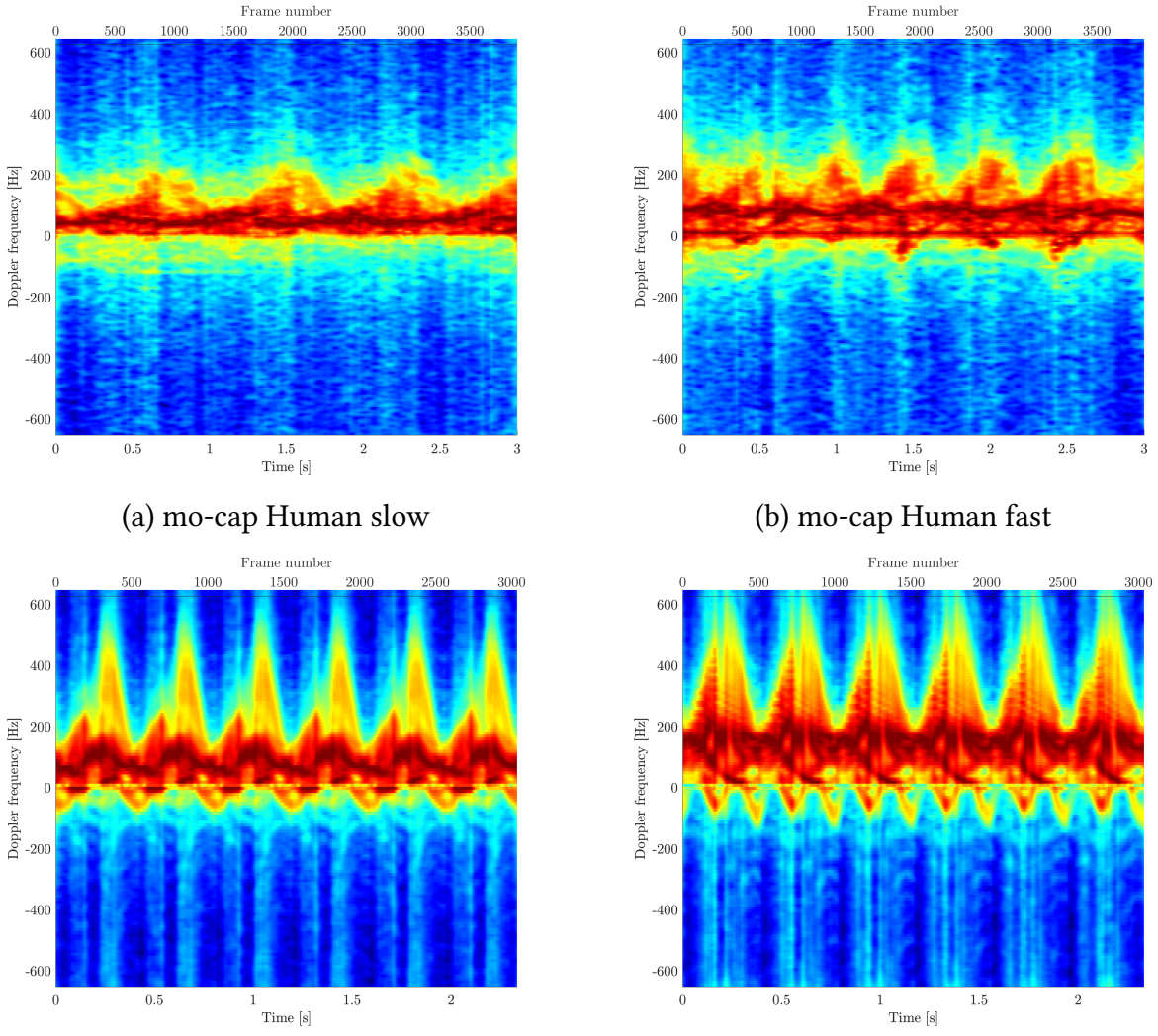

(a) mo-cap Human slow

(b) mo-cap Human fast

(c) Chen Human slow

(d) Chen Human fast

Figure 5.3: micro-Doppler signatures for an approaching human with $\psi = 0°$.

Figure (a) and (b) are created from a mo-cap recording, while (c) and (d) are created from the Chen human model. It can be observed that the faster targets in (b) and (d) have a main-Doppler line at a higher Doppler frequency. The total observation time $T_o = T \cdot I$ for each $\boldsymbol{\mu}$

is along the vertical axis. This directly represents the time the targets has been recorded by the radar. A more step periods results in D_g with more prominent peaks, which is shown in Figure 5.4.

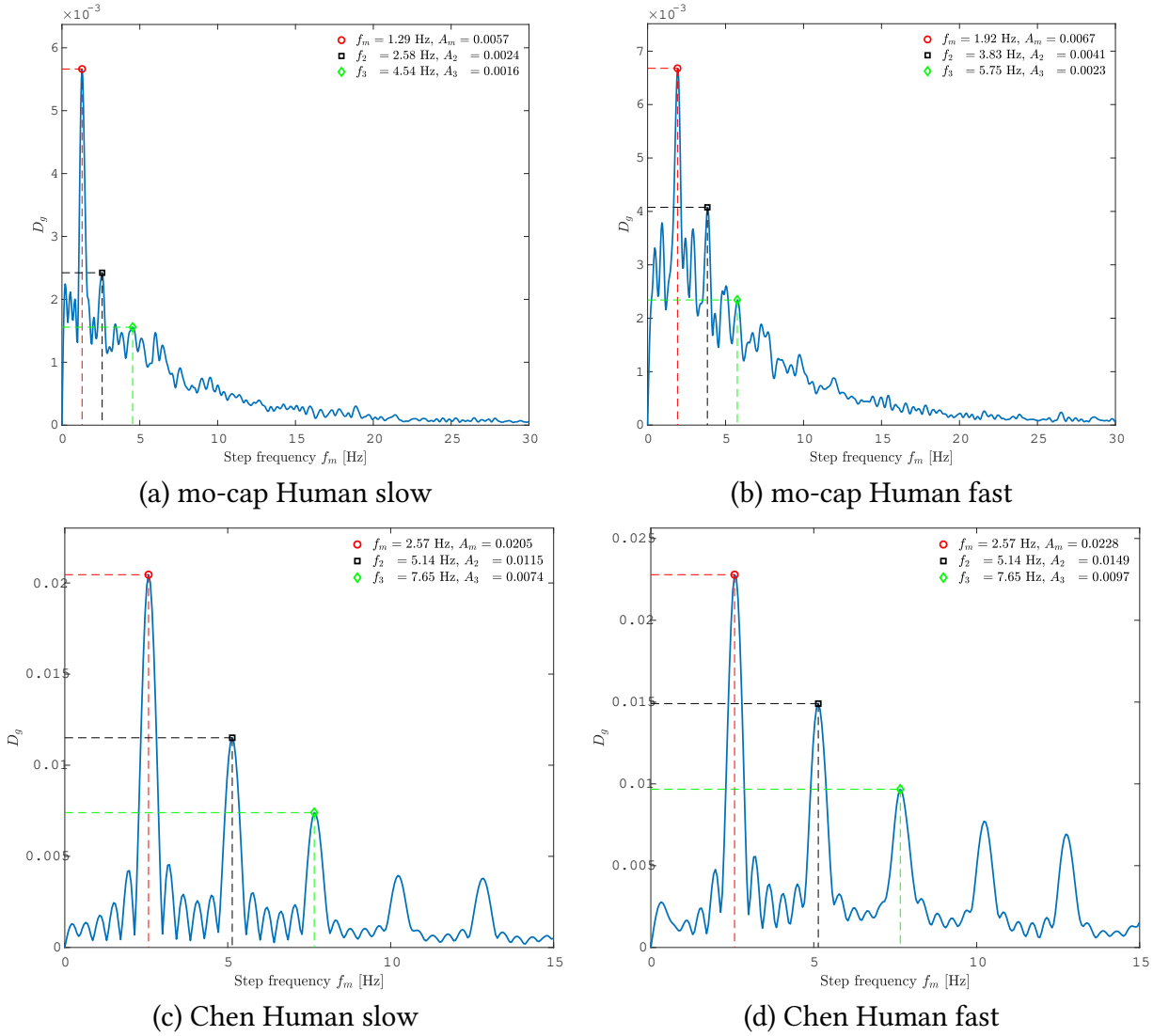

(a) mo-cap Human slow

(b) mo-cap Human fast

(c) Chen Human slow

(d) Chen Human fast

Figure 5.4: Step frequency extraction by peak detection.

It can be seen that the Chen target models have lower sidelobe levels, compared to mo-cap. This is a result of more gait cycles within the observation time. Lower sidelobe levels makes it easier for the peak detection to correctly estimate f_m, f_2, f_3, A_m, A_2 and A_3. In (a) the second and third harmonic are just above the sidelobes, while in (b) they are more or less hidden. This shows that the observation time of the target, T_o is a critical factor in resolving the step-frequencies. f_m is equal in (c) and (d), because the Chen target simulation maintains a constant step frequency, independent of v_m. This is a limitation in the Chen model, where it does not follow accurately the motion of a real target.

A longer recording in time, assuming more periods, will reduce the sidelobes in D_g and make the peak detection more accurate. Short observation time proved to be a major limitation for the the mo-cap recordings.

Figure 5.5 shows the estimated Doppler frequency f_d and its amplitude A_{f_d}.

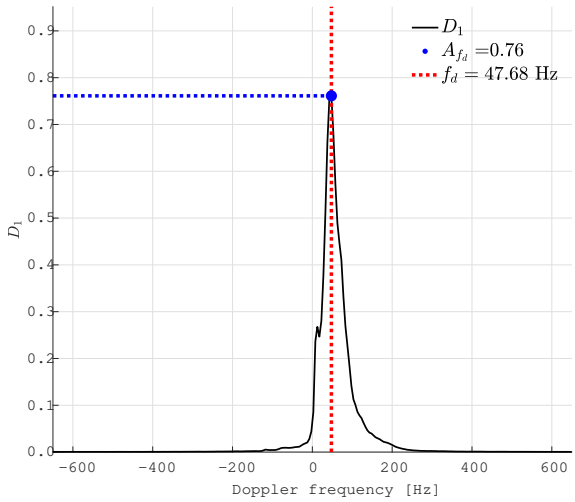

(a) mo-cap Human slow

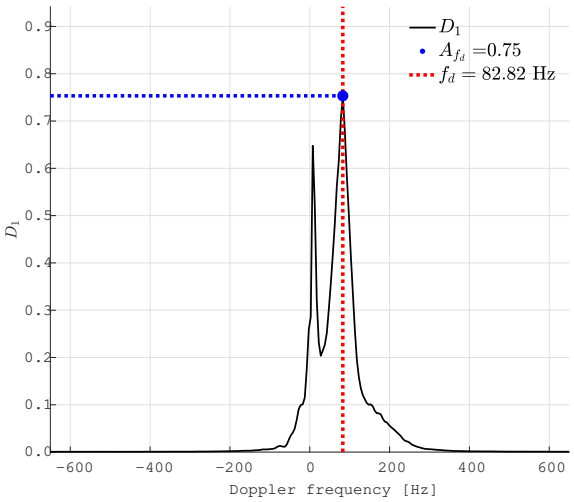

(b) mo-cap Human fast

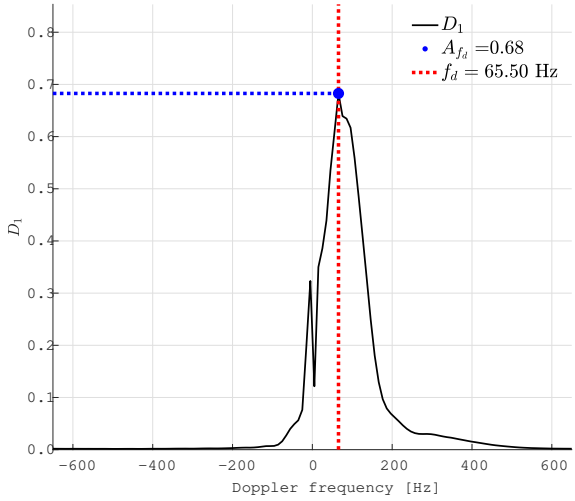

(c) Chen Human slow

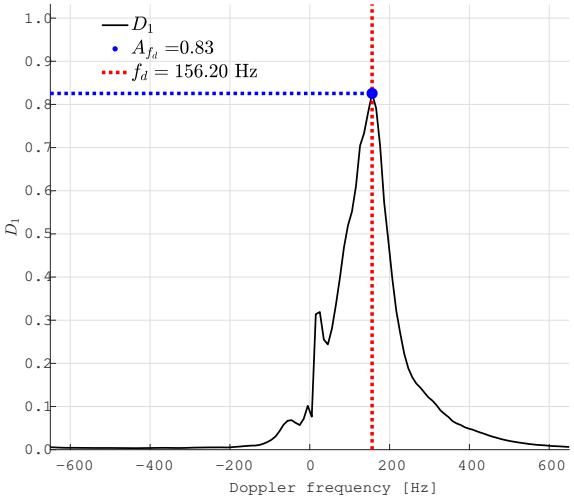

(d) Chen Human fast

Figure 5.5: Average Doppler frequency and micro-Doppler bandwidth

It can be observed that the two slow targets (a) and (c) have a lower f_d than the faster targets in (b) and (d). The value of A_{f_d} are very close for the four targets. Since all targets are human and have equal RCS σ, this is expected.

Figure 5.6 shows the micro-Doppler bandwidth B_μ for the four targets.

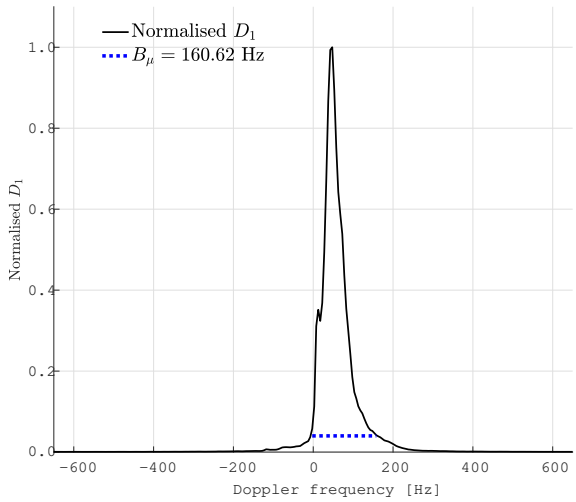

(a) mo-cap Human slow

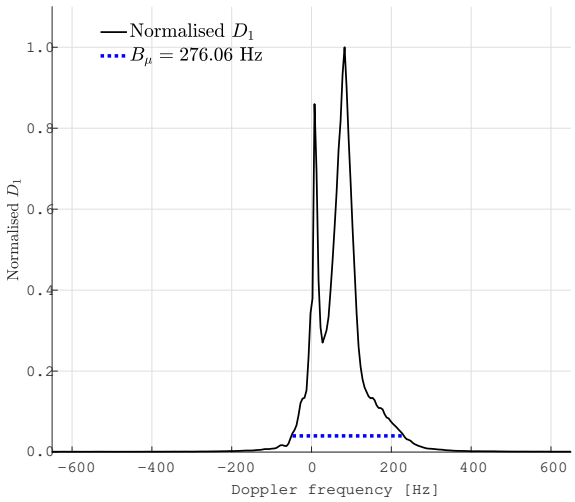

(b) mo-cap Human fast

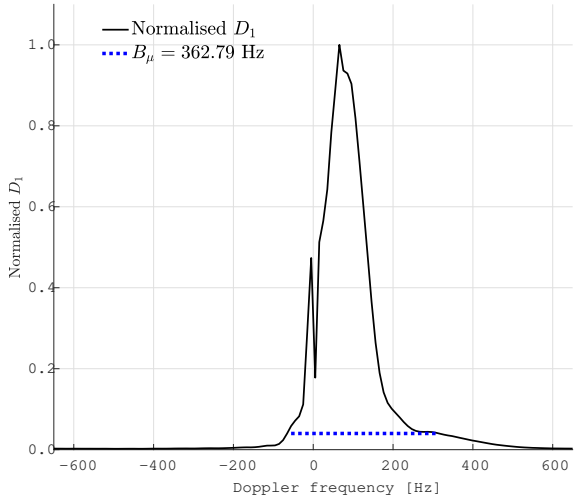

(c) Chen Human slow

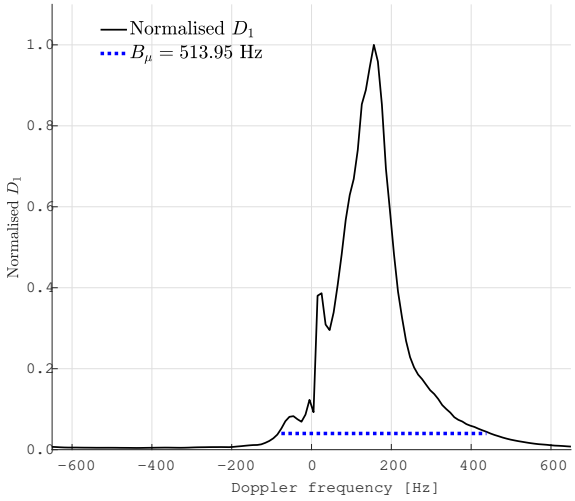

(d) Chen Human fast

Figure 5.6: micro-Doppler bandwidth estimation

The micro-Doppler bandwidth B_μ can be seen to increase with a targets radial velocity. This is an indication of faster moving appendages, which is a result of increased f_m. D_1 is normalized such that the micro-Doppler bandwidth estimation threshold t_μ is applicable for all targets.

5.3.2 Dog

Figure 5.7 shows the feature extraction results from the dog mo-cap recording. In (a) the Doppler frequency shift for each point scatterer is given, in (b) the micro-Doppler signature matrix $\boldsymbol{\mu}$, in (c) the step-frequency matrix $\boldsymbol{D}$, in (d) the normalized D_1 and in (e) D_1.

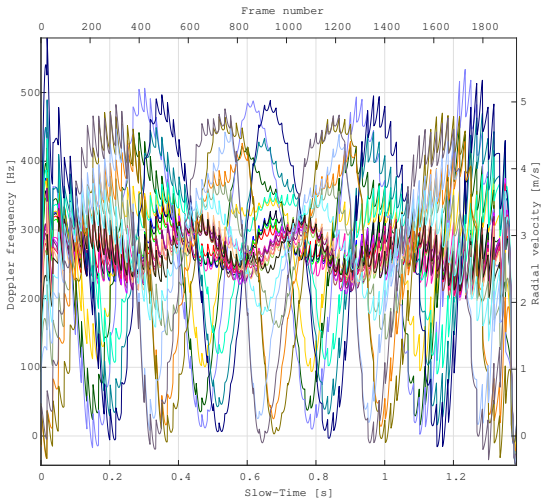

(a) Dog Doppler shift

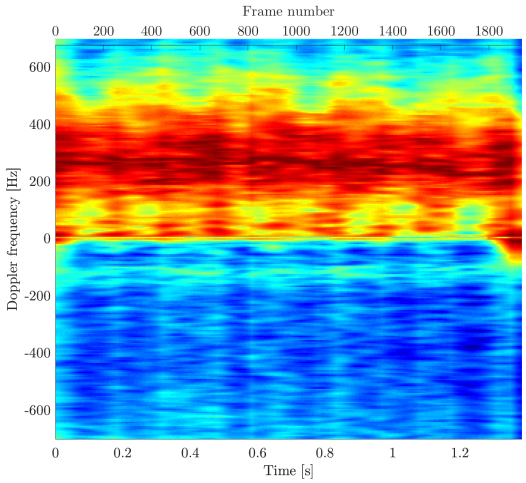

(b) Micro-Doppler signature

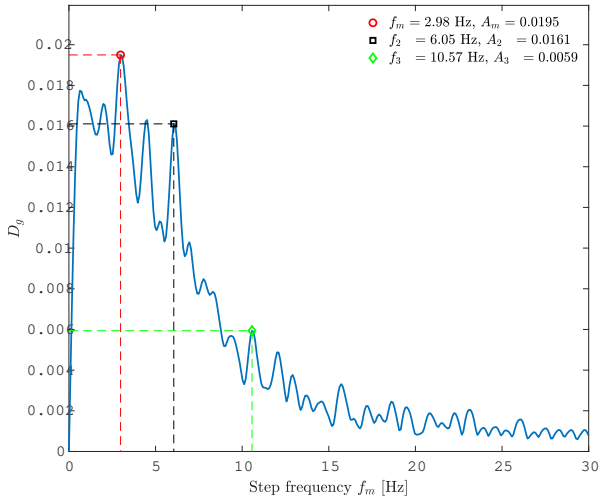

(c) Step frequency peaks

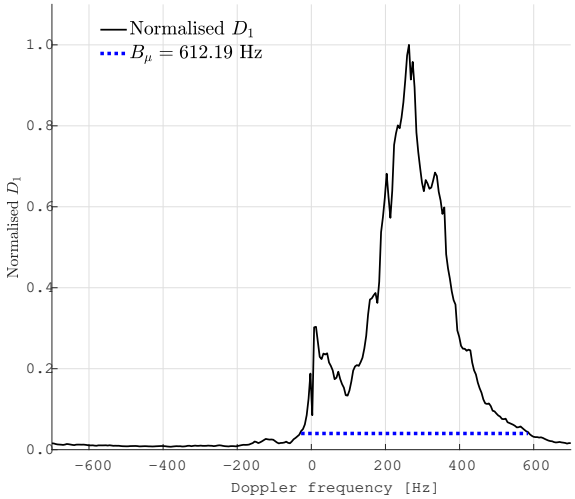

(d) Normalized D_1

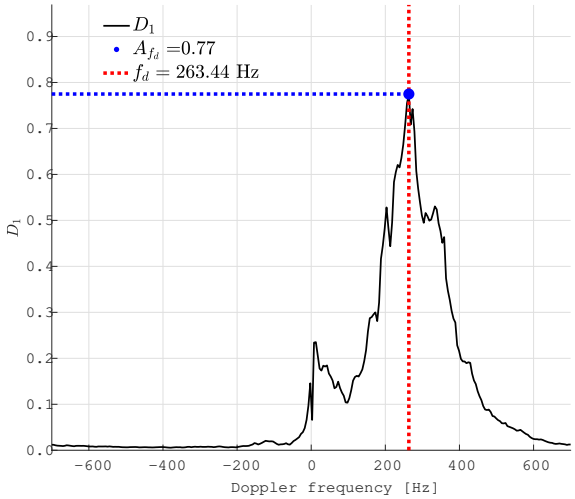

(e) D_1

Figure 5.7: Average Doppler frequency and micro-Doppler bandwidth

A step-frequency $f_m \approx 6$ Hz is extracted from (a). Since a dog has four legs, which are much shorted than a human, it is expected to have a higher f_m relative to v_m. In (c) f_m is

erroneous estimated to be 2.98 Hz, when is should be 6.05 Hz as is estimated for f_2. This error happens since the micro-Doppler envelope of each pair of legs is not separated in $\boldsymbol{\mu}$. In (b) the same six envelopes can barely be counted as the red columns below the main-Doppler line. The legs of the dogs are not clearly separable. A longer observation time is assumed to reduce the sidelobe levels in D_g, enough to estimate correct step frequencies. However due to the lack of dog mo-cap recordings this has not been tested. From (d) $B_\mu = 607$ Hz, and from (e) $A_m = 0.79$ and $f_d = 263$ Hz.

5.4 Feature-Set Results

Figure 5.8 shows how the step length L_m varies according to v_m, for all the human mo-cap and dog recordings.

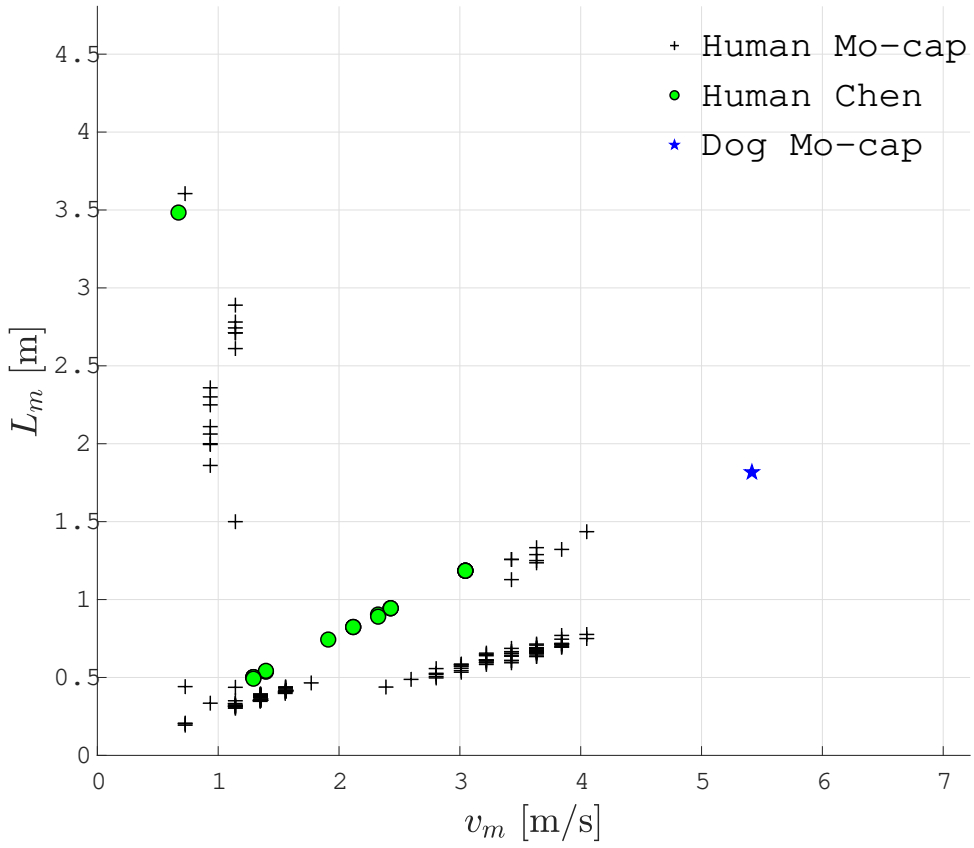

Figure 5.8: Step length L_m versus v_m

A linear relationship between L_s and v_m for the major part of the targets can be observed. The targets with $L_m > 1.5$ m is wrong estimates, caused by erroneous peak estimation for f_m. When comparing humans and the dog it can be seen that the dog has much shorter L_m relative to its v_m. This is assumed to be a critical feature parameter to differentiate human and dog targets.

Figure 5.9 shows each of the six feature-Set parameters for all 170 scenarios.

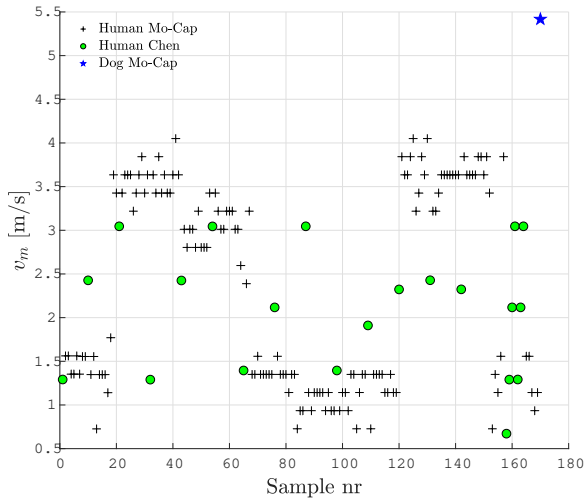

(a) v_m

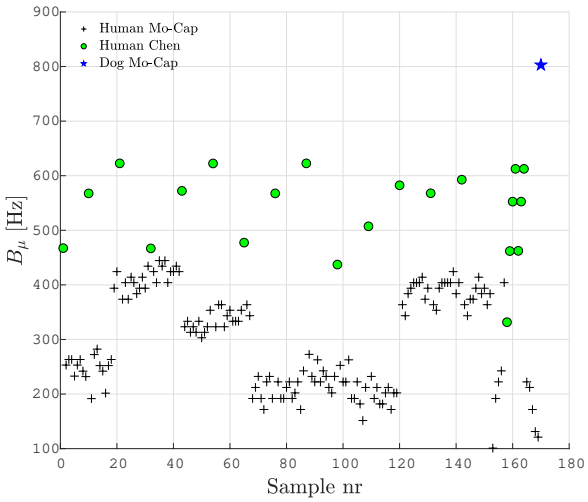

(b) B_μ

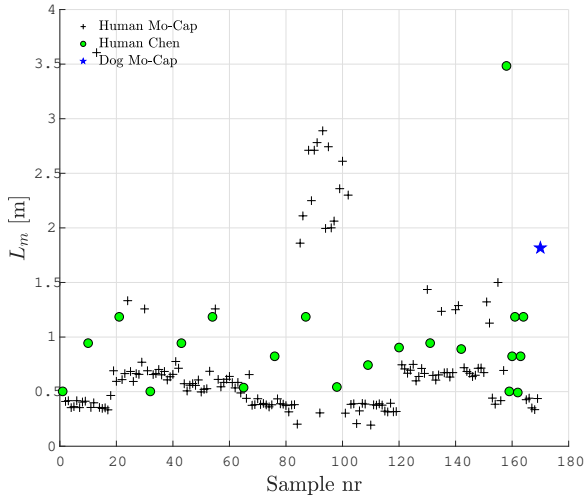

(c) L_m

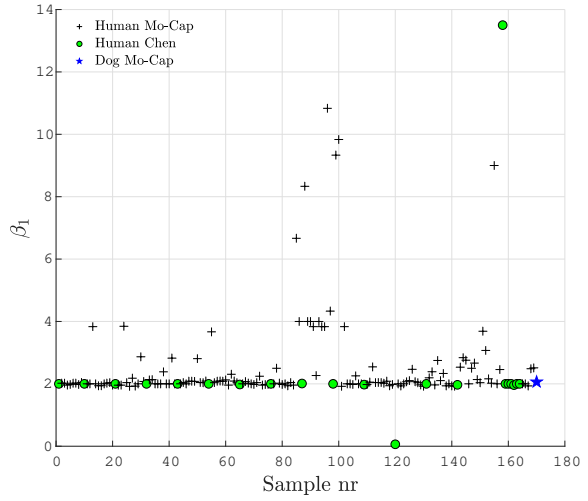

(d) β_1

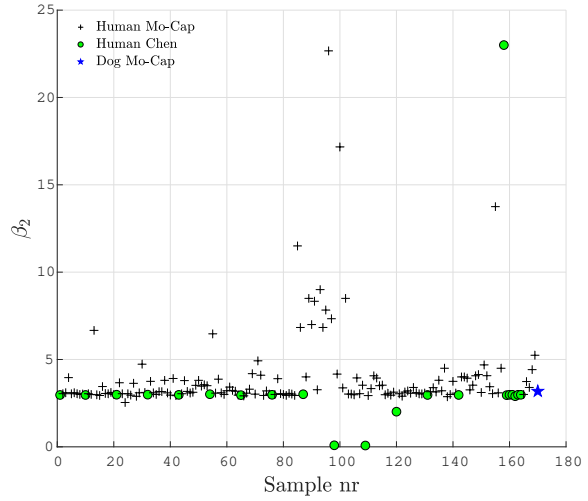

(e) β_2

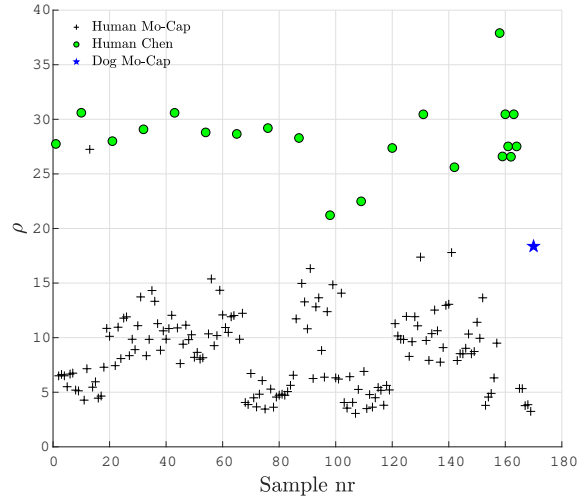

(e) ρ

Figure 5.9: Feature-Set results

Each targets v_m is shown in (a). v_m can be any value for any target, and on its own does not provide any mean to differentiate human and dog targets. v_m is first valuable when used

together with f_m. The micro-Doppler signature bandwidth B_μ shown in (b) separates the targets into groups. The human Chen data, due to its larger envelopes, have consistently hight B_μ. It is expected that the groupings in (b) correspond to the groups in (a). β_1 and β_2, if extracted with perfect accuracy should be 2 and 3 respectively. The deviation from these value makes β_1 and β_2 valuable as a estimator for the correctness of f_m, f_2 and f_3. In (d) and (e) it can be observed that most values fall on 2 and 3, respectively, with some error values far off. The step amplitude ratio ρ is observed to group similar targets, and is expected to help discriminate between human and non-human targets. It is expected that ρ is higher for humans than pet-animals. With only one dog target its value is not significant and a proper evaluation of ρ is not possible. It can be seen that the targets based on Chen simulation has a higher ρ, since their micro-Doppler signature has higher envelopes.

The accuracy of each of the feature-Set parameters is not that important for classification. The importance of the feature extraction is to obtain parameters which group target of equal class together.

5.5 Limitations in the micro-Doppler signature

The feature extraction results presented are from "best-case" scenarios, as mentioned at the start of this chapter. In real recordings the scenario conditions will vary, and compared to the results presented here, most likely be worse. An aspect angle ψ around $90°$ would significantly decrease radars ability to detect the targets Doppler frequency shift. Two similar target signatures, with one with $\psi = 0°$ and one with $\psi = 90°$ is show in Figure 5.10.

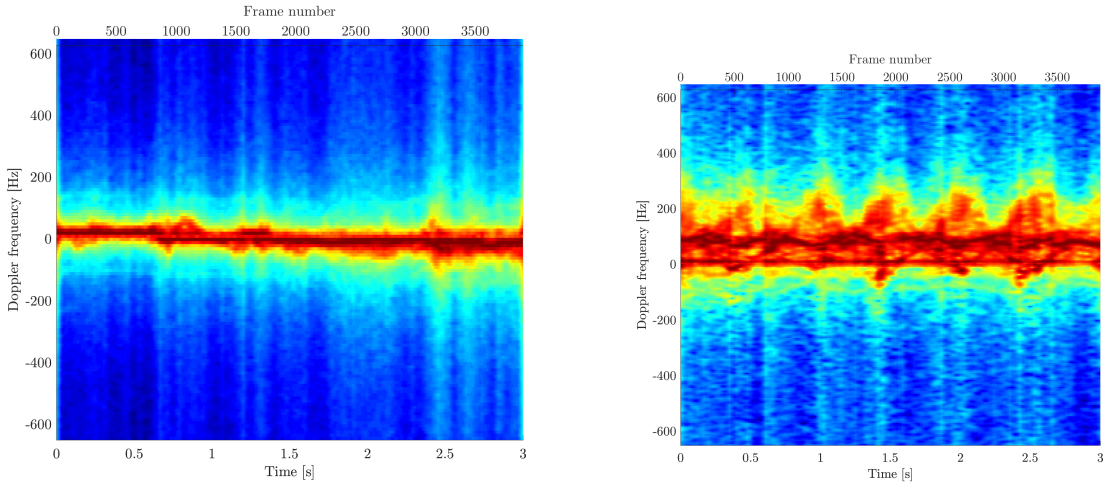

(a) $\psi = 0°$ (b) $\psi \approx 90°$

Figure 5.10: Comparison between a mo-cap recording and the Chen target model.

The micro-Doppler signature envelopes is significantly less in (a) than (b), and the Doppler frequency of the main Doppler line is $f_d \approx 0$. This shows how important an aspect angle ψ close to $0°$ or $180°$ when observing the target.

To extract the micro-Doppler signature is also required isolate target path with constant velocity and direction in $\boldsymbol{\mu}$. Figure 5.11 show a problematic scenario where two different movement directions are observed, and present in the same $\boldsymbol{\mu}$.

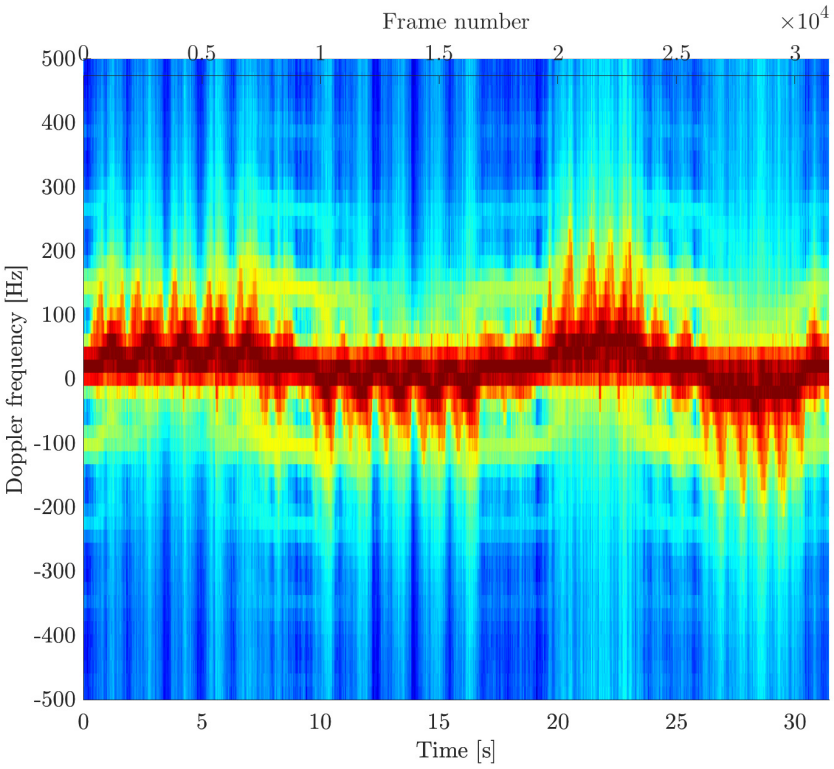

Figure 5.11: A micro-Doppler signature of a human walking in multiple directions.

The directional change cause the main-Doppler line to change sign, and makes it near impossible to reliable extract the step-frequency components. A solution here would be to divided $\boldsymbol{\mu}$ into four shorter observation periods, and perform feature extraction of each separately. However if the observation time becomes to short, the step-frequency components cannot be resolved.

Chapter 6

Conclusion

A system for generating annotated datasets of humans and dogs, based on micro-Doppler signature from radar is developed. It uses motion capture recordings to obtain human and dog movement patterns. A radar simulator has been developed which simulates the operation of a pulse-Doppler radar. A feature extraction method is proposed. This is intended to extract six feature parameters to compactly describe the target. It is assumed that this feature set clusters similar targets classes, such that a classifier can with good accuracy determine the target class.

With this system 170 annotated feature sets is created, and to some degree clustered each target class. However only one usable dog motion capture recordings was obtained. This prevented a through evaluation of how well the feature extractor grouped human and dog targets. To train a classifier to automatically detect human and dog targets, more dog motion recordings needs to be obtained or created.

6.1 Further work

Target tracking

To use this system on real radar recordings, a tracking module needs to be developed. It should performed a threshold detection on $\boldsymbol{G}$, and then lock the clustering magnitudes for each target in a range/Doppler gate. It is also critical that the thresholding resolves the signature in $\boldsymbol{G}$ into multiple separated clusters, such as legs, torso and arms, as explained in Section 4.2.2. Without the micro-Doppler signature wont get the characteristic envelopes caused by the legs, and the step-frequency will be hard to extract.

Bibliography

[1] T. Ø. Fossum, "Exploration of micro-doppler signatures associated with humans and dogs using uwb radar," Master's thesis, Norwegian University of Science and Technology, 2015.

[2] M. I. Skolnik, Introduction to Radar systems. McGraw Hill Education Private Limited, 3 ed., 2014.

[3] H. Langen, "Ultra-Wideband Radar Simulator for classifying Humans and Animals based on Micro-Doppler Signatures," Master's thesis, Norwegian University of Science and Technology, Norway, 2016.

[4] A. Alzogaiby, "Using micro-doppler radar signals for human gait detection," Master's thesis, Stellenbosch University, 2014.

[5] H. Langen, "Simulation of micro-doppler signatures in ultra-wideband radar," 2015.

[6] V. C. Chen, The micro-Doppler effect in radar. Artech House, 2011.

[7] R. Boulic, N. M. Thalmann, and D. Thalmann, "A global human walking model with real-time kinematic personification," The Visual Computer, vol. 6, pp. 344–358, Nov 1990.

[8] Novelda AS, XeThru File Formats, 9 2017. Rev. B.

[9] Novelda AS, X4 Impulse Radar Transceiver SoC Datasheet, 2017. Rev. D.

[10] P. Jeroen J.A. van Boxtel, "Free motion capture databases." http://www.jeroenvanboxtel.com/MocapDatabases.html. Accessed: 14.05.2018.

[11] C. M. U. G. Lab, "Carnegie mellon university graphics lab motion capture database." http://mocap.cs.cmu.edu. Accessed: 14.05.2018.

[12] P. Toiviainen and B. Burger, "Mocap toolbox." https://www.jyu.fi/hytk/fi/laitokset/mutku/en/research/materials/mocaptoolbox. Accessed: 02.05.2018.

[13] "C3d the biomechanics standard." https://www.c3d.org. Accessed: 03.05.2018.

[14] "Definition of gait." http://www.dictionary.com/browse/gait. Accessed: 05.04.2018.

[15] C. D. Newton and D. M. Nunamaker, Textbook of Small Animal Orthopaedics. J.B. Lippincott Company, 1985.

[16] M. Otero, "Application of a continuous wave radar for human gait recognition," in Signal Processing, Sensor Fusion, and Target Recognition XIV, vol. 5809, pp. 538–549, International Society for Optics and Photonics, 2005.

[17] D. Sutherland, R. Olshen, E. Biden, and M. Wyatt, The Development of Mature Walking. Cambridge University Press, 1988.

[18] "History of the study of locomotion." http://www.clinicalgaitanalysis.com/history/modern.html. Accessed: 01.05.2018.

[19] "Marker placement guide." http://mocap.cs.cmu.edu/markerPlacementGuide.pdf. Accessed: 05.05.2018.

[20] "Free motion capture data." http://www.motioncapturedata.com/2009/05/animal-motion-capture-dog.html. Accessed: 14.05.2018.

[21] M. A. Richards, J. A. Scheer, and W. A. Holm, Principles of Modern Radar Volume I-Basic Principles. Scitech Publishing, 2010.

[22] M. A. Richards, Fundamentals of radar signal processing. Tata McGraw-Hill Education, 2005.

[23] D. Tahmoush and J. Silvious, "Radar micro-doppler for long range front-view gait recognition," in Biometrics: Theory, Applications, and Systems, 2009. BTAS'09. IEEE 3rd International Conference on, pp. 1–6, IEEE, 2009.

Appendix A

Time-Frequency Window Length

Figures A.1, A.2 A.3 A.4 A.5 and A.6 show how different framebuffer lengths M affects the time-frequency resolution of the micro-Doppler matrix $\boldsymbol{\mu}$. This again affects how prominent the f_m, f_2 and f_3 peaks become in the step-Doppler spectrogram D_g.

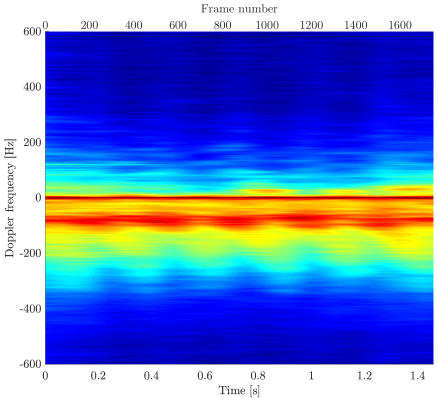

(a) Micro-Doppler signature $\boldsymbol{\mu}$

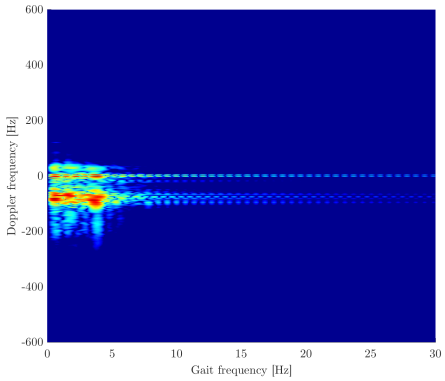

(b) Step-Doppler matrix, $\boldsymbol{D}$

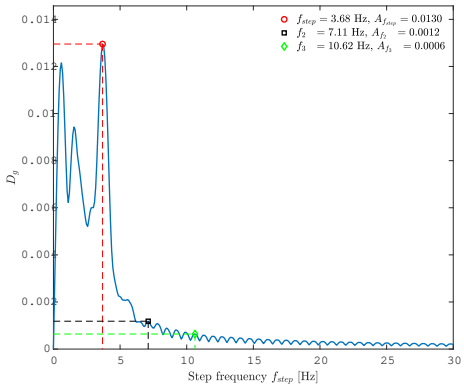

(c) Step-Doppler Spectrum, D_g

Figure A.1: CPI $T_d = 1$s

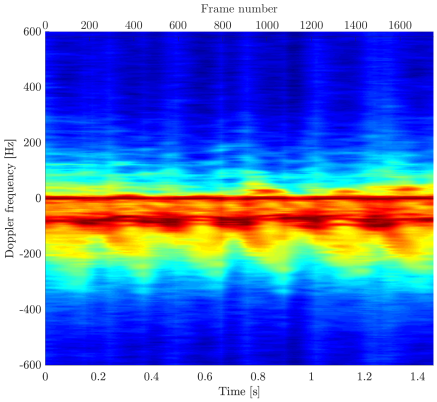

(a) Micro-Doppler signature $\boldsymbol{\mu}$

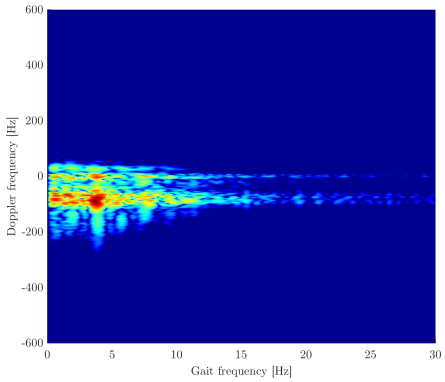

(b) Step-Doppler matrix, $\boldsymbol{D}$

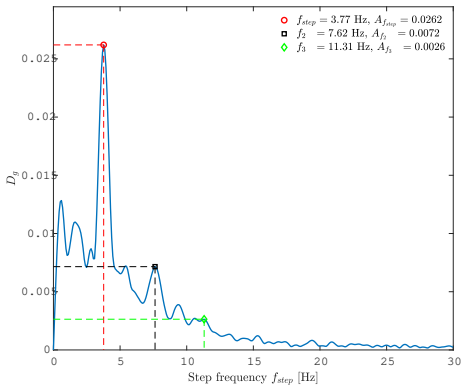

(c) Step-Doppler Spectrum, D_g

Figure A.2: CPI $T_d = 0.5$s

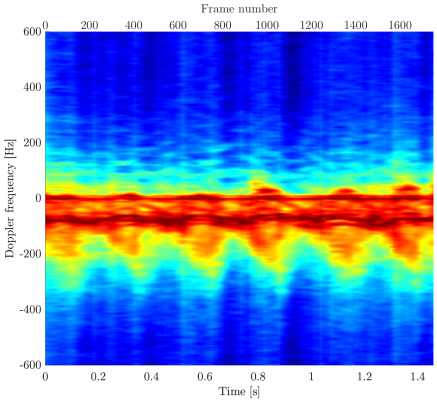

(a) Micro-Doppler signature $\boldsymbol{\mu}$

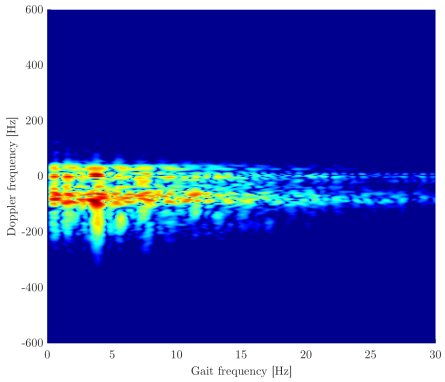

(b) Step-Doppler matrix, $\boldsymbol{D}$

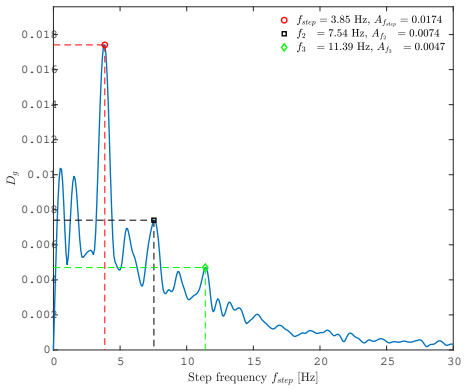

(c) Step-Doppler Spectrum, D_g

Figure A.3: CPI $T_d = 0.3$s

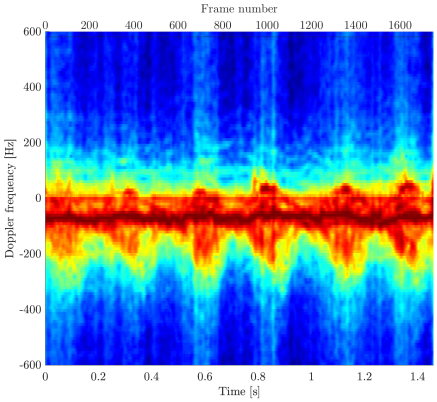

(a) Micro-Doppler signature $\boldsymbol{\mu}$

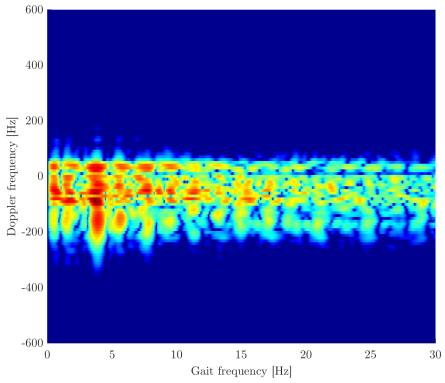

(b) Step-Doppler matrix, $\boldsymbol{D}$

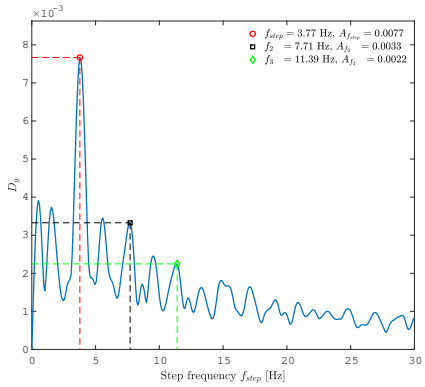

(c) Step-Doppler Spectrum, D_g

Figure A.4: CPI $T_d = 0.1$s

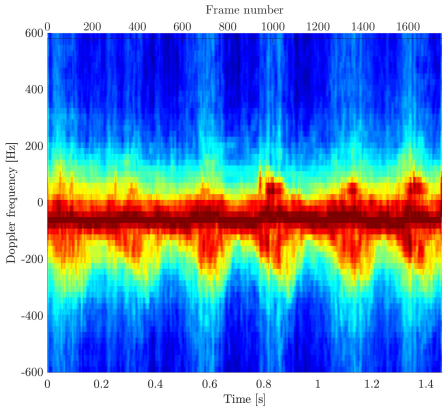

(a) Micro-Doppler signature $\boldsymbol{\mu}$

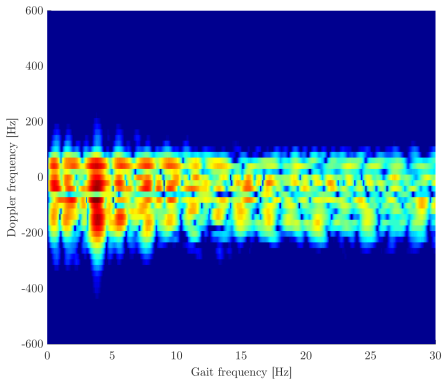

(b) Step-Doppler matrix, $\boldsymbol{D}$

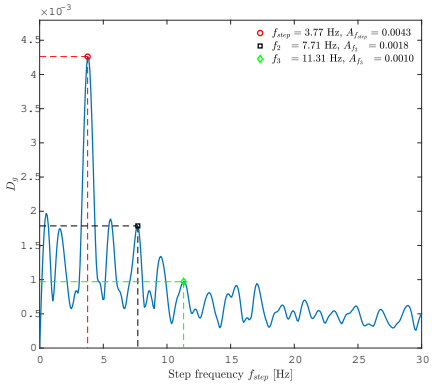

(c) Step-Doppler Spectrum, D_g

Figure A.5: CPI $T_d = 0.05$s

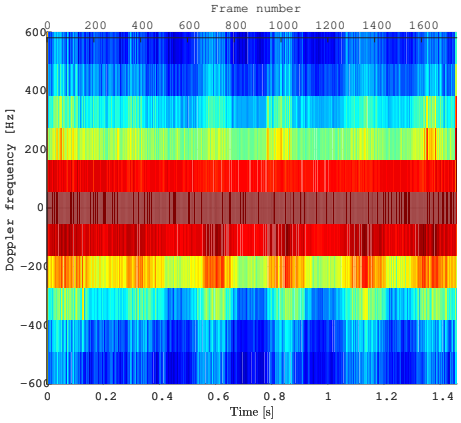

(a) Micro-Doppler signature $\boldsymbol{\mu}$

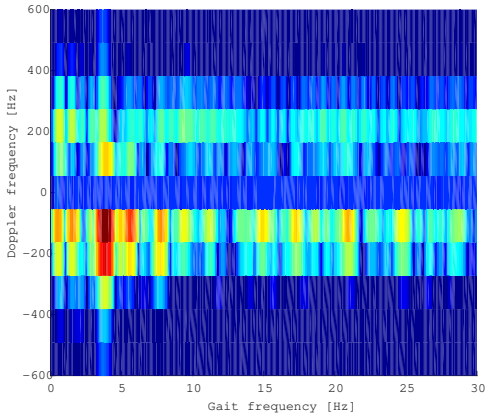

(b) Step-Doppler matrix, $\boldsymbol{D}$

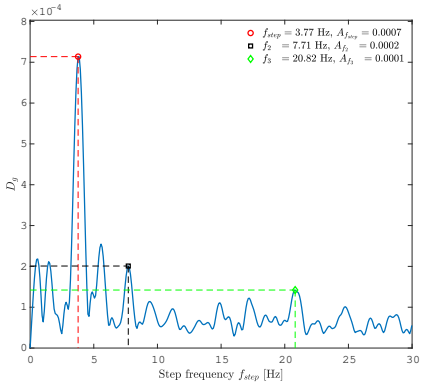

(c) Step-Doppler Spectrum, D_g

Figure A.6: CPI $T_d = 0.01$s